Modelling dynamics of Jakobshavn Isbræ and its contribution to sea level rise over the past and future century

Muresan, Ioana Stefania

Publication date:
2016

Document Version
Publisher's PDF, also known as Version of record

Modelling dynamics of Jakobshavn Isbræ

and its contribution to sea level rise over the past and future century

Ioana Stefania Muresan
Ph.D. thesis
September 16, 2016

Supervisors: Shfaqat A. Khan and Kurt H. Kjær

DTU Space
National Space Institute

Dansk sammenfatning

Den hurtigst flydende gletsjer på jorden, Jakobshavn Isbræ (JI) i Vestgrønland, indeholder nok vand til at øge havniveauet med ~0.7 m, og er derfor blevet studeret nøje igennem det seneste årti. Dynamikken bag JI er grundigt undersøgt, hvorimod gletsjerens længerevarende respons på klimaforandringer stadig er ukendt. Ved at kombinere historiske data med 3-D modellering har vi her fundet ud af, at gletsjerens tunge kollapsede i 1930'erne, efterfulgt af en moderat tilbagetrækning i de følgende årtier og endnu et omfattende kollaps i 2003, efter hvilket gletsjeren har befundet sig i en periode med konstant massetab.

Siden 1840 har JI mistet 1214.5 Gt, svarende til en havniveaustigning på omtrent 3.3 mm eller 12 % af den totale masse af Grønlands ismasse. Klimamodeller forceret med realistiske klimafluktuationer samt gletsjergeometrier forudsiger endnu et markant kollaps resulterende i en tilbagetrækning på op til 40 km langs gletsjerens fæste på den nedadskrånende havbund. Destabiliseringen styres primært af gletsjergeometrien og tyder på at massetabet når at blive tredoblet inden år 2100 i forhold til det forrige århundrede. Klimamodellerne viser endvidere, at for at modvirke den nuværende tilbagetrækningshastighed af gletsjeren, er det nødvendigt at temperaturen i det omkringliggende hav varigt falder med 0.9 °C. Såfremt temperaturen igen stiger vil tilbagetrækningen genoptage. Studiet indikerer desuden et uundgåeligt kollaps af gletsjeren selv for klimascenarier med beskedne temperaturstigninger, hvilket vil resultere i en acceleration af den globale vandstandsstigning.

Modelling dynamics of Jakobshavn Isbræ and its contribution to sea level rise over the past and future century

Ioana Stefania Muresan
National Space Institute
Ph.D. thesis, Kgs. Lyngby, September 16, 2016

www.space.dtu.dk

Abstract

The rate of net ice mass loss from Greenland's marine terminating glaciers has more than doubled over the past two decades highlighting their importance for future sea-level rise. Current projections are built upon observations from a short term record spanning only from several years to a decade. However, the last decade is dominated by anomalous dynamic changes and is therefore not representative of multi-decadal behaviour of glacier dynamics.

A regional three-dimensional outlet glacier model developed as part of the PISM is used to simulate the behaviour of Jakobshavn Isbræ (JI; located in west Greenland) since the end of the Little Ice Age (LIA). The model is forced with different climate variables: near-surface air temperature, surface mass balance (SMB), sea-surface temperature and salinity. In order to accurately simulate and understand the longer-term controls of dynamic changes, the model is constrained by observed terminus positions (1900-2014) and mass change estimates (1997-2014). The present study is the first that successfully simulated JI's behaviour over the last century. For the period 1990-2014, the model simulated two major accelerations in 1998 and 2003 that are consistent with observations of changes in glacier terminus. An initial, and most probably the first significant acceleration of JI after the end of LIA was modelled in ~1930. Overall, I found that the ocean influence in JI's behaviour over the last century is significant and most of the JI retreat during 1840–2014 is driven by the ocean parametrization and the glacier's subsequent response, which was largely governed by its own bed geometry. In my simulations, the retreat of the front reduced the buttressing at the terminus and generated a dynamic response in the upstream region of JI which finally led to flow acceleration. This buttressing effect tends to govern JI's behaviour. Consequently, the results showed that the dynamic changes modelled at JI are triggered at the terminus.

In a final phase, using this model that has been adjusted to the longer-term record, I performed experiments to the near future (i.e., 2013-2100) using five ocean temperature scenarios and two atmospheric scenarios (RCP 4.5 and RCP 8.5) as climate forcing. In terms of mass change, I found that from the end of the LIA until the end of the 21st century JI's mass change was and will remain predominately dynamically controlled (between 74 % and 86 % of the mass change is dynamic in origin). The study further indicates that the change in mass loss at JI is already triggered and that an eminent collapse of the terminus by the end of the century with retreat of up to 40 km along JI's downward-sloping, marine-based bed is inevitable. A cooling experiment suggested that 0.9 °C of ocean cooling is needed to reverse the current retreat trend which however, will restart once cooling stops. The modelled

cumulative mass change for the period 1840-2012 is ~1215 Gt or 3.4 mm SLR equivalent. For the 21st century, the best case scenario with regards to future warming (i.e., no increase in surface ocean temperature relative to present day) suggested mass loss estimates amount to ~1860 Gt by the year 2100 (67 % increase relative to 1840-2012) or 5.2 mm SLR equivalent. In the worst case scenario with regards to future warming expected mass loss of JI amounts to 3275 Gt by the year 2100 (192 % increase relative to 1840-2012) or 9.1 mm SLR equivalent.

Overall, the study is unique both in approach and results obtained, and shows significant progress in modelling the temporal variability of the flow at JI. The study improves our quantitative understanding of the past and future of JI's dynamics.

Acknowledgements

The work has been carried out at the Technical University of Denmark (DTU), DTU SPACE, between May 2013 and April 2016 under the supervision of Shfaqat A. Khan and Kurt H. Kjær. The Ph.D. was co-funded by Forskningsraadet for Natur og Univers (grant no. 12-155118) and DTU SPACE. Additional funds for conference participations were provided by Otto Mønsteds fond.

I am indebted to many people for making my Ph.D. an unforgettable experience. First, I would like to thank my advisors Abbas and Kurt, for giving me the chance to be part of the next generation of ice sheet modellers, and especially Abbas, for his continuous support and mentoring during the last three years. Thank you for encouraging my research and for allowing me to grow as a scientist. I am also very grateful for the opportunity to do field work in Greenland. As a modeller this gave me a unique perspective on just how big and fragile these frozen rivers of ice really are.

I should also thank the PISM group (Ed, Constantine and Andy) for their help and assistance with PISM at the beginning of my journey. Their host and support during my external stay at University of Alaska Fairbanks (UAF) was invaluable.

I thank my fellow colleagues, especially Tibor, Johan, Heidi, Maulik, Peter and Zhao for stimulating discussions and for creating a motivating work environment.

Many thanks to Andrei, Morgan and Flavia for proofreading corrections.

Least but not last, I would like to thank my family: my parents and my brother for their endless care and support, and for constantly pushing me to follow my dreams.

Abbreviations

BOX – a climate reconstruction after Box et al. (2013)

DJF – December, January, and February

DMI – Danish Meteorological Institute

FTT – Force To Thickness mechanism

GIA – Glacial Isostatic Adjustment

GPS – Global Positioning System

GrIS – Greenland Ice Sheet

HIRHAM – The Hydrostatic Atmospheric Regional Climate Model

JI – Jakobshavn Isbræ

JJA – June, July, and August

LIA – Little Ice Age

MET – Met Office Hadley centre

PDD – Positive Degree Day method

PISM – the Parallel Ice Sheet Model

RACMO – The Regional Atmospheric Climate Model

RCP - Representative Concentration Pathway

RMSE – Root Mean Squared Error

SLE – Sea Level Equivalent

SLR – Sea Level Rise

SIA – Shallow Ice Approximation

SMB – Surface Mass Balance

SSA – Shallow Shelf Approximation

SST – Sea Surface Temperature

T – Surface Air Temperature

Table of contents

CHAPTER 1

Introduction

The recent rapid dynamic mass loss of tidewater outlet glaciers in Greenland through acceleration of ice discharge highlights their importance for sea-level rise, but the controlling processes are not well understood and have been identified in the 5th IPCC-report as a major uncertainty in our ability to predict future sea-level. Recent studies (Rignot et al., 2008; Moon et al., 2012; Shepherd et al., 2012; Enderlin et al., 2014) suggest that the rate of net ice mass loss from Greenland's marine terminating glaciers has more than doubled over the past two decades. Jakobshavn Isbræ (JI), located mid-way up on the west side of Greenland (Fig. 1), is one of the largest outlet glaciers in terms of drainage area as it drains ~6 % of the Greenland Ice Sheet (GrIS) (Krabill et al., 2000). JI terminus retreated ~30 km from 1850 to 1964, followed by a stationary front for 35 years (Csatho et al., 2008). Following initial glacier acceleration in 1998, JI retreated over 15 km between 2001 and 2007. Due to its consistently high ice flow rate and seasonally varying flow speed and front position, the glacier has received much attention over the last two decades (Thomas et al., 2003; Luckman and Murray, 2005; Holland et al., 2008; Amundson et al., 2010; de Juan et al., 2010; Khan et al., 2010; Motyka et al., 2011; Joughin et al., 2012; Gladish et al., 2015a; Gladish et al., 2015b). Measurements from synthetic aperture radar suggest that the ice flow speed of JI doubled between 1992 and 2003 (Joughin et al., 2004). More recent measurements show a steady increase in the flow rate over the glacier's faster-moving region of ~5 % per year (Joughin et al., 2008). The speedup coincides with thinning of up to 15 m a^{-1} between

2003 and 2012 near the glacier front (Krabill et al., 2004; Nielsen et al., 2013) as observed from airborne laser altimeter surveys. The steady increase in the flow rate and the glacier thinning suggest a continuous dynamic drawdown of mass, and they highlight JI's importance for the GrIS mass balance and future sea-level rise.

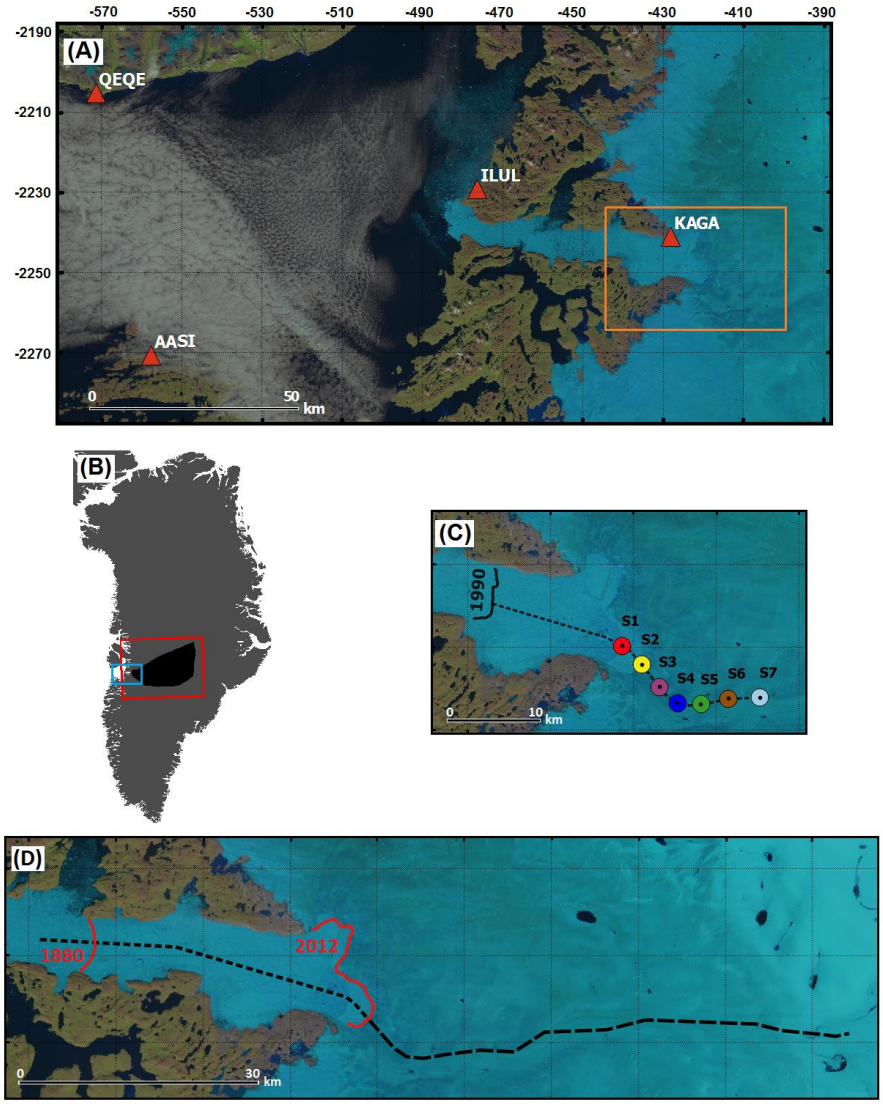

Figure 1: (A) Landsat 8 image of Ilulissat fjord and part of Disko Bay acquired in August 2014. The dark orange triangles indicate the locations of the GPS stations shown in Fig. 32. The rectangle defined by light orange borders outlines the location of Fig. 1C. (B) Grey filled Greenland map. The black filled rectangle highlights the JI basin used to compute the mass loss and is identical to Khan et al. (2014). The rectangle defined by red borders indicates the computational domain. The light blue border rectangle represents the location of Fig. 1A. (C) Coloured circles indicate the

locations plotted in Fig. 28. The thick black line denotes the JI terminus position in the 1990s. The dotted black line represents the flow-line location plotted used in Sect. 6. (D) The dotted black line represents the flow-line location used in Sect. 5. The long dashed black line represents the flow-line location used in Sect. 7. The solid dark red lines denote the JI terminus positions in 1880 and 2012. The coordinates given in (A) are in polar-stereographic projection units (km).

This thesis focuses on numerically modelling Jakobshavn Isbræ constrained to a variety of observations. Numerical ice sheet models provide quantitative insights on the four-dimensional distribution of stresses and allow us to reconstruct past and future ice mass changes and glacier dynamics which cannot be inferred from, e.g. satellite and airborne data or geological evidence. Several processes have been identified as controlling the observed speedup of JI (Nick et al., 2009; Van der Veen et al., 2011; Joughin et al., 2012). One process is enhanced sliding at the glacier bed due to increased lubrication from surface melt water reaching the bed, as indicated by correlations between enhanced flow and increased surface melt. A second process is a reduction in resistance (buttressing) at the marine front through thinning and/or retreat of the glacier termini. Recent findings indicate that the first explanation is relevant on relatively short time-scales (days to weeks). The second process, reduced buttressing at the marine terminus, seems to more likely explain the recent dynamic changes observed in Greenland (Nick et al., 2013) but the details of the processes triggering and controlling thinning and retreat remain elusive. Accurately modelling complex interactions between thinning, retreat, and acceleration of flow speed as observed at JI, still remains challenging.

Furthermore - and crucially - our current understanding of these processes is almost entirely based on observations from a short-term record, spanning only from a year to a decade (i.e., mostly starting 2000; Vieli et al., 2000; Nick et al., 2009; Vieli et al., 2011), and which are characterized by short-term fluctuations and therefore not representative for longer-term trends of decade-to-century time scales. The initial speedup of JI occurred at a time when the satellite and airborne observations were unavailable (i.e., sometime at the end of the Little Ice Age, LIA) and it is these longer-term trends that are relevant for a robust assessment of present and future sea-level. The unique years to multi-decadal timescale dataset of outlet glacier changes acquired with an existing specifically designed fully 3-D dynamic numerical model for outlet glacier flow allows us to investigate and quantify in detail the longer-term controls of such dynamic changes. Understanding the sensitivity of dynamic thinning to climate forcing beyond the last decade is crucial for accurately projecting the GrIS contributions to global sea level change.

Here, I used a high-resolution, three-dimensional, time-dependent regional outlet glacier model that has been developed as part of the Parallel Ice Sheet Model (PISM; see Sect. 3) (The PISM Authors, 2014) to investigate the dynamic evolution of JI between 1840-2014. The model is forced with different climate variables: near-surface air temperature, surface mass balance (SMB), sea-surface temperature and salinity. My modelling approach is based on regional equilibrium simulations and a time-integration over the period 1840 to 2014. Overall, I perform over 200 experiments which I divide in Study 1, Study 2, and Study 3. These experiments range between simulations with fixed terminus positions (i.e., Study 1) to simulations that allow the grounding lines and the calving fronts to evolve freely under the applied ocean parametrization and monthly atmospheric forcing (i.e., Study 2 and 3).

In general, reproducing past and present-day observations of the dynamical behaviour of Greenland's outlet glaciers is the key for developing realistic projections of future changes in the GrIS (IPCC, 2013). In a final phase, using this model that has been adjusted to the longer-term record, I will run experiments to the near future (i.e., 2013-2100) using five different ocean temperature scenarios and two different RCP (Representative Concentration Pathways) scenarios (RCP 4.5 and RCP 8.5) as climate forcing (i.e., Study 4).

1.1 Existing literature

Over the past decade, we have seen significant improvements in the numerical modelling of glaciers and ice sheets (e.g. Price et al., 2011; Vieli and Nick, 2011; Winkelmann et al., 2011; Larour et al., 2012; Pattyn et al., 2012; Seroussi et al., 2012; Aschwanden et al., 2013; Nick et al., 2013; Mengel and Levermann, 2014; Aschwanden et al., 2016) and several processes have been identified as controlling the observed speedup of JI (Nick et al., 2009; Van der Veen et al., 2011; Joughin et al., 2012). Some regional scale glacier models are based on a flow-line approach (Nick et al., 2009; Parizek and Walker, 2010), which models the one- or two-dimensional dynamic behaviour of the glacier under consideration. Flow-line models are computationally efficient and valuable for understanding basic processes. However, three-dimensional models are more appropriate in areas of flow divergence/convergence and/or where lateral stresses are important. All the existing literature on modelling and projecting JI dynamics and mass changes using forward simulations is mostly based on flow-line models (Vieli et al., 2000; Nick et al., 2009, Vieli et al., 2011, Nick et al., 2013), where the model is calibrated only on the last decade. The last decade, however, is not necessarily representative for typical glacier behaviour and as discussed by Bevan et al. (2012), this period is most probably dominated by anomalous dynamic signal. On the other hand, previous 3-D modelling studies have mostly concentrated on modelling individual processes using stress

perturbations (e.g. Van der Veen et al., 2011, Joughin et al. 2012). The present study is the first that aims to model the behaviour of JI since the end of the Little Ice Age (LIA) with a 3-D process-based model.

The 3-D regional glacier model used here has been developed by Della-Giustina (2011) and it is now fully available in PISM. The regional model is capable of simulating an outlet glacier, and its associated drainage basin using an approach that is very similar to a one-way nested model. In such a model the coarse domain provides the initial and the boundary conditions for the nest domain (i.e., the high resolution regional domain) and feedbacks between the coarse domain and the nest are not included. PISM does not perform the actual grid nesting but allows the user to specify the initial and the boundary conditions provided by the whole ice sheet initialization simulation in an approach similar with the one-way nested model (Della-Giustina, 2011). PISM and its underlying equations and theory are further detailed in Sect. 3.

An initial parameter study for JI was performed by Della-Giustina (2011) using the regional model on 2 km and 1 km grids. The goal of that particular study was not to reproduce observations but rather to find sets of parameters that produce certain behaviours within the model, to define grid size sensitivity and to evaluate the temporal resolution for which model results are still relevant after initialization. Her experiments suggest that for JI, the modelled results are relevant for ~1000 model years after initialization and increasing the resolution from 2 km to 1 km does not result in model improvement with respect to ice thickness or horizontal surface velocities.

1.2 Overview

Overall, this study aims to improve our quantitative understanding of the past, present and future JI dynamics and mass change estimates, as well as to constrain JI's contribution to sea-level rise over 260 years. The study shows significant progress in modelling the decadal and temporal variability of the flow at JI.

The thesis is organized as follows. Chapter 2 provides an overview of the overall data used in the thesis. I describe both data used as an input in PISM, such as atmospheric and oceanic forcing or observed terminus positions, but also data used in the validation of the model, such as ice thickness changes or horizontal velocities.

In Chapter 3, I describe PISM, its underlying physics and equations. The initialization procedure and the regional modelling approach are also detailed in this chapter.

In Chapter 4 (Study 1), I focus on finding a suitable initialization method for my further studies, as well as to define atmospheric forcing and bed topography sensitivities, and evaluate if the regional model is able to realistically transform climate forcing into simulate mass change.

Chapter 5 (Study 2) describes regional JI simulations performed from the end of the LIA until 2012. Here, I focus on modelling the terminus advance and/or retreat and the speed fluctuations observed at JI during the period 1840-2012. Relative to Chapter 6, I am mostly interested in the overall modelled 20th century retreat and mass change.

Chapter 6 (Study 3) focuses mainly on simulations performed from 1990 until 2014. Relative to Chapter 5, here I focus more on the seasonal driven terminus advance and/or retreat and speed fluctuations of JI during the period 1990-2014. The period 1990-2014 is abundant in observations and ensures better constrains for the model. In the same chapter, I present the regional model sensitivity to parameters controlling ice dynamics, basal processes, ice shelf melt, and ocean temperature.

Chapter 7 (Study 4) presents projections (prognostic modelling) for the period 2013-2100 using two RCP scenarios (i.e., RCP 4.5 and RCP 8.5) as atmospheric forcing and five ocean temperature scenarios as oceanic forcing. Each study (Chapter 4 to Chapter 7) ends with its own Discussion section.

Chapter 8 highlights the main findings of the thesis and brings together the discussion performed at the end of each study.

Chapter 9 provides the overall conclusion and outlook of the thesis.

The Appendix sections A to F include additional figures and tables. Appendix G introduces teaching activities and conferences attended during the Ph.D. period.

Additional to the main text presented here, the Ph.D. dissertation consists of the following papers:

i. Khan, S. A., K. H. Kjær, M. Bevis, J. L. Bamber, J. Wahr, K. K. Kjeldsen, A. A. Bjørk, N. J. Korsgaard, L. A. Stearns, M. R. van den Broeke, L. Liu, N. K. Larsen, and **I. S. Muresan**. 2014. "Sustained mass loss of the Northeast Greenland Ice Sheet triggered by regional warming." Nat. Clim. Change 4: 292–299. doi:10.1038/nclimate2161.

ii. **Muresan, I. S.**, S.A. Khan, A. Aschwanden, C. Khroulev, T. Van Dam, J. Bamber, M. V. D. Broeke, B. Wouters, P. Kuipers Munneke, and K. H. Kjær. 2016. "Modelled glacier dynamics over the last quarter of a

century at Jakobshavn Isbræ". The Cryosphere 10(2): 597-611. doi: 10.5194/tc-10-597-2016.

iii. **Muresan, I. S**., S. A. Khan, A. A. Bjørk, K. K. Kjeldsen, K. H. Kjær, A. Aschwanden, P. Langen, T van Dam, C Gladish, D Holland , J. E. Box and Michiel van den Broeke. 2016. "Eminent and inevitable terminus collapse of Jakobshavn Isbræ by 2100". Manuscript in review in Nature Geoscience (available upon request).

CHAPTER 2

Data

2.1 Atmospheric input

2.1.1 Surface mass balance and air temperature for the period 1840-2014

As most of the ice sheet models are run offline, the required atmospheric forcing includes only the surface mass balance (SMB; the net balance between accumulation (snowfall) and ablation (melt and subsequent runoff)), and surface air temperature or precipitation and surface air temperature, if a PDD scheme is employed. The first option, also my choice for the outlet regional glacier model, is often the preferred one, especially if the climate model in use has high quality surface mass and energy sub-models. Therefore, HIRHAM5 and RACMO2 and a climate reconstruction after Box et al. (2013), Box (2013), Box and Colgan (2013), hereafter "BOX" are used in this thesis.

The regional climate model RACMO2 (Ettema et al., 2009) is a high-resolution limited area model with physical processes adopted from the global model of the European Centre for Medium-Range Weather Forecasts (ECMWF). Its adaptation for the GrIS, including the treatment of meltwater percolation and refreezing, as well as the evaluation of the modelled SMB, is described by Ettema et al. (2009) and

Ettema et al. (2010). The lateral boundary conditions are provided by ECMWF reanalyses, notably ERA-40 and ERA-Interim, and the model is run at a spatial resolution of ~11 km over the period 1958 to 2014. Based on a comparison with observations, Ettema et al. (2009) concluded that the model performs very well in simulating accumulation (N = 265, r = 0.95), yielding a 14 % uncertainty in ice-sheet integrated SMB. The model provides monthly means of near-surface air temperature, climatic mass balance, and the individual subcomponents, i.e., precipitation, evaporation/sublimation, run-off, melting, and re-freezing (Fig. 2).

The hydrostatic atmospheric regional climate model HIRHAM is based on HIRLAM7 dynamics (Eerola, 2006) and ECHAM5 physics (Roeckner et al., 2003). HIRHAM5 is run at a spatial resolution of ~5.55 km and provides monthly mean 2 m air temperature and climatic mass balance for the period 1989-2012 (Fig. 2; Christensen et al., 2006). HIRHAM5 is forced at the lateral boundaries based on the ERA-Interim product (Dee et al., 2011). Error estimates for HIRHAM are based on comparison with ice cores for the 1989-2010 period to assess annual accumulation accuracy and with PROMICE automated weather station ablation rate observations (Ahlstrøm et al., 2008; Fausto et al., 2012) for June, July, and August (JJA) in the 2007-2013 period. The HIRHAM data have a ~-3.5 % accumulation rate bias and a 38 % RMS error. HIRHAM SMB data have an average 0.714 correlation with monthly PROMICE data, a bias of +0.07 m water equivalence (w.e.), and an absolute RMS error of 42 % (Jason Box, personal communication).

The BOX climate reconstruction (Box et al., 2013; Box, 2013; Box and Colgan, 2013) is based on monthly meteorological stations air temperatures, ice cores, and regional climate model outputs combined to develop a continuous 172 yr (1840-2012) monthly reconstruction of ice sheet SMB, accumulation rate, and near surface air temperatures (Fig. 2). The BOX reconstruction is produced at a resolution of ~5 km, providing near surface air temperature, climatic mass balance and its individual subcomponents, i.e. run-off and internal accumulation. In the version used here, several refinements are made to the Box (2013) temperature (T) and SMB reconstruction. Multiple station records now contribute to the near surface air temperature for each given year, month and grid cell in the domain, while in Box (2013), data from the single highest correlating station yielded the reconstructed value. The estimation of values is made for a domain that includes land, sea, and ice. Box (2013) reconstructed T over only ice. A physically-based meltwater retention scheme of Pfeffer et al. (1990, 1991) replaces the simpler approach used by Box (2013). The RACMO2 data have a higher native resolution of 11 km as compared to the 24 km Polar MM5 data used by Box (2013) for air temperatures. The revised surface mass balance data end two years later in year 2012. The annual accumulation rates from ice cores are dispersed into a monthly temporal resolution by weighting

the monthly fraction of the annual total for each grid cell in the domain evaluated using 1960-2012 RACMO2 data. In an identical error assessment as with HIRHAM, for BOX, the accumulation rate has a -6.3 % bias and a 32 % RMS error. For SMB, using 20 station years of PROMICE data, the BOX JJA SMB has a correlation with independent observations of 0.650, an average bias of +0.10 m water equivalence, and an absolute RMS error of 40 % (Jason Box, personal communication).

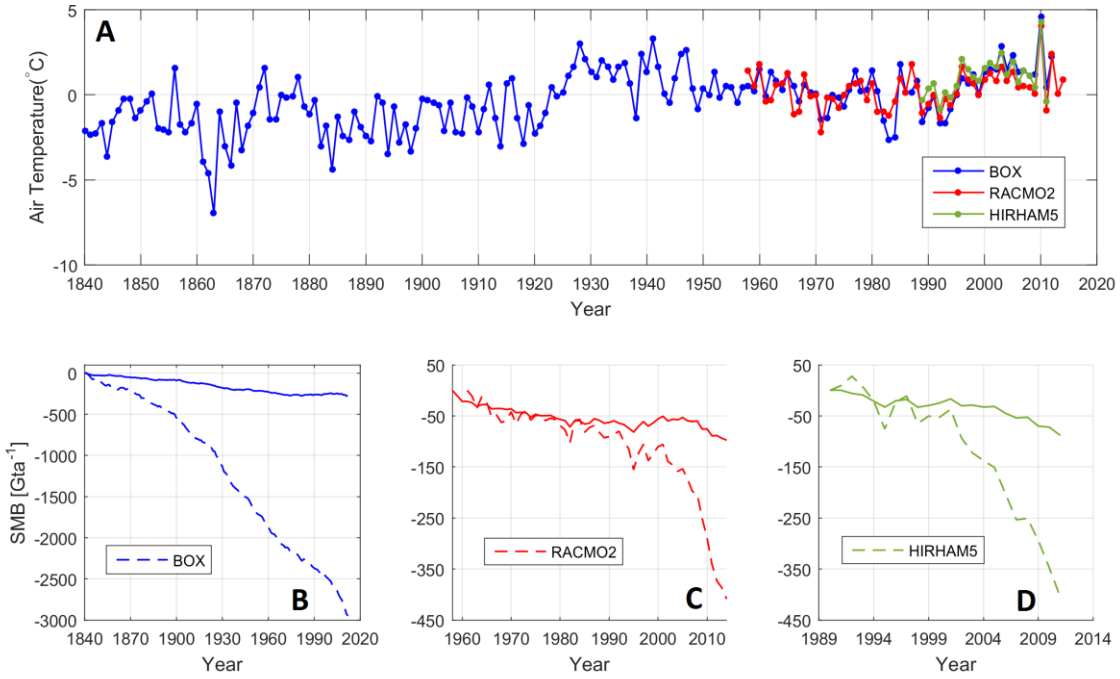

Figure 2: (A) Surface air temperatures anomalies relative to the period 1960-1990 for BOX (1840-2012; blue) and RACMO2 (1958-2014; red), and relative to the period 1989-1990 for HIRHAM5 (1990-2011; green). The mass change due to SMB for BOX (B), RACMO2 (C) and HIRHAM5 (D), computed for the whole computational domain is shown with dashed line and in the mask from Fig. 1B with solid line. For BOX and RACMO2, I removed the 1960-1990 baseline.

Mean summer (June, July, August (JJA)) and mean winter (December, January, February (DJF)) 1990-2012 temperature and SMB for the three datasets used as atmospheric forcings are introduced for JI in Fig. 3.

2.1.2 Surface mass balance and air temperature for the period 2010-2100

The Representative Concentration Pathways (RCP) scenarios are four greenhouse gas concentration trajectories developed for IPCC (2013). The RCP 4.5 was developed by the MiniCAM modeling team at the Pacific Northwest National Laboratory's Joint Global Change Research Institute (JGCRI) and assumes

employment of a range of technologies and strategies for reducing greenhouse gas emissions. Generally, RCP 4.5 is known as a stabilization scenario, where the total radiative force is stabilized before 2100. The resulting development path is detailed

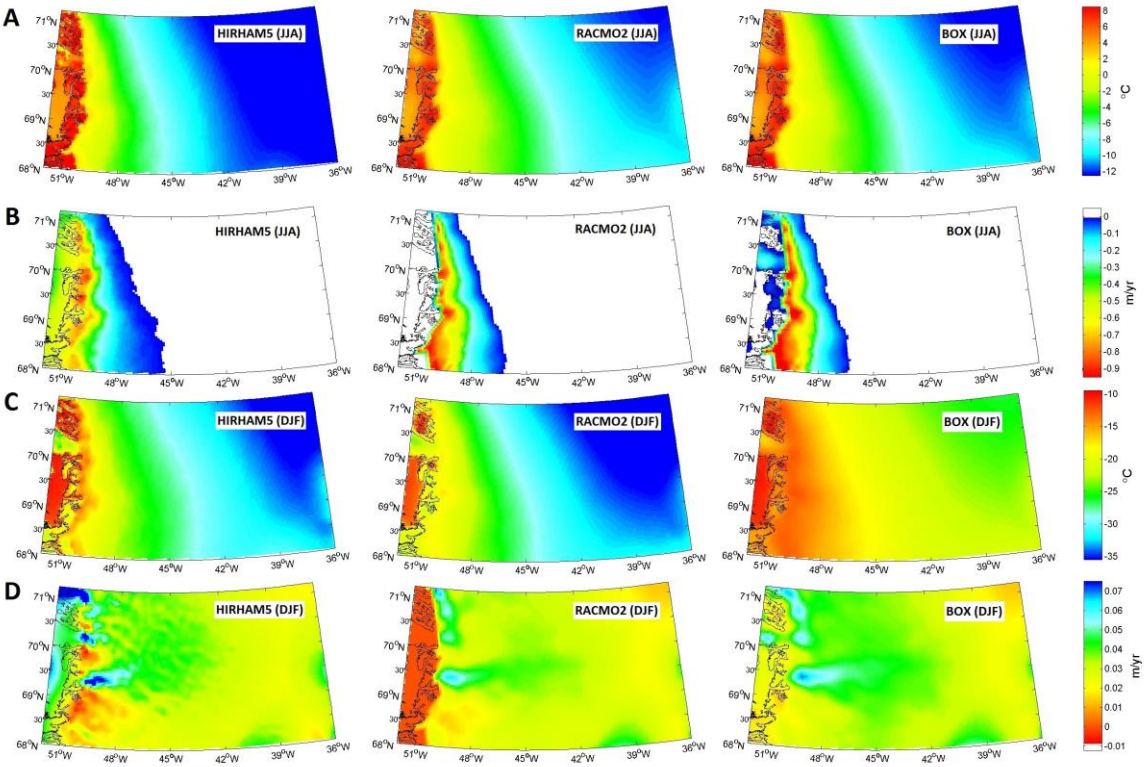

Figure 3: Mean summer (June-August) 1990-2012 air temperature (A) and SMB (B) and mean winter (December-February) air temperature (C) and SMB (D) for HIRHAM5, RACMO2 and BOX for my regional Jakobshavn Isbræ domain (Fig. 1B). The JJA temperature is similarly represented by all three datasets with more accentuated differences in the interior part of the domain, while the JJA SMB is characterized by large fluctuations in the proximity of the coastline. The DJF mean temperature and SMB are characterized by large fluctuations among the three datasets, both near the coast and in the interior parts of the domain (note BOX DJF temperature). All three datasets are presented on a 5 km grid.

in Clarke et al. (2007). The RCP 8.5 was developed by the MESSAGE modeling team and the Integrated Assessment Framework at the International Institute for Applies Systems Analysis (IIASA), Austria. Generally, the RCP 8.5 is characterized by increasing greenhouse gas emissions and by the end of 2100 results in high greenhouse gas concentration levels. The resulting development path is detailed in Riahi et al. (2007).

The RCP 4.5 and RCP 8.5 derived SMB and surface air temperature scenarios for my regional JI domain were computed by Peter Langen at the Danish Meteorological Institute (DMI). The 5 km HIRHAM5 regional model (Lucas-Picher et al., 2012) was driven with updates to the snow-ice-subsurface scheme (Langen et al., 2015) into the future using output from the EC-Earth atmosphere-ocean general circulation model. Six-hourly fields of SST and sea ice concentration as well as temperature, humidity and winds on the lateral boundaries of the HIRHAM5 domain were used.

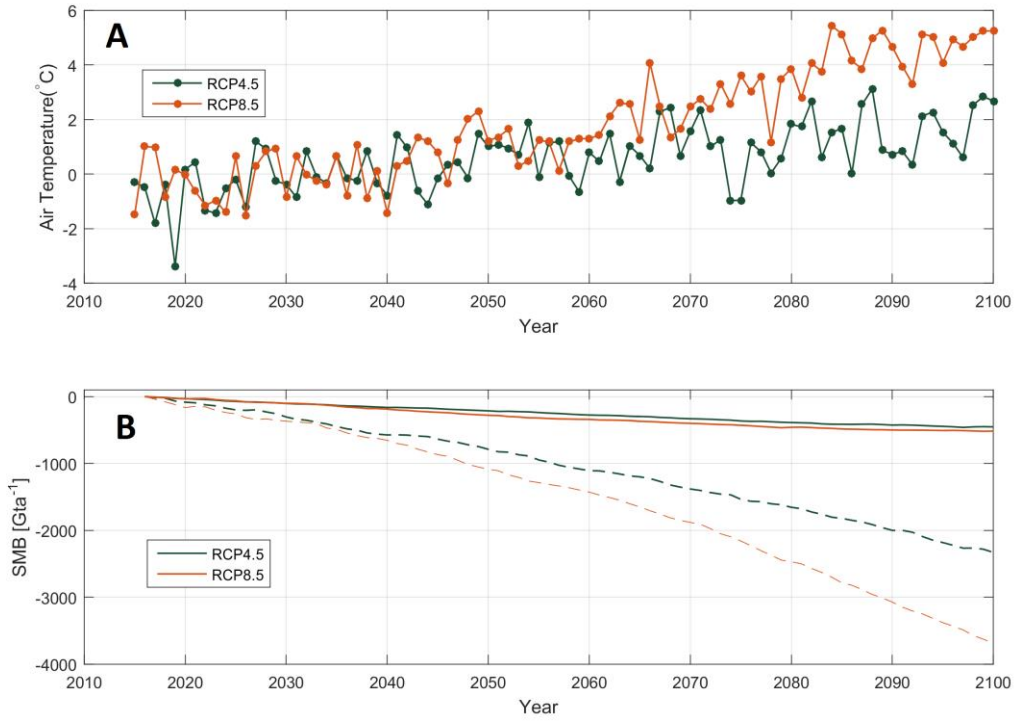

Figure 4: (A) Surface air temperatures anomalies (i.e., relative to 2000-2010) for the period 2016-2100 for RCP 4.5 (green) and RCP 8.5 (red). (B) The mass change due to SMB (i.e., after the 2000-2010 baseline is removed) for RCP 4.5 and RCP 8.5 for the whole computational domain (dashed line) and in the mask shown in Fig. 1B (solid line).

The daily SMB calculations from the HIRHAM5 were performed after an update to the subsurface model employed by Langen et al. (2015). The EC-Earth simulation supplied a reference period historical simulation up to 2010, and continued into the future along the RCP 4.5 and RCP 8.5 scenarios for atmospheric composition. As it was too computationally demanding to run the HIRHAM5 for the full century-long duration using two different scenarios, two 20-year time slices with a total of 5×20 HIRHAM5 simulations for each scenario were selected (Peter Langen, personal communication). Having T and SMB from these 100 years of simulation, an interpolation to produce continuous driving fields for the PISM experiments to 2100

with both the RCP 4.5 and RCP 8.5 scenarios was performed. The difference in SMB between RCP 4.5 and RCP 8.5 for the whole computational domain is ~1355 Gt (Fig. 1B), while relative to the JI drainage basin mask (Fig. 1B), the difference decreases to only ~62 Gt.

The RCP 4.5 and RCP 8.5 derived air temperature and SMB for the period 2010-2100 are further used in Study 4.

2.2 Ocean input

2.2.1 Ocean water salinity and temperature for the period 1840-2014

From the ocean side, I used a parametrization for ice shelf melting where the melting effect of the ocean is based on both ocean temperature and salinity (Martin et al., 2011). This ice shelf melting parametrization is described in detail in Sect. 3.6.

A previous study conducted by Mengel and Levermann (2014) using the same ice shelf melting parametrization established that the sensitivity of the melt rate to salinity is negligible. Therefore, I chose to keep the ocean water salinity (35 psu) constant in time and space as the model does not capture the salinity gradient from the base of the ice shelf through layers of low and high salinity. Regarding the ocean temperature, whenever the parametrization for ice shelf melting was used, I always started the simulations with a constant ocean water temperature of -1.7 °C, which I considered to be the surface ocean temperature in the grid cells adjacent to the JI terminus (i.e., Study 2 and 3). I have also computed (i.e., relative to this starting temperature) 10 year intervals of sea surface temperature anomaly changes (SST; 10×17), which I then used as an input to the meting parametrization (Sect. 3.6) in Study 2. To obtain these anomalies, I removed the 1961–1990 mean annual SST (Fig. 5). The SST data have been extracted from the HadISST1 Met Office Hadley Centre dataset (MET[1]).

2.2.2 Ocean water salinity and temperature for the period 2013-2100

For ocean projections (Study 4), I used a similar approach with the one presented in Sect. 2.2.1, where I kept the ocean water salinity constant (35 psu) and I computed 10 year intervals (10×9) based on a linear increase in ocean surface temperature which I divided in intermediate (Scenario B, 1 °C) and harsh (Scenario C, 3°C). The magnitude of the ocean temperature increase is in agreement with projected ocean warming around Greenland (e.g. Yin et al. 2011; IPCC, 2013). Additionally, I considered a scenario with 0 °C increase in ocean temperatures relative to the reference period 2000-2012 (i.e., -1.3 °C, see Fig. 5) which I denoted as Scenario A.

[1] http://www.metoffice.gov.uk/hadobs/hadisst/data/download.html

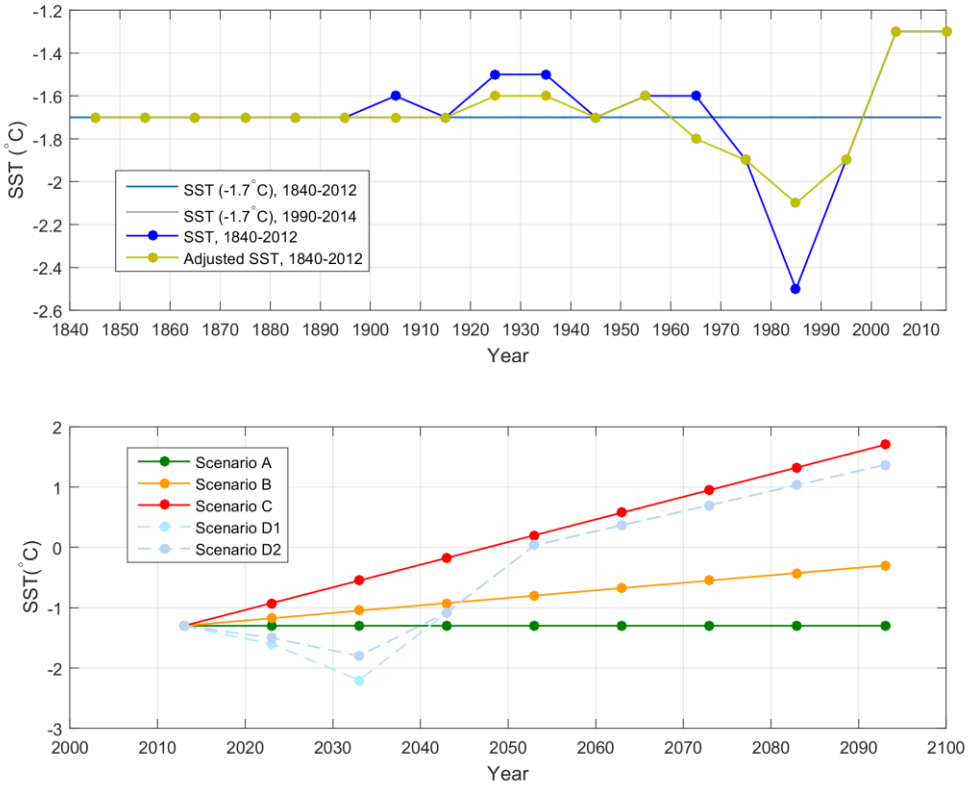

Figure 5: Surface ocean temperature used as an input in the historical simulations (top) and in the prognostic simulations (bottom). The light blue line and the olive-yellow line (top) are superimposed over the period 1845-1915. "SST, 1840-2012" refers to temperature changes as extracted from the original MET data set. "Adjusted SST, 1840-2012" represent temperatures that have been adjusted such that the model accurately matched the observed trend in mass change for the period 1997-2012.

The period 1970-1992 is known as a cooling period, where low temperatures are characteristic for the GrIS. This cooling period is mostly attributed to an increase in atmospheric aerosols (Schlesinger 1994, Chylek et al. 2004). According to Liepert et al. (2002) a global reduction of ~4 % in incoming solar radiation reaching the ground between 1961 and 1990 was observed. The cooling episodes in 1983-1984 and 1991-1992 are related with major volcanic eruptions (i.e., Mt. Pinatubo eruption in June 1991 followed by two years of cooling, 1991-1992). Some researchers have also attributed the cooling/warming phase to changes in the North Atlantic Oscillation (NAO) (IPCC, 2013). To include such a cooling period in my simulations, I further designed two additional scenarios (Scenario D1 and Scenario D2; Fig. 5). Both scenarios assume an ocean cooling period between 2020-2040. While Scenario D1 assumes a decrease in surface ocean temperatures similar in magnitude with the "MET SST changes" for the period 1970-1990 (~0.9°C; Fig. 5), Scenario D2

assumes a decrease similar with the "Adjusted SST" (~0.5°C; Fig. 5 and Sect. 5). Over the period 2041-2060, both scenarios assume a linear increase in SST of 1.1 °C. Starting 2060, both scenarios include the SST changes used in Scenario C (~0.37 °C; Fig. 5). Regarding the atmospheric forcing, during the cooling period, I used mean 1960-1990 air temperature and SMB.

2.3 Bedrock topography and surface elevation

I used the bed topography from Bamber et al. (2001) and Bamber et al. (2013). The 1 km bed elevation dataset for all of Greenland (Bamber et al., 2013) was derived from a combination of multiple airborne ice thickness surveys and satellite-derived elevations during 1970–2012. In comparison with the compilation published in 2001, the 2013 dataset has an improved resolution, particularly along the ice sheet margin. In the region close to the outlet of JI, data from an 125 m CReSIS DEM (that includes all the data collected in the region by CReSIS between 1997 and 2007) have been used to improve the accuracy of the dataset. Errors in bed elevation are known to range from 10 m to 300 m, depending on the distance from an observation and the variability of the local topography (Bamber et al., 2013). At the continental margin,

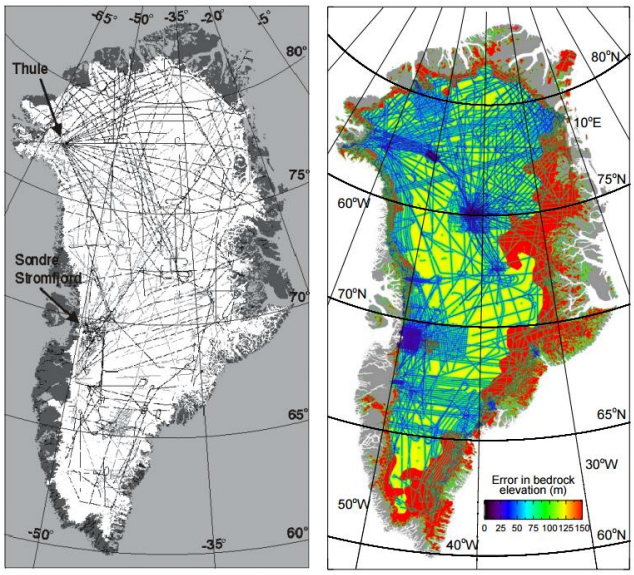

Figure 6: (left) Airborne radar flightlines showing the coverage over the GrIS used in Bamber et al. 2001. (right) RMS error in bed elevation from Bamber et al. (2013). Note that the smallest errors (blue) are in the proximity of the flightlines. The figures are adopted from Bamber et al. (2001) and Bamber et al. (2013).

the basal geometry was improved with the aid of bathymetric data that extends out to the continental shelf (i.e., as far as the maximum glacial extent) (Bamber et al., 2013). The bathymetry was taken from the International Bathymetric Chart of the

Arctic Ocean (IBCAO) v3 (Jakobsson et al., 2012) and represents an interpolation of various bathymetric data from the entire Arctic Ocean. Further, in the Jakobshavn region, the bathymetry was supplemented with additional data from soundings made in the Jakobshavn fjord by CReSIS (Bamber et al., 2013).

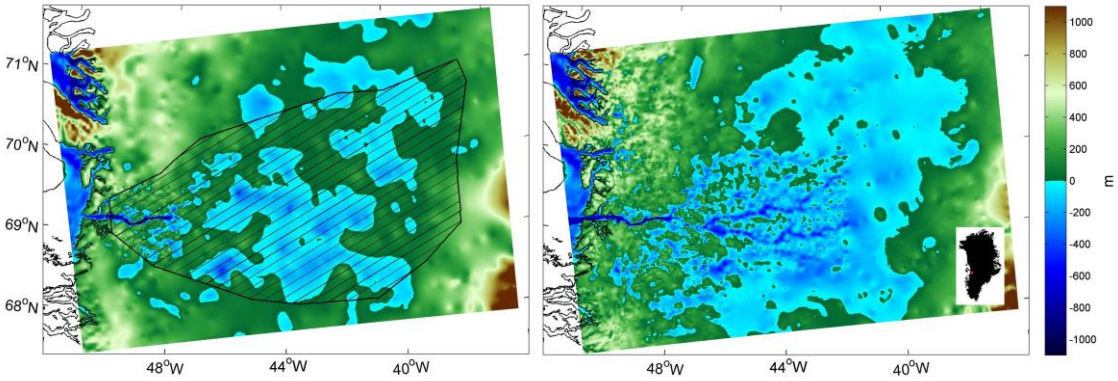

Figure 7: (left) Bedrock topography in the Jakobshavn region according to Bamber et al. (2001a,b) and (right) Bamber et al. (2013). The bed topography from Bamber et al. (2013) provides an improved resolution and better defined troughs for the Jakobshavn region. The black polygon represents the drainage basin mask for JI as computed from the surface DEM.

In Study 2 and 3, I computed the ice thickness as the difference between surface and bedrock elevation. Further, for Study 2 the terminus position and surface elevation in the Jakobshavn region (i.e., from Bamber et al. (2013)) have been adjusted to simulate 1840 terminus and surface elevation based on "historical moraines" (fresh non-vegetated moraines in the proximity of the present glacier ice terminus) and fresh trimlines (pronounced boundaries between abraded and less abraded bedrock on valley sides) (Fig. A2; Csatho et al., 2008; Khan et al. 2014). According to Csatho et al. (2008) these marks were formed at the end of LIA and correspond to the culmination of LIA glacier advances. An identical approach has been used for Study 3 where the terminus position and surface elevation is adjusted to simulate 1990 conditions based on 1985 aerial photographs (Fig. A2; Csatho et al., 2008).

Study 1 is based on the bed topography from Bamber et al. (2001) and Bamber et al. (2013), while Study 2, Study 3 and Study 4 use solely the bed topography from Bamber et al. (2013).

2.4 Observed ice mass change

I estimated the rate of ice volume change using 1997–2014 NASA's Airborn Topographic Mapper (ATM) flights (Krabill, 2014) derived altimetry, supplemented with Ice, Cloud and land Elevation Satellite (ICESat) data (Zwally et al., 2012) for 2003–2009 and Land, Vegetation and Ice Sensor (LVIS) data (Blair and Hofton, 2012) for 2007–2012, CryoSat-2 data (Wouters et al., 2015) for 2010–2014, and European Remote-Sensing Satellite (ERS-2) data during 1997-2003. ATM flight lines in the JI region between 1993 and 1996 cover only a minor transect, and are therefore not used. The procedure for deriving ice surface elevation changes is identical to that presented in Khan et al. (2013) and is similar to the method used by, for example, Ewert et al. (2012) and Smith et al. (2009). However, ice surface elevation changes from cryostat-2 data were derived as described by Wouters et al. (2015) and Helm et al. (2014).

Table 1: Estimated ice mass change rates in Gt a^{-1} from airborne and satellite laser altimetry for 1997– 2014

Time span	Mass change [Gt a^{-1}]
1997–2003	-5.9 ± 2.7
2003–2006	-10.4 ± 1.4
2006–2009	-18.7 ± 1.2
2009–2012	-27.4 ± 1.6
2012–2014	-33.1 ± 2.2

I converted the volume loss rate into a mass loss rate and took firn compaction into account as described by Kuipers Munneke et al. (2015). Further, corrections were made for bedrock movement caused by elastic uplift from present-day mass changes (Khan et al., 2010) and long-term past ice mass changes, Glacial Isostatic Adjustment (GIA), (Peltier, 2004). Table 1 shows the ice mass change rates in Gt a^{-1} during 1997-2014.

2.5 Observed elastic uplift

To estimate site coordinates from GPS measurements, I followed the procedure of Khan et al. (2010). In order to focus on elastic displacements caused by present-day mass variability of the JI, I removed bedrock displacements due to ice mass loss outside JI using load estimates from satellite altimetry (Nielsen et al., 2013) and I removed the GIA based on the deglaciation history ICE-5G (VM2 L90) Version 1.3 estimated by W. R. Peltier.

2.6 Observed horizontal velocities

The observed surface speeds (Joughin et al., 2010) had been derived using Interferometric Synthetic Aperture Radar (InSAR) data from the RADARSAT-1 satellite, Advanced Land Observation Satelitte (ALOS) and TerraSAR-X data. Prior to 2010, the dataset provides annual ice-sheet wide horizontal velocity maps for Greenland for the winters of 2000-2001, 2005-2006, 2006-2007, 2007-2008, and 2008-2009. The mean measurement and processing errors are within 2 m a^{-1} in areas with low surface slope (Joughin et al., 2010). After 2010, almost monthly horizontal velocities are available for the JI region (Joughin et al., 2010).

2.7 Observed terminus positions

The observed terminus positions are from Csatho et al. (2008) (Fig. 8). The terminus history back to LIA was reconstructed from historical records, satellite and aerial imagery, ground surveys, airborne laser altimetry and field mapping of lateral moraines and trimlines (Csatho et al. 2008; Khan et al. 2014). Essentially, the period 1990 to 2012 was mapped from satellite and aerial imagery, ground surveys and airborne laser altimetry. The period prior to 1990 was reconstructed using historical aerial imagery (i.e., 1944, 1953, 1959, 1964 and 1985) and field mapping of lateral moraines and trimlines. The method is detailed in Csatho et al. 2008 and is similar with Khan et al. 2014.

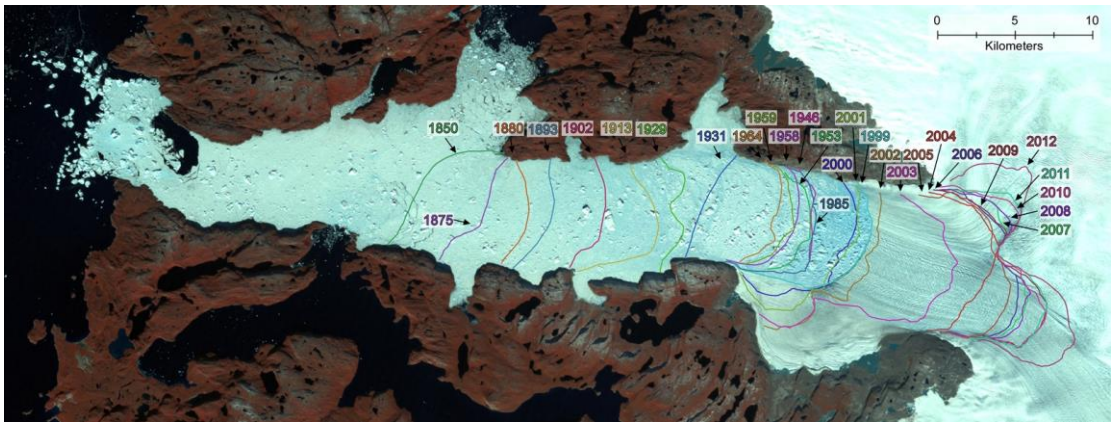

Figure 8: Observed front positions (Csatho et al., 2008) for the period 1840-2012 at JI (Courtesy of Abbas Khan).

2.8 Other data

The model of the geothermal flux was adopted from Shapiro and Ritzwoller (2004). Any ice thickness changes data used in the thesis are from Krabill (2014). In general, any further grid refinements were performed using bilinear interpolation. A second order conservative remapping scheme (Jones, 1999) was used for bed topography data.

CHAPTER 3

Scientific approach

The ice sheet model used in this thesis is PISM (stable version 0.6[2]). PISM is an open source, parallel, three-dimensional, thermodynamically coupled and time dependent ice sheet model (Bueler and Brown, 2009; The PISM Authors, 2014). The field equations and the shallow approximations are solved numerically in PISM by finite differences. The spatial domain is covered by a 3-D rectangular grid which is always divided in equal sized grid cells. In each grid point the differentials are approximated based on differences of the field variables between neighbouring cells. In solving the differences, the size of the grid cells determines the local error and hence, the overall accuracy of the approximation.

PISM core is centred on ice dynamics and lithospheric deformations, where the atmosphere and the ocean can affect the ice dynamics only through well-defined interfaces. At each time step PISM computes the thermal and dynamic state of the ice sheet, and the response of the lithosphere. For computing the ice dynamics and the lithospheric deformations, PISM requires input fields of bed topography, ice thickness, surface elevation and geothermal heat flux. The bed deformation model is based on Lingle and Clark (1985) and Bueler et al. (2007). The model represents a generalized and improved version of the widely used bed deformation model, the flat

[2] Except Study 1 (Sect. 4) where PISM v0.5-88-gc24f74b has been used.

earth Elastic Lithosphere Relaxing Asthenosphere (ELRA) model. Regarding the atmospheric input, I used a one way forcing approach where the ice dynamics model is forced with high quality surface mass balance and air temperature fields (i.e., from BOX, RACMO2 or/and HIRHAM5; Sect. 2.1). From the ocean side, I used a parametrization for ice shelf melting (Sect. 3.6) that requires input fields of surface ocean temperature (Sect. 2.2).

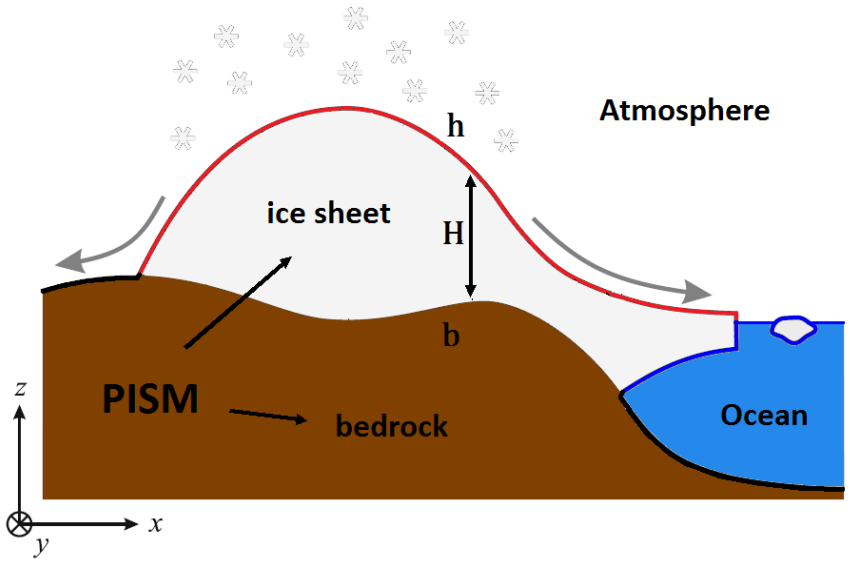

Figure 9: Sketch showing PISM view centred on ice dynamics and lithospheric deformations together with the well-defined interfaces for atmosphere (red) and ocean (blue).

Further, I introduce the main equations that define PISM and that I consider meaningful for understanding the modelling approach and at a later stage, the results obtained. The full description of PISM is available online[3]. Largely, the following sections are based on Greve and Blatter (2009), Paterson and Cuffey (2010) and The PISM Authors (2014).

3.1 Field equations

We treat ice in glaciers as a fluid and therefore, the glacier motion is described by a velocity field. First, we considered ice to be an incompressible fluid (i.e., its density is assumed constant; incompressibility condition):

$$\nabla \cdot \boldsymbol{v} = 0 \qquad (1)$$

where $v(t, x, y, z)$, t represents the time, (x, y) define the horizontal dimensions, and z defines the vertical dimension.

[3] http://www.pism-docs.org/

Secondly, ice is a shear-thinning fluid, where the viscosity depends on the shear rate (i.e., large strain rates imply low viscosity) and thus, the ice flow has a non-Newtonian behaviour. Generally, viscous fluid motion is described by the Navier-Stokes equations. However, ice flow is slow and therefore the forces of inertia (i.e., left hand side of the Navier-Stoke equation) are negligible:

$$0 = -\nabla p + \nabla \cdot \tau_{ij} + \rho_i g \qquad (2)$$

where p is the pressure, τ_{ij} is the deviatoric stress tensor, (i, j) define the two horizontal components, ρ_i is the density of ice, and g is the acceleration due to gravity.

Thirdly, the viscosity is not constant, so an empirical flow law for ice (Nye, 1953) derived based on laboratory experiments is needed (Glen, 1952):

$$\dot{\epsilon}_{ij} = E_{SIA} A \tau^{n-1} \tau_{ij} \qquad (3)$$

where $\dot{\epsilon}_{ij}$ is the strain rate tensor, E_{SIA} is the flow enhancement factor, A is the ice softness term in the Glen flow law, τ is the magnitude of τ_{ij}, and n is the exponent in Glen flow law (n=3). The deviatoric stress tensor can be expressed as:

$$\tau_{ij} = \sigma_{ij} + p\delta_{ij} \qquad (4)$$

with σ being the full stress tensor, p the pressure of the isotropic part of σ and δ_{ij} the Kronecker delta.

The ice softness coefficient, A, is further calculated based on an Arrhenius-type law and holds the form (Paterson and Budd, 1982; Aschwanden et al., 2012):

$$A = \begin{cases} A_c(1 + f\omega)e^{\frac{-Q_c}{RT_{pa}}} & if\ T < T_c, \\ A_\omega(1 + f\omega)e^{\frac{-Q_\omega}{RT_{pa}}} & if\ T \geq T_c, \end{cases} \qquad (5)$$

where A_c, A_ω, Q_c and Q_ω, are constant parameters corresponding to values measured below and above a critical temperature threshold $T_c = -10$ °C (Paterson and Budd, 1982), T represents the ice temperature, ω represents the water content, R is the ideal gas constant, and T_{pa} is the pressure-adjusted temperature calculated using the Clapeyron relation.

The empirical flow law for ice, Eq. 3, can be rewritten in an inverted form as:

$$\tau_{ij} = B\dot{\epsilon}_e^{\left(\frac{1}{n}\right)-1}\dot{\epsilon} \qquad (6)$$

where $B = A^{-\frac{1}{n}}$ and $\dot{\epsilon}_e^2 = \frac{1}{2} tr\left(\dot{\epsilon}_{ij}^2\right)$, with tr representing the trace of the tensor.

While form (3) holds for grounded and slowly moving ice, for ice shelf and ice stream flow a "viscosity" form of the flow law is needed. Knowing that $\tau_{ij} = 2\nu\dot{\epsilon}_{ij}$, the viscosity, ν, can be expressed as:

$$\nu = B\dot{\epsilon}_e^{\left(\frac{1}{n}\right)-1}. \qquad (7)$$

For conservation of energy (i.e., the evolution of temperature within the ice), PISM uses an enthalpy scheme (Aschwanden et al., 2012) that accounts for changes in temperature in cold ice (i.e., ice below the pressure melting point) and for changes in water content in temperate ice (i.e., ice at the pressure melting point):

$$\frac{\partial T}{\partial t} + \boldsymbol{v} \cdot \boldsymbol{\nabla} T = \frac{k}{\rho c}\Delta T + \frac{\nu\,\dot{\epsilon}_e^2}{4\rho c} \qquad (8)$$

where k denotes the thermal conductivity of ice and c represents the ice specific heat capacity.

Solving Eqs. 1, 2, 3 and 7 will provide a full thermodynamic Stoke solution to the problem. However, solving the full Stoke problem generally results in extensively large computational times. Therefore, shallow approximations are employed and widely assumed by ice sheet models, including PISM.

3.2 Shallow Approximations

To approximate the Stokes stress balance (Greve and Blatter, 2009), PISM uses the superposition of the non-sliding shallow ice approximation (SIA; Morland and Johnson, 1980; Hutter, 1983) and the shallow shelf approximation (SSA; Weis et al., 1999) for simulating slowly moving grounded ice in the interior part of the ice sheet, and the SSA for simulating fast-flowing outlet glacier and ice shelf systems (Winkelmann et al., 2011). This superposition of SIA and SSA (the "SIA+SSA" hybrid model) sustains a smooth transition between non-sliding, bedrock frozen ice and sliding, fast-flowing ice, and has been shown to reasonably simulate the flow of both grounded and floating ice (Winkelmann et al., 2011).

I chose not to provide here the whole ensemble of derivations behind the SIA and the SSA, but interested readers can refer to Greve and Blatter (2009) for more details (i.e., Chapter 5 for SIA and Chapter 6 for SSA).

3.2.1 Shallow Ice Approximation (SIA)

To make the problem solvable, the Stoke equations introduced above needed suitable boundary conditions. Boundary conditions for the free surface and the ice base can be computed as detailed in Chapter 5, from Greve and Blatter (2009) (see Eq. 5.21 for the free surface and Eq. 5.31 for the ice base). Based on the hydrostatic approximation (Eq. 5.56 in Greve and Blatter (2009)), the stress balance equation (i.e., Eq. 2) in its tensor component form can be expressed as:

$$\frac{\partial \tau_{xx}}{\partial x} + \frac{\partial \tau_{xy}}{\partial y} + \frac{\partial \tau_{xz}}{\partial z} = \frac{\partial p}{\partial x} \qquad (9a)$$

$$\frac{\partial \tau_{yx}}{\partial x} + \frac{\partial \tau_{yy}}{\partial y} + \frac{\partial \tau_{yz}}{\partial z} = \frac{\partial p}{\partial y} \qquad (9b)$$

$$\frac{\partial \tau_{zx}}{\partial x} + \frac{\partial \tau_{zy}}{\partial y} + \frac{\partial \tau_{zz}}{\partial z} = \frac{\partial p}{\partial z} - \rho_i g. \qquad (9c)$$

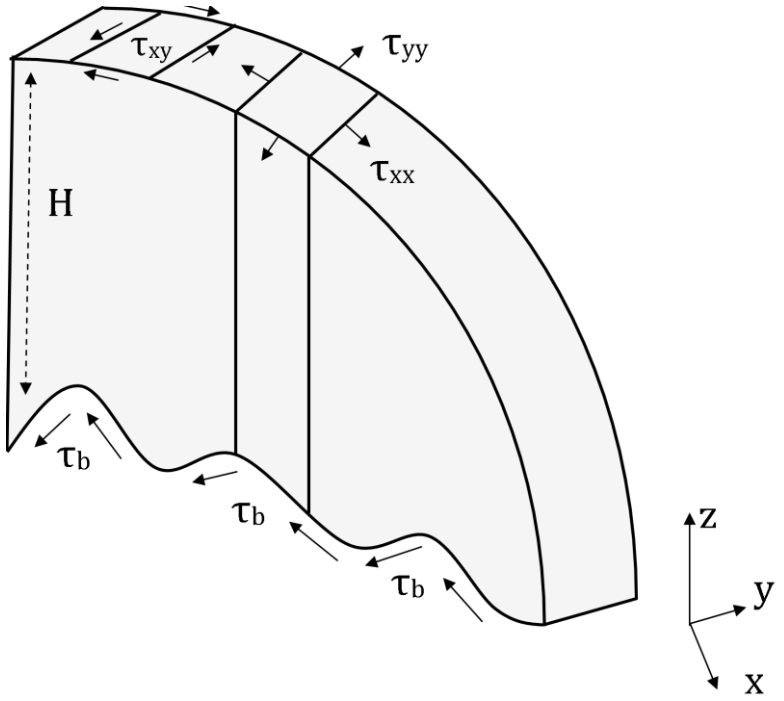

Figure 10: Sketch that shows part of the stress acting on the columns. Adopted from Paterson and Cuffey (2010).

The SIA holds for those regions of the ice sheet where bottom friction is high enough (i.e., such that the vertical shear stresses dominate the horizontal shear and the

longitudinal stresses). Therefore, all the normal stresses, τ_{xx}, τ_{yy} and τ_{zz}, as well as the shear stress in the vertical planes, τ_{xy}, are negligible:

$$\frac{\partial \tau_{xz}}{\partial z} = \frac{\partial p}{\partial x} \qquad (10a)$$

$$\frac{\partial \tau_{yz}}{\partial z} = \frac{\partial p}{\partial y} \qquad (10b)$$

$$0 = \frac{\partial p}{\partial z} - \rho_i g. \qquad (10c)$$

Integrating Eq. 10c gives the pressure distribution:

$$p = \rho_i g\ (h - z) \qquad (11)$$

where h represents the upper surface elevation (Fig. 9).

Introducing Eq. 11 in Eq. 10a and in Eq. 10b holds the expression for the horizontal driving stresses:

$$\tau_{xz} = -\rho_i g(h - z)\frac{\partial h}{\partial x} \qquad (12a)$$

$$\tau_{yz} = -\rho_i g(h - z)\frac{\partial h}{\partial y}. \qquad (12b)$$

Inserting Eq. 13a and Eq. 13b in the generalized form of Eq. 3 allows us to connect the horizontal shears stress with the horizontal velocities as following:

$$\frac{1}{2}\left(\frac{\partial v_x}{\partial z} + \frac{\partial v_z}{\partial x}\right) = E_{SIA} A \tau^{n-1} \tau_{xz} = -E_{SIA} A\ [\rho_i g(h - z)]^n |\nabla h|^{n-1} \frac{\partial h}{\partial x} \qquad (13a)$$

$$\frac{1}{2}\left(\frac{\partial v_y}{\partial z} + \frac{\partial v_z}{\partial y}\right) = E_{SIA} A \tau^{n-1} \tau_{yz} = -E_{SIA} A\ [\rho_i g(h - z)]^n |\nabla h|^{n-1} \frac{\partial h}{\partial y} \qquad (13b)$$

where $\tau = \sqrt{{\tau_{xz}}^2 + {\tau_{yz}}^2} = \rho_i g(h - z)\left[\left(\frac{\partial h}{\partial x}\right)^2 + \left(\frac{\partial h}{\partial y}\right)^2\right]^{\frac{1}{2}} = \rho_i g(h - z)|\nabla h|$.

The horizontal derivatives of the vertical velocity are negligible and integrating Eq. 14a and 14b from the ice base (b) to an arbitrary position (z) in the ice sheet holds:

$$v_x = -2(\rho_i g)^n\ (\nabla h)^{n-1} \frac{\partial h}{\partial x} \int_b^z E_{SIA} A (h - \bar{z})^n\, d\bar{z} \qquad (14a)$$

$$v_y = -2(\rho_i g)^n (\nabla h)^{n-1} \frac{\partial h}{\partial y} \int_b^z E_{SIA} A (h - \bar{z})^n \, d\bar{z}. \qquad (14b)$$

Consequently, the SIA velocity of ice, v_{SIA}, follows :

$$v_{SIA} = -2(\rho_i \mathrm{g})^n |\nabla h|^{n-1} \left[\int_b^z E_{SIA} A (h - \bar{z})^n d\bar{z} \right] \nabla h \, . \qquad (15)$$

Therefore, for SIA, and opposite to SSA (Sect. 3.2.2), the stresses follow directly from the geometry of the ice sheet.

3.2.2 Shallow Shelf Approximation (SSA)

The SSA, as the name suggests, is applied to ice shelves or in regions of the ice sheet where the grounded ice is sliding over a weak base. The dynamics of an ice shelf are relatively different than that of the ice in the interior part of the ice sheet. The first obvious difference is that an ice shelf is characterized by an ice to ocean boundary where the basal friction should be approximately 0, i.e. $\tau_b \approx \tau_{sea} \approx 0$. Therefore, the basal friction is low enough such that the ice deforms uniformly within the entire ice column:

$$\frac{\partial \tau_{xx}}{\partial x} + \frac{\partial \tau_{xy}}{\partial y} + \frac{\partial \tau_{xz}}{\partial z} = \frac{\partial p}{\partial x} \qquad (16a)$$

$$\frac{\partial \tau_{yx}}{\partial x} + \frac{\partial \tau_{yy}}{\partial y} + \frac{\partial \tau_{yz}}{\partial z} = \frac{\partial p}{\partial y} \qquad (16b)$$

$$\frac{\partial \tau_{zz}}{\partial z} = \frac{\partial p}{\partial z} - \rho g. \qquad (16c)$$

Furthermore, the horizontal velocities are independent of depth, and so they only depend on the horizontal coordinates and the time:

$$v_x = v_x(x, y, t), \qquad v_y = v_y(x, y, t). \qquad (17)$$

or

$$\frac{\partial v_x}{\partial z} = 0 \qquad (18a)$$

$$\frac{\partial v_y}{\partial z} = 0. \qquad (18b)$$

The result is a two-dimensional model with a membrane-type of flow (i.e., v_x and v_y are depth-independent). Integrating Eq. 16c gives the pressure distribution:

$$p = \rho_i g\,(h - z) - \tau_{xx} - \tau_{yy}\,. \quad (19)$$

Inserting Eq. 19 in Eq. 16a and 16b holds:

$$2\frac{\partial \tau_{xx}}{\partial x} + \frac{\partial \tau_{yy}}{\partial x} + \frac{\partial \tau_{xy}}{\partial y} + \frac{\partial \tau_{xz}}{\partial z} = \rho_i g \frac{\partial h}{\partial x} \qquad (20a)$$

$$2\frac{\partial \tau_{yx}}{\partial x} + \frac{\partial \tau_{yy}}{\partial y} + \frac{\partial \tau_{xx}}{\partial y} + \frac{\partial \tau_{yz}}{\partial z} = \rho_i g \frac{\partial h}{\partial x}. \qquad (20b)$$

From Eq. 6 and Eq. 7, Eq. 20a and Eq. 20b can be written based on their velocity components:

$$\frac{\partial}{\partial x}\left[2\bar{\nu}\left(2\frac{\partial v_x}{\partial x} + \frac{\partial v_y}{\partial y}\right)\right] + \frac{\partial}{\partial y}\left[\bar{\nu}\left(\frac{\partial v_x}{\partial y} + \frac{\partial v_y}{\partial x}\right)\right] + \frac{\partial \tau_{xz}}{\partial z} = \rho_i g \frac{\partial h}{\partial x} \qquad (21a)$$

$$\frac{\partial}{\partial x}\left[\bar{\nu}\left(\frac{\partial v_x}{\partial y} + \frac{\partial v_y}{\partial x}\right)\right] + \frac{\partial}{\partial y}\left[2\bar{\nu}\left(\frac{\partial v_x}{\partial x} + 2\frac{\partial v_y}{\partial y}\right)\right] + \frac{\partial \tau_{yz}}{\partial z} = \rho_i g \frac{\partial h}{\partial y}\,. \qquad (21b)$$

where $\bar{\nu}$ represents the vertical-averaged viscosity. The vertical-averaged viscosity is calculated as:

$$\bar{\nu} = \frac{\bar{B}}{2}\,(E_{SSA})^{-\frac{1}{n}}\left[\frac{1}{2}\dot{\epsilon}_{ij}\dot{\epsilon}_{ij} + \frac{1}{2}\dot{\epsilon}_{ij}^2\right]^{\frac{1-n}{2n}} \qquad (22)$$

where $\bar{B}$ is the vertically-averaged ice hardness, and E_{SSA} is the flow enhancement factor for the SSA.

Integrating over the entire column, the stress balance for the SSA is obtained:

$$\frac{\partial}{\partial x}\left[2\bar{\nu}\,H\left(2\frac{\partial v_x}{\partial x} + \frac{\partial v_y}{\partial y}\right)\right] + \frac{\partial}{\partial y}\left[\bar{\nu}\,H\left(\frac{\partial v_x}{\partial y} + \frac{\partial v_y}{\partial x}\right)\right] + \tau_{b_x} = \rho_i g H \frac{\partial h}{\partial x} \qquad (23a)$$

$$\frac{\partial}{\partial x}\left[\bar{\nu}\,H\left(\frac{\partial v_x}{\partial y} + \frac{\partial v_y}{\partial x}\right)\right] + \frac{\partial}{\partial y}\left[2\bar{\nu}\,H\left(\frac{\partial v_x}{\partial x} + 2\frac{\partial v_y}{\partial y}\right)\right] + \tau_{b_y} = \rho_i g H \frac{\partial h}{\partial x} \qquad (23b)$$

where H represents the ice thickness and $\left(\tau_{b_x}, \tau_{b_y}\right) = \tau_b$ define the basal shear stress.

Finally, the horizontal velocities, $\boldsymbol{v}$, are computed in PISM as the sum of $\boldsymbol{v}_{SIA}$ and $\boldsymbol{v}_{SSA}$:

$$\boldsymbol{v} = \boldsymbol{v}_{SIA} + \boldsymbol{v}_{SSA}. \qquad (24)$$

In a nutshell, the SIA describes the vertical shear stress as a local function of the driving stress and is known to perform relatively well for grounded parts of the ice sheet that have a strong connection with the bed, and that are characterized by planar bed topography. The SSA describes a membrane-type flow, that performs relatively well for those regions of the ice sheet that are floating, or where the grounded ice is sliding over a weak base (i.e., $\tau_b \approx 0$).

3.3 Basal sliding

The basal shear stress is related to the sliding velocity by a nearly-plastic power law (Schoof and Hindmarsh, 2010):

$$\tau_b = -\tau_c \frac{\boldsymbol{u}}{u_{threshold}^{q} |\boldsymbol{u}|^{1-q}} \qquad (25)$$

where τ_c is the till yield stress, $\boldsymbol{u}$ is the model sliding velocity, $u_{threshold}$= 100 m a^{-1} represents the velocity threshold, and q is the exponent of the pseudo-plastic basal resistance model. This nearly-plastic power law is most useful at the basal boundary, where the geothermal flux varies in space (Shapiro and Ritzwoller, 2004).

The yield stress is determined by models of till material property (the till friction angle, ϕ) and is based on the effective pressure on the saturated till. The Mohr-Coulomb criterion (Cuffey and Paterson, 2010) is used to relate the saturation, yield stress (τ_c), and the model liquid water within the till:

$$\tau_c = c_0 + \tan(\phi) N_{till} \qquad (26)$$

where c_0=0 kPa is the till cohesion, ϕ is the till fraction angle and N_{till} is the effective pressure. The till fraction angle (ϕ) is computed as a piecewise-linear function of the bed elevation, with ϕ = 15° for bed elevations lower than 300 m below sea level, with ϕ = 40° for bed elevations higher than 700 m above sea level, and in between values with a linear change:

$$\phi(x,y) = \begin{cases} \phi_{min}, & b(x,y) \le b_{min} \\ \phi_{min} + [b(x,y) - b_{min}] \cdot M, & b_{min} < b(x,y) < b_{max} \\ \phi_{max,} & b_{max} \le b(x,y). \end{cases} \qquad (27)$$

The effective pressure on the till is determined by the modelled amount of water in the till:

$$N_{till} = \delta P_o 10^{(e_0/C_c)(1-(W_{till}/W_{till}^{max}))} \qquad (28)$$

where δ is the till effective fraction overburden, e_0 = 0.69 is the till reference void ratio, C_c = 0.12 is the till compressibility coefficient, P_o is the ice overburden pressure, W_{till} is the effective thickness of water in the till computed by time-

integrating the basal melt rate and W_{till}^{max} = 2 m is the maximum effective thickness of the water stored in the till. In this subglacial hydrology model the water is not conserved and the excess water drains when the effective thickness of the water stored in till exceeds W_{till}^{max}. This model is based on the "undrained plastic bed" concept of Tulaczyk et al. (2000). The ice flow therefore develops in PISM, as a consequence of plastic till failure, i.e. where the basal shear stress exceeds the yield stress, and is influenced by the thermal regime and the volume of water at the ice-sheet bed.

Changes in mass balance are communicated to the ice flow through the mass continuity equation:

$$\frac{\partial H}{\partial t} = M - S - \nabla \boldsymbol{Q} \qquad (29)$$

where H is the current modelled thickness, t is the current time, M and S are the surface and basal mass balance, and $\boldsymbol{Q}$ is the flux.

Table A2, Table A3, Table A5, Table A6, Table A11, Table A12 and Table A14 provide values of the parameters altered from the default PISM values during the different studies performed.

3.4 Calving

The physics at the calving front are boundary condition modifications to the mass continuity and to the SSA stress balance equations. Three types of calving were used in my simulations. For whole GrIS runs and in Study 1, I removed ice in the open ocean according to the present-day thickness. Any ice shelf that developed during the simulations in ocean grid cells marked as ice free at the beginning of the run was calved. In general, when this simple calving condition is used, the terminus position remains fixed to the present-day position.

In Study 2, 3 and 4, I used a more physically based approach, where I applied the superposition of a physically based calving (eigencalving) parametrization (Winkelmann et al., 2011; Levermann et al., 2012) and a basic calving mechanism (Albrecht et al., 2011) that removes at a rate of at most one grid cell per time step, any floating ice at the calving front thinner than a given threshold. The benefit of using such a combination of calving laws is that it can evolve the terminus position with time under the applied forcings and thus, potential calving feedbacks are not ignored.

The average calving rate (c) is calculated as the product of the principal components of the horizontal strain rates ($\dot{\varepsilon}_{\pm}$), derived from SSA velocities, and a proportionality constant parameter (k) that captures the material properties relevant for calving:

$$c = k\dot{\varepsilon}_{+}\dot{\varepsilon}_{-} \quad \text{for } \dot{\varepsilon}_{\pm} > 0. \qquad (30)$$

The strain rate pattern is strongly influenced by the geometry and the boundary conditions at the ice shelf front (Levermann et al., 2012). The proportionality constant, k, is chosen such that the ice front variability is small (Leverman et. al., 2012). This physically based calving law appears to yield realistic calving front positions for various types of ice shelves being successfully used for modelling calving front positions in whole Antarctica simulations (Martin et al., 2011) and regional east Antarctica simulations (Mengel and Levermann, 2014) but has never been used with success for the GrIS. In contrast to Antarctica, known for its large shelves and shallow fjords, the GrIS is characterized by narrow and deep fjords, and JI makes no exception. The strain rate pattern in the eigen calving parametrization performs well only if fractures in glacier ice can grow, and calving occurs only if these rifts intersect (i.e., possible only for relatively thin ice shelves). In my model, the eigen calving law has priority over the basic calving mechanism. That is to say, the second calving law used (the basic calving mechanism) removes any ice at the calving front not calved by the eigen calving parametrization, overall thinner than 500 m. Therefore, the creation of the conditions under which calving can occur with the subsequent calving mechanism (e.g. a floating ice shelf) relies solely on the parametrization for ice shelf melting (Sect. 3.6).

A partially-filled grid cell formulation (Albrecht et al., 2011), which allows for sub-grid scale retreat and advance of the ice shelf front is used to connect the calving rate computed by the calving parametrizations with the mass transport scheme at the ice shelf terminus. This sub-grid scale retreat and advance of the shelf allows for realistic spreading rates, important for the eigen calving parametrization. The sub-grid interpolation is performed only when a floating terminus exists. In both situations (i.e., floating ice or grounded terminus) the stress boundary conditions are applied at the calving front and in the discretization of the SSA equations (Winkelmann et al., 2011). The retreat and advance of the front through calving (valid for both calving mechanisms) is restricted to at most one grid cell length per adaptive time step.

3.5 Parametrization for grounding line migration

The parameterization of the grounding line position is based on a linear interpolation scheme (the “LI” parameterization; Gladstone et al., 2010) extended to two

horizontal dimensions (x, y). This sub-grid treatment of the grounding line interpolates the basal shear stress in x, y based on the spatial gradient between cells below and above the grounding line, and allows for a smooth transition of the basal friction from grounded to floating ice (Feldmann et al., 2014). At each time step the grounding line position is determined by a mask that distinguishes between grounded and floating ice using a flotation criterion based on the modelled ice thickness (Winkelmann et al., 2011):

$$b(x, y) = -\frac{\rho_i}{\rho_o} H(x, y) \qquad (31)$$

where ρ_i is the density of the ice, ρ_o is the density of the ocean water and H represents the ice thickness. Therefore, the grounding line migration is influenced by the ice thickness evolution, which further depends on the velocities computed from the stress balance. The superposition of SIA and SSA (Eq. 24), ensures that the stress transmission across the grounding line is continuous and that buttressing effects are included.

3.6 Parameterization for ice shelf melting

I used a parametrization for ice shelf melting where the melting effect of the ocean is based on both sub-shelf ocean temperature and salinity (Martin et al., 2011). To accommodate this parametrization several changes have been made in PISM at the sub-shelf boundary (Winkelmann et al., 2011). First, the ice temperature at the base of the shelf (the pressure-melting temperature) is calculated based on the Clausius-Clapeyron gradient and the elevation at the base of the shelf, and is applied as a Dirichlet boundary condition in the conservation of energy equation:

$$T_{pm} = 273.15 + \beta_{cc} z_b \qquad (32)$$

where $\beta_{cc} = 8.66 \times 10^{-4}$ K m^{-1} represents the Clausius-Clapeyron gradient and z_b represents the elevation at the base of the ice shelf.

Second, basal melting and refreezing is incorporated through a sub-shelf mass flux used as a sink/source term in the mass-continuity equation. This mass flux from shelf to ocean (Beckmann and Goosse, 2003) is computed as a heat flux between the ocean and ice, and represents the melting effect of the ocean through both temperature and salinity (Martin et al., 2011):

$$S = \frac{Q_{heat}}{L_i \rho_i} \qquad (33)$$

$$Q_{heat} = \rho_o c_{p_o} \gamma_T F_{melt} (T_o - T_f) \qquad (34)$$

where $L_i = 3.35 \times 10^5$ J kg^{-1} is the latent heat capacity of ice, $c_{p_o} = 3974$ J (kg K)$^{-1}$ is the specific heat capacity of the ocean mixed layer, $\gamma_T = 10^{-4}$ m s^{-1} is the

thermal exchange velocity, F_{melt} is a model parameter, T_o is the ocean water temperature (here equivalent with the SST introduced in Sect. 2.2 and Fig. 5) and T_f is the virtual temperature. This virtual temperature represents the freezing temperature of ocean water at the depth z_b below the ice shelf and has the form:

$$T_f = 273.15 + 0.0939 - 0.057S_o + 7.64 \times 10^{-4} z_b \qquad (35)$$

where S_o is the salinity of the ocean. In the heat flux parametrization, the ocean temperature at the ice shelf base is computed as the difference between the input ocean temperature and a virtual temperature that represents the freezing point temperature of ocean water below the ice shelf (Eq. 34). The freezing point temperature is calculated based on the elevation at the base of the shelf and the ocean water salinity (Eq. 35).

Figure 11 shows possible ice shelf temperatures as a function of the elevation at the base of the shelf.

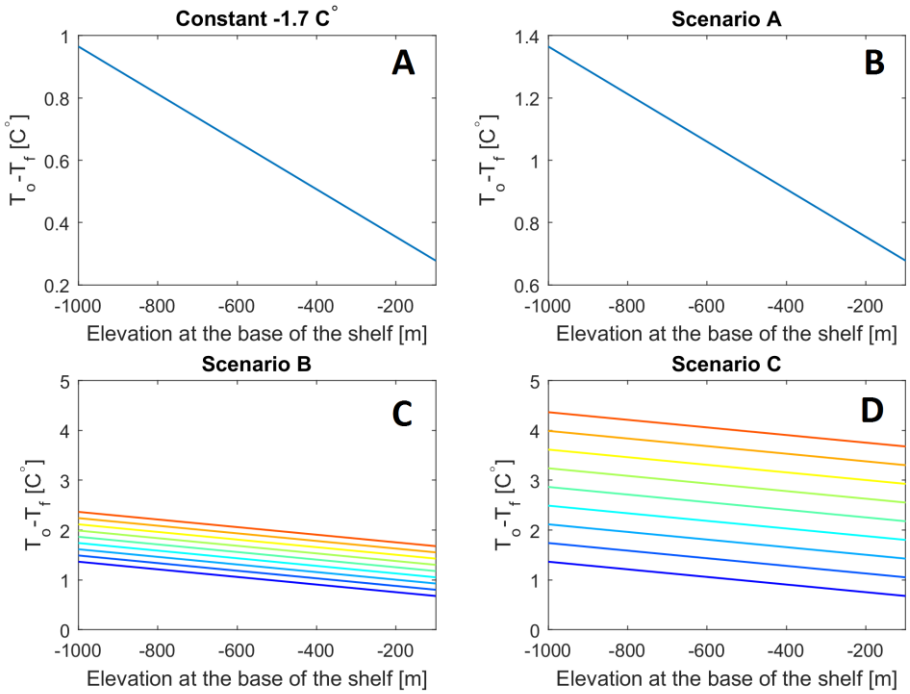

Figure 11: Ocean temperatures at the ice shelf base illustrated for different possible elevations at the base of the shelf and different surface ocean temperature scenarios (i.e., (A) Constant -1.7 °C, (B) Scenario A, (C) Scenario B, and (D) Scenario C). In (C) and (D) the colour scale denotes the 10 year intervals (10×9) used between 2010 (blue) and 2100 (red; Sect. 2.2).

In consequence, as the glacier retreats and/or advances, both the pressure-melting temperature and the heat flux between ocean and ice evolve alongside the modelled glacier ice shelf geometry. The ocean water salinity ($S_o = 35$ psu) is kept constant in

time and space as the model does not capture the salinity gradient from the base of the ice shelf through layers of low and high salinity. A previous study conducted by Mengel and Levermann (2014) using the same model established that the sensitivity of the melt rate to salinity is negligible.

Following this melting parametrization, the highest melt rates are modelled in the proximity of the glacier grounding lines and decrease with elevation (Fig. 11) such that the lowest melt rates are closer to the central to frontal area of the modelled ice shelf. At the grounding line, PISM computes an extra flotation mask that accounts for the fraction of the cell that is grounded by assigning 0 to cells with fully grounded ice, 1 to cells with ice-free or fully floating ice, and values between 0 and 1 to partially grounded grid cells. The basal melt rate in the cells containing the grounding line is then adjusted based on this flotation mask as follows (the PISM Authors, 2014):

$$M_{b,adjusted} = \lambda M_{b,grounded} + (1 - \lambda) M_{b,shelf-base} \qquad (36)$$

where M_b refers to the basal melt rate and λ is the value of the flotation mask. At the vertical ice front, I do not apply any melt.

3.7 Initialization procedure and regional modelling

In my model, the three-dimensional ice enthalpy field, basal melt, modelled amount of till-pore water, and lithospheric temperature are obtained from an ice-sheet-wide paleo-climatic spin-up. At this initialization stage, I considered a paleo-climatic spin-up and a "force to thickness" (FTT) spin-up. Disregarding the method used, I chose to spin-up for 125 kyr in order to provide my regional Jakobshavn regional model with stress boundary and thermodynamic initial conditions dependent on the long-term memory of the ice sheet (Huybrechts and de Wolde, 1999; Rogozhina et al., 2011). In Study 1, I spin-up with yearly mean 1960-1990 climate for RACMO2 and BOX, and mean 1989-1990 climate for HIRHAM5. In Study 2, I spin-up with yearly mean 1840-1900 climate, while in Study 3, I spin-up with yearly mean 1960-1990 climate (Table 2). While the paleo-climatic spin-up follows closely the SeaRISE initialization procedure described by Bindschadler et al. (2013), the FTT spin-up is based on the same procedure except that, additionally, the modelled ice thickness is constrained during the last 5000 years of the simulation to the present-day thickness. The mass balance correction procedure is described in Aschwanden et al. (2013). Both methods are detailed in the above mentioned citations and I invite the readers to read additional information therein (see also Appendix B1). As a rule of thumb, I start the spin-up on a 10 km grid, and then I refine to 5 km at -5ka. It is important to note that during the paleo-climatic and the "FTT" initialization the terminus is always held fixed to the observed position from Bamber et al. (2013).

To identify the Jakobshavn glacier drainage basin (DB) and its corresponding regional domain, I used the Python drainage-basin-delineation tools developed in PISM for this purpose. The algorithm is based on a simple concept: ice flows down the surface gradient. To identify the drainage basin, the user is required to supply a Digital Elevation Model (DEM) and to select a rectangle that approximates the glacier terminus. The basin drainage mask for JI is included in Fig. 1B. In order to isolate the dynamics of a single glacier from other fast flowing basins nearby, PISM applies a mass balance correction outside of the drainage basin mask (The PISM Authors, 2014). This way, the area, and thus the dynamics inside the drainage basin mask, will be able to evolve freely in time, while the area outside the drainage basin will be kept near the present-day geometry (Figs. 1B and 12).

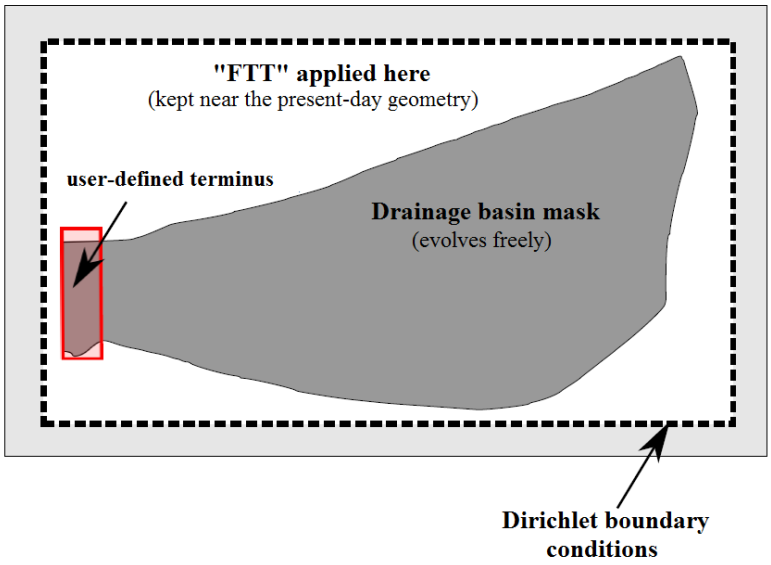

Figure 12: A regional model domain in PISM. Adopted from Della-Giustina (2011).

In the regional outlet glacier model of PISM, the boundary conditions are handled in a 10 km strip positioned outside of the JI's drainage basin and around the edge of the computational domain (Figs. 1B and 12). In this strip, the input values of the basal melt, the amount of till-pore water, ice enthalpy, and lithospheric temperature from the paleo-climatic spin-up are held fixed and applied as Dirichlet boundary conditions in the conservation of energy model (The PISM Authors, 2014). I started my regional JI runs with an equilibrium simulation on a 125 × 86 horizontal grid with 5 km spacing. The enthalpy formulation modelled the mass and energy balance for the three-dimensional ice fluid field based on 200 regularly spaced layers within the ice. The temperature of the bedrock thermal layer was computed up to a depth of 1000 m with 50 regularly spaced layers. The first step was to obtain a 5 km regional equilibrium model for JI using constant mean climate (i.e., repeating the 1960-1990

or 1989-1990 mean air temperature and SMB for Study 1, repeating the 1840-1900 mean air temperature and SMB for Study 2, and repeating the 1960-1990 mean air temperature and SMB for Study 3). I considered that equilibrium has been established when the ice volume in the regional domain changed by less than 10 % in the final 100 model years. Grid refinements are made from 5 km (125×86) to 2 km (310×213) after 3000 years. In Study 1, the simulations reached equilibrium after 200 years with an ice volume increase that varies from 1 % and 10 % between the different simulations. In Study 2 and 3, the 2 km simulations reached equilibrium after 200 years with ~4 % increase relative to the input dataset from Bamber et al. (2013) adjusted to simulate 1840 and 1990 terminus positions and surface elevation, respectively. Further, using my equilibrium simulations with a 2 km horizontal grid and 400 regularly spaced layers within the ice, I simulated forward in time (hindcast) from 1840 or/and 1990 to 2012 or/and 2014 by imposing monthly fields of SMB and 2 m air temperatures through a one-way forcing scheme. For simulations performed on a 1 km horizontal grid, the exact same procedure was used with the mention that in the regional equilibrium run an additional grid refinement from 2 km to 1 km was made after 200 years. The length of the 1 km regional equilibrium simulation was 100 years.

The prognostic simulations (projections) were performed for the period 2013-2100 on a 2 km grid and were built as a continuation of the historical simulations performed in Study 2 (Sect. 5), both for constant and varying ocean temperature. To ensure a smooth transition in air temperature and SMB between the BOX climate used in Study 2 and the RCP projections (Sect. 2.1.2) used in Study 4, I computed and forced the latter as anomalies with respect to the mean 2000-2010 BOX air temperature and SMB (Peter Langen, personal communication).

In Study 1, I allowed only the upper and lower surfaces to evolve. In Study 2, 3 and 4 all the boundaries (calving fronts, grounding lines, upper and lower surfaces) were free to evolve in time both during the regional equilibrium and the forward simulations.

3.8 Summary

Overall, I performed a wide range of simulations from whole GrIS paleo-climate spin-ups that provided boundary conditions for my regional simulations, to regional JI runs that included equilibrium, forward and prognostic simulations. I started my simulations with a calving criterion that favoured a fixed terminus position and ended by using the superposition of two calving mechanisms that allowed the terminus to advance and/or retreat under the applied climate forcing. I performed

well over 200 simulations which I further divided in Study 1, Study 2, Study 3 and Study 4. A summary of these simulations is introduced in Table 2.

Table 2: Summary of simulations for Jakobshavn Isbræ. The bed topography from Bamber et al. (2001) is abbreviated with v1 and the bed topography from Bamber et al. (2013) with v2. The forward simulations are performed only on a 2 km grid unless otherwise indicated by asterisks (*). The simulations signalized with "*" are performed both using 1 km and 2 km grids. The initialization, equilibrium and forward simulations are detailed in Sect. 3.7. "FTT" refers to the "force to thickness" mechanism (see Sect. 3.7).

Study no.	Initialization	Regional Jakobshavn Isbræ simulations							
		Bedrock topography	Equilibrium simulations (mean climate)	Forward simulations					
				Year	Terminus	Ocean forcing	HIRHAM5	RACMO2	BOX
Study 1	(I) paleo climatic FTT spin-up	v1	1989-1990 or 1960-1990	1990-2012	Fixed	No	Rv1FTT-H90-12	Rv1FTT-R90-12	Rv1FTT-J90-12
		v2			Fixed	No	Rv2FTT-H90-12	Rv2FTT-R90-12	Rv2FTT-J90-12
	(II) paleo climatic spin-up	v1	1989-1990 or 1960-1990	1990-2012	Fixed	No	Rv1-H90-12	Rv1-R90-12	Rv1-J90-12
		v2			Fixed	No	Rv2-H90-12	Rv2-R90-12	Rv2-J90-12
		v2	1990-2000		Fixed	No	Rv2-H90-12*	-	-
Study 2	(II) paleo climatic spin-up	v2	1840-1900	1840-2012	Movable	Constant+Variable[1]	-	-	1840-2012
Study 3	(II) paleo climatic spin-up	v2	1960-1990	1990-2014	Movable	Constant[1]	-	1990-2014	-

	Projections					
	Year	Terminus		Climate	RCP	Abreviation
Study 4	2010-2100	Movable	Constant+Variable[1]	HIRHAM	4.5	1840-2100BH4.5
	2010-2100	Movable	Constant+Variable[1]	HIRHAM	8.5	1840-2100BH8.5

[1] Please refer to Sect. 2.2 for ocean water temperature scenarios.

CHAPTER 4

Study 1: Paleo spin-up and initial simulations with the regional model

In this first study, I performed a suite of simulations which include paleo-climatic and "FTT" spin-ups, regional equilibrium and forward simulations using RACMO2, HIRHAM5 and BOX as climate forcing. I spin-up for 125 kyr using yearly mean 1960-1990 climate for RACMO2 and BOX, and 1989-1990 climate for HIRHAM5. Along the ice shelf calving front, I applied a calving condition that removed ice in the open ocean according to the present-day thickness (Bamber et al., 2013). When this simple calving condition is used, the terminus remains fixed to the position from Bamber et al. (2013) both during the paleo climate, regional equilibrium and forward simulations. Therefore, the study allowed only the upper and lower surfaces to evolve freely. Please note, that my purpose here was neither to study initialization methods sensitivities nor to find limitations of these methods but rather to find a suitable initialization method for my regional domain based on the existing literature. Previous studies (e.g. performed with PISM) have already largely addressed these points and interested readers can refer

to Aschwanden et al. (2013) and Aðalgeirsdóttir et al. (2014) for more details. The values of the ice sheet model parameters used (see Sect. 3 for the underlying equations) are included in Table A2 and Table A3.

4.1 Paleo and "FTT" spin-ups

As seen in Fig. 13, the paleo-climatic spin-up tends to overestimate the ice thickness near the coastline for each of the three atmospheric forcings used, while the "FTT" mechanism, as expected, provides a better agreement with observed ice thickness. Nonetheless, the general modelled ice thickness pattern seems to remain widely unchanged, except maybe the very proximity of the coastline where the paleo-climatic spin-up tends to overestimate the ice thickness. Differences in ice thickness are also modelled in NE Greenland, where BOX tends to overestimate the ice thickness, and SE Greenland where both RACMO2 and BOX overestimate the ice thickness.

The observed and modelled velocities (Fig. 14) look similar: the model seems to capture the ice divides in the central region of the GrIS but generally underestimates the fast flow in the main outlet glaciers. In the north eastern side of the GrIS (NEGIS) the magnitude of the flow is better captured when BOX is used as atmospheric forcing (over 1500 m a^{-1} of increase in the terminus area relative to HIRHAM5). Changes in SMB affect both the SIA (Eq. 15) and the SSA (Eq. 23) but the effect in the SIA is very weak as the driving stresses are not affected by a few meters of difference in thickness induced by SMB variability. In the SSA, the coupling is done via the effective pressure term in the definition of the yield stress (Eq. 26). In my model, the effective pressure is determined by the ice overburden pressure (i.e., ice thickness) and the effective thickness of water in the till. Relative to SIA, this effect is much stronger and favours the idea that in this particular model some velocity peaks could potentially be influenced by changes in SMB (e.g. potentially larger changes in BOX relative to RACMO2 and HIRHAM5). Further, the air temperatures represent boundary conditions for the enthalpy equation (Aschwanden et al., 2012). The long time span covered by the paleo simulations can allow advection/diffusion to propagate down into the column and to reach the high shearing layer at the base of the ice. Consequently, higher air temperatures (e.g. in BOX relative to RACMO2 and HIRHAM5; Fig. 3) could potentially soften the ice and enhance sliding.

Overall, in the JI region, both methods and all atmospheric forcings used seem to generate, at least from a large scale perspective, the same behaviour with respect to modelled ice thickness and horizontal velocities. Nonetheless, as my region of interest is Jakobshavn glacier, I chose to further investigate more closely atmospheric forcing sensitivities for the JI region only.

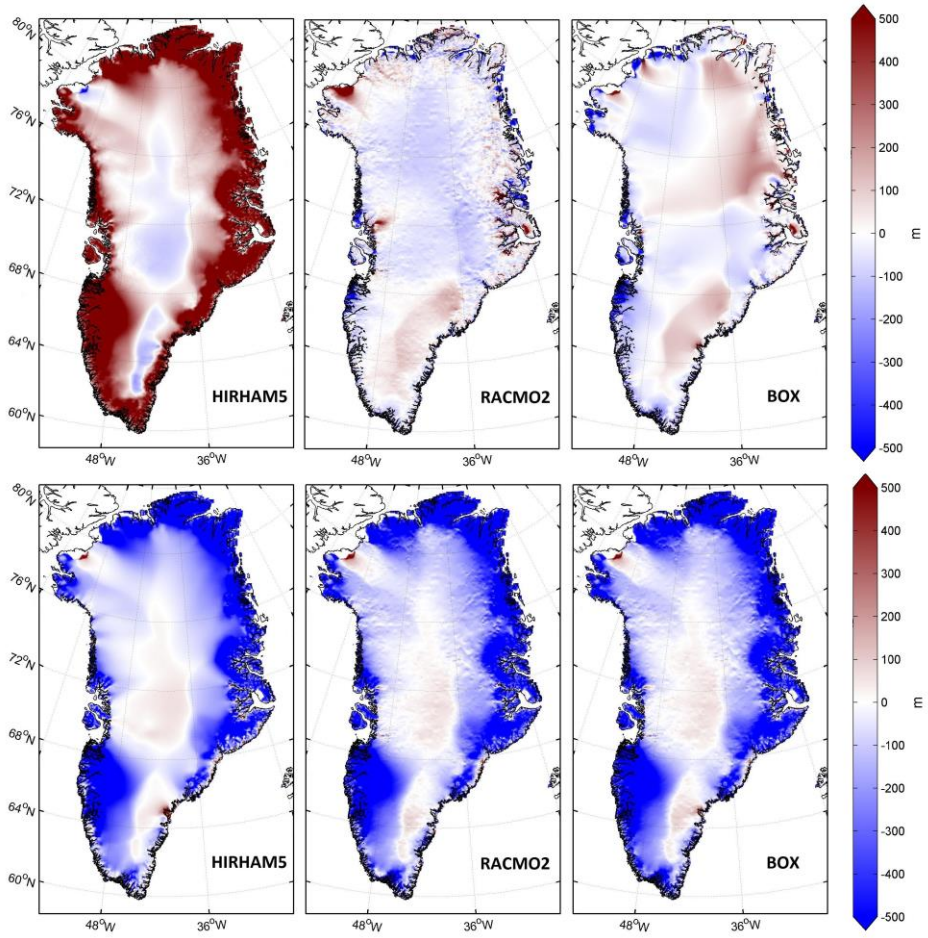

Figure 13: Differences in ice thickness for HIRHAM5 (HO=modelled HIRHAM5-observations), RACMO2 (modelled RACMO2 - observations - HO) and BOX (modelled BOX - observations - HO) at the end (~1989) of the paleoclimate spin-up (top row) and FTT paleo-climate spin-up (bottom row) on a 5 km grid. The initializations without the FTT mechanism overestimate the ice thickness at the margins of the ice sheet. The observed ice thickness is from Bamber et al. (2013).

4.2 Initial Jackobshavn Isbræ regional runs

In this section, I introduce some results obtained in the initial runs performed with the regional model. The purpose of these runs is to provide an insight in the regional model performance with and without the "FTT" mechanism and define atmospheric forcing and bed topography sensitivities, if any. Throughout these simulations, as in case of the whole GrIS spin-ups, I used the simple calving mechanism, which keeps the terminus stable to the present day position. Consequently, only the upper and lower surfaces are free to evolve in time both during the regional equilibrium and the forward simulations, and there is no input from the ocean side.

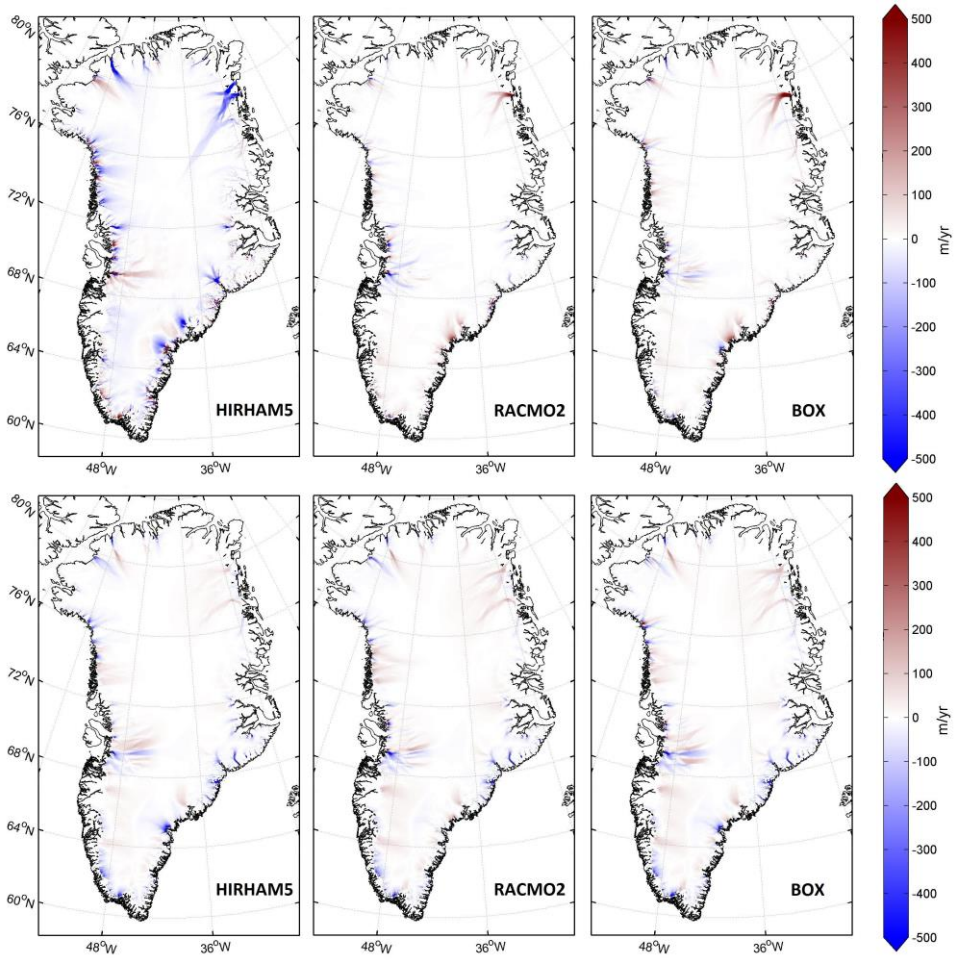

Figure 14: Differences between modelled and observed surface velocities for HIRHAM5 (HO=modelled HIRHAM5-observations), RACMO2 (modelled RACMO2 - observations - HO) and BOX (modelled BOX - observations - HO) at the end (~1989) of the paleoclimate spin-up (top row) and FTT paleo-climate spin-up (bottom row) on a 5 km grid. The observed surface velocities are from Joughin et al. (2010).

My overall goal here was to evaluate the modelled present-day JI sensitivity to three climatology datasets (i.e., RACMO2, HIRHAM5 and BOX), two bedrock topographies (Bamber et al. (2001) and Bamber et al. (2013)) and assess the ability of the regional outlet glacier model to realistically transform atmospheric forcing into simulated mass loss. For this purpose, I designed an ensemble of 14 simulations based on common spin-up methods (with and without FTT), bed topographies, and widely used climatic datasets for modelling and projecting the GrIS and JI mass loss. A summary of these simulations is given in Table 2 (see Study 1). I validated the model by comparing model results for horizontal surface velocities, ice thickness, and mass loss time series with existing observations (Sect. 2).

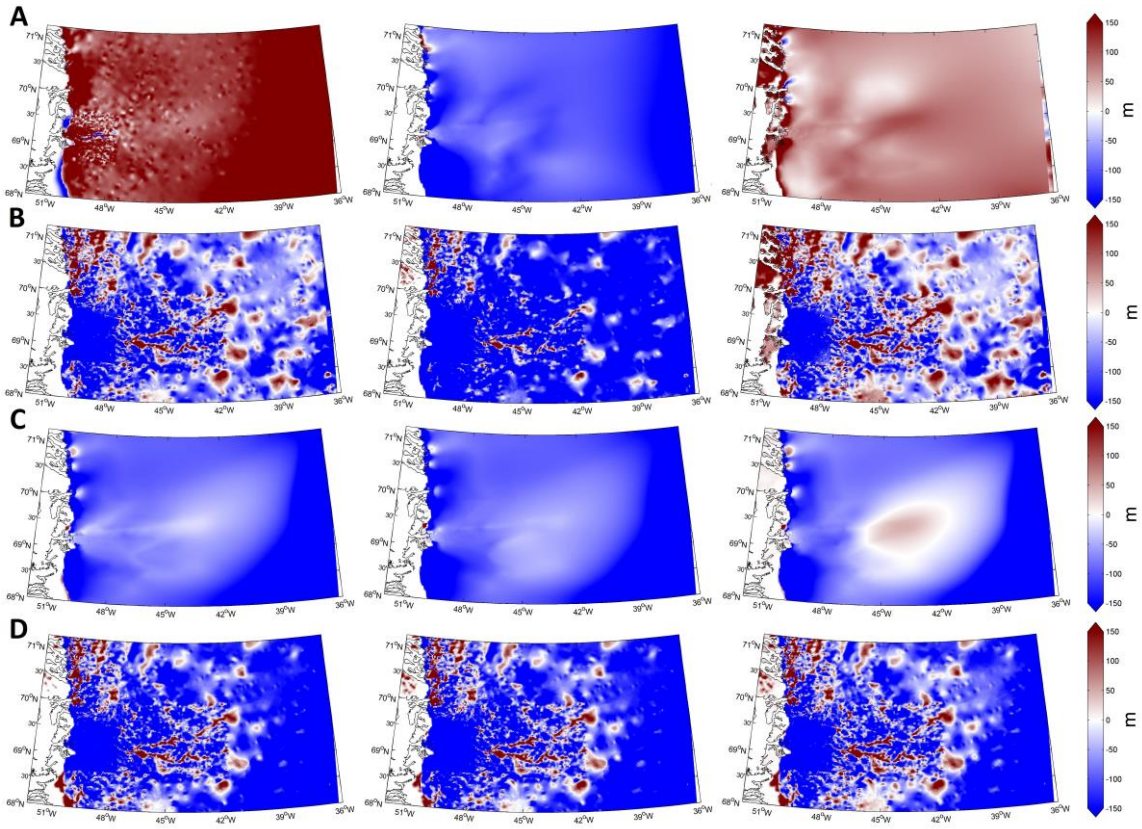

Figure 15: Differences in ice thickness on a 2 km grid at the end of a forward simulation (1990-2012) for bedmap v.1 (rows A and C) and bedmap v.2 (rows B and D), without (rows A and B) and with (rows C and D) the FTT mechanism for HIRHAM5 (model-observation), RACMO2 and BOX.

Figure 15 shows differences in ice thickness between the model and the observations on a 2 km grid at the end of the forward simulation, which for this particular runs correspond to 2012. Overall, a better agreement with observations is obtained when the bed geometry from Bamber et al. (2013) is used (note that "bed geometry" refers here to both bed topography and ice thickness; Table A4). The best fit with the observed ice thickness is achieved with the bed geometry from Bamber et al. (2013) and HIRHAM5 as climate forcing in experiment Rv2-H90-11 (RMSE 93 m, AMD 60, $\bar{o}$ = 1997, $\bar{m}$ = 1980). Differences in ice volume between the model and the observations reach up to 10 % in the experiments that are using the bed from Bamber et al. (2001), for example in experiment Rv1-J90-11 (with a modelled ice volume of 0.6 [10^6 km^3] and an observed ice volume of 0.55 [10^6 km^3]). When the bed geometry from Bamber et al. (2013) is used, the differences are reduced and range between 1 % - 5 %.

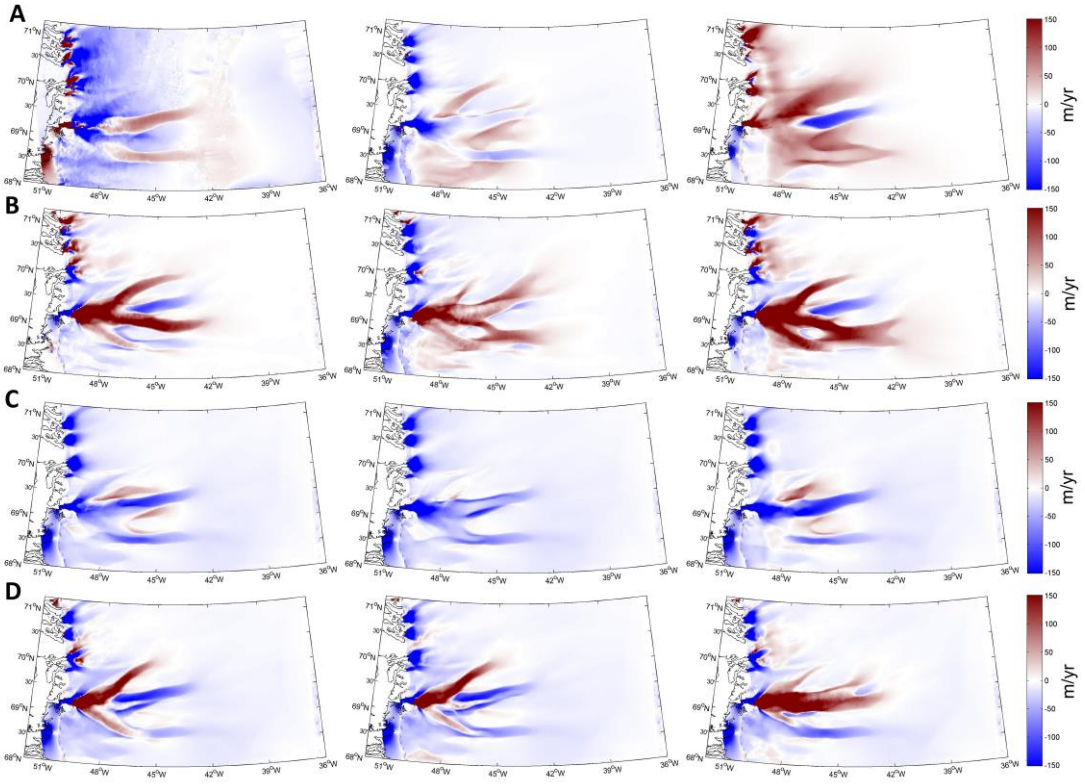

Figure 16: Differences in horizontal surface velocities on a 2 km grid at the end of a forward simulation (1990-2012) for (rows A and C) the bed topography from Bamber et al. (2001) and for (rows B and D) the bedrock topography from Bamber et al. (2001), without the FTT mechanism (rows A and B) and with the FTT mechanism (rows C and D) for HIRHAM5 (model-observation), RACMO2 and BOX.

Overall, when the "FTT" mechanism is used, a better agreement with observations is obtained. In the experiments without the "FTT" mechanism, the overall trend is to overestimate the ice thickness towards the end of the domain. In general, both with and without the "FTT" mechanism, two distinct patterns can be observed in my simulations: when the bed geometry from Bamber et al. (2001) is used, the trend is to underestimate the ice thickness in the main channel of JI and overestimate the ice thickness elsewhere in the domain, while for the bed geometry from Bamber et al. (2013), the trend is to underestimate the thickness for the entire terminus region and overestimate the ice thickness in some of the troughs that extend deep into the ice sheet (Fig. 15). The terminus region and the narrow and deep troughs that define JI represent the area where the two bed datasets are most different (Fig. 7). While the bed geometry from Bamber et al. (2001) underestimates the depth in these troughs, the dataset from Bamber et al. (2013) provides an improved and more recently mapped bed topography and ice thickness of JI. This bed geometry (i.e., Bamber et al. (2013)) is overall characterized by better defined troughs and consequently ice thickness slopes.

In terms of velocities (Figs. 16, 17 and 18), similar behaviours are modelled with and without the "FTT" mechanism. However, I should stress here that with the "FTT" on, the mean modelled velocities ($\overline{m}$) are 40 % to 50 % smaller than the mean observed velocities ($\overline{o}$). Overall, the trend is to underestimate the velocities in the terminus region when the bed from Bamber et al. (2001) is used, and overestimates the velocities in the main troughs when the bed from Bamber et al. (2013) is employed. The best agreement with observed surface velocities was obtained in experiment Rv2-R90-11 with the bed from Bamber et al. (2013) and RACMO2 as the climate forcing (RMSE 155 m a^{-1}, AMD 35, $\overline{o}$ = 53, $\overline{m}$ = 49). All the simulations performed with the bed from Bamber et al. (2001) tend to underestimate the high velocities close to the terminus area. Overall, a better agreement with the observed horizontal velocities is obtained when the bed geometry from Bamber et al. (2013) is used (Table A4).

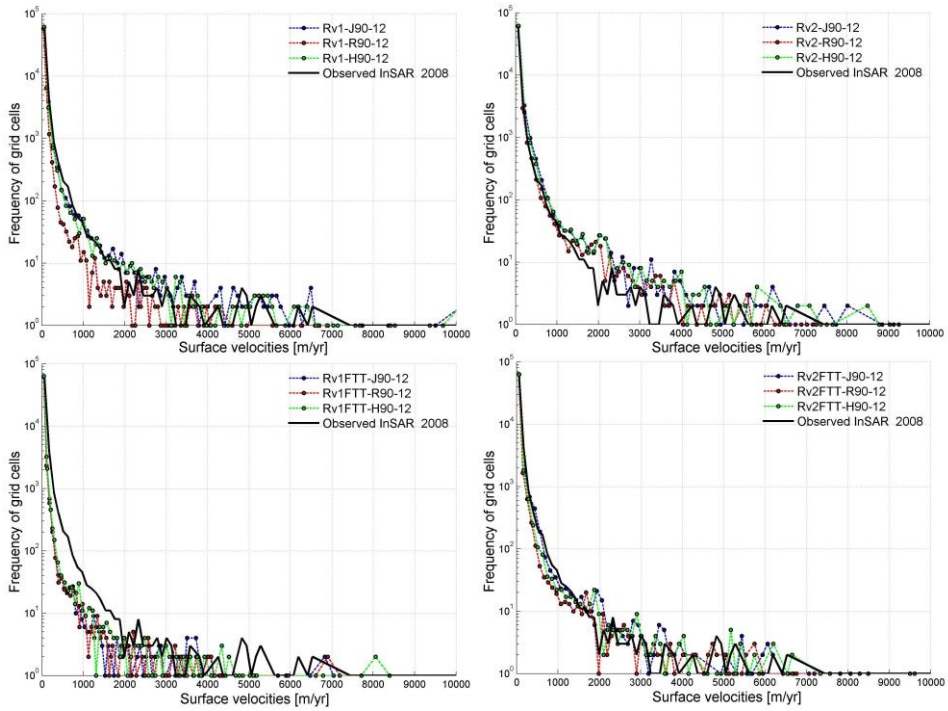

Figure 17: Distribution of modelled and observed surface velocities on a 2 km grid at the end of the forward simulation (~2012) for HIRHAM5 (green), RACMO2 (red) and BOX (blue) for the two bed topographies used, with and without the FTT mechanism. The observed velocities are for the winter of 2008-2009 and are based on the ice-sheet wide horizontal velocity map (Joughin et al., 2010).

The sensitivity of the modelled horizontal velocities and ice thickness relative to the three climate dataset used (i.e., HIRHAM5, RACMO2, and BOX) is not as significant as for the bedrock geometry or the spin-up method used. However, both

RACMO2 and HIRHAM5 are forced at the lateral boundaries based on the ERA-Interim product and the BOX reconstruction is further correlated with RACMO2. Overall a better agreement with the observed behaviour is obtained when the regional outlet glacier model is forced with RACMO2.

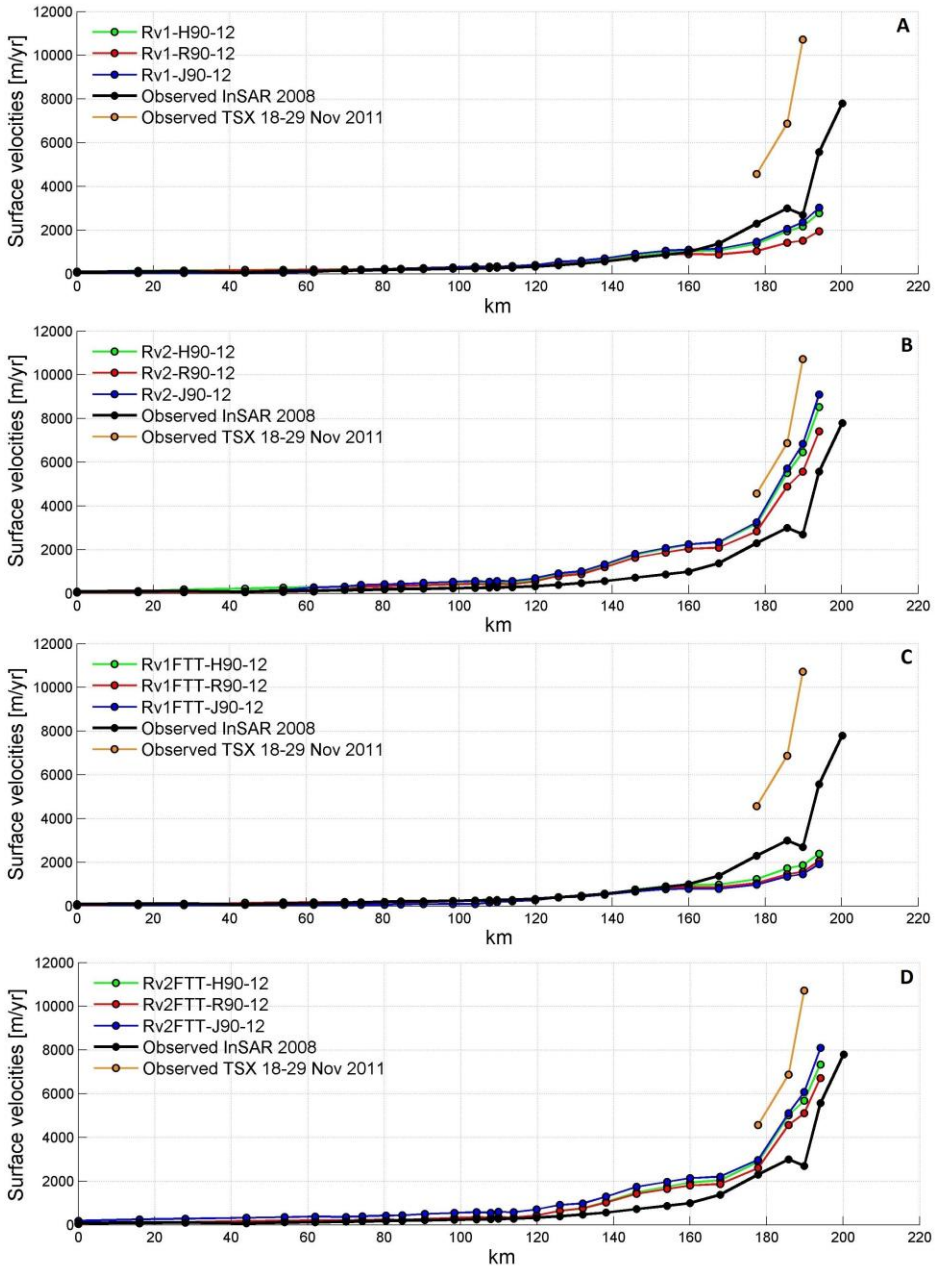

Figure 18: Simulated flow-line ice divide to terminus on a 2 km grid at the end of the forward simulation (~2012) for the bed topography from Bamber et al. (2001) (A, C) and Bamber et al. (2013) (B, D) without FTT (A, B) and with the FTT mechanism (C, D) for HIRHAM5 (green), RACMO2 (red) and BOX (blue). The observed TSX 18-29 Nov 2011 horizontal velocities are produced from TerraSAR-X (TSX) image pairs collected between 18 and 29 November 2011 (Joughin et al., 2010).

Figure 19 shows observed versus modelled monthly cumulative mass change time series for the period 1997-2012 on a 2 km grid.

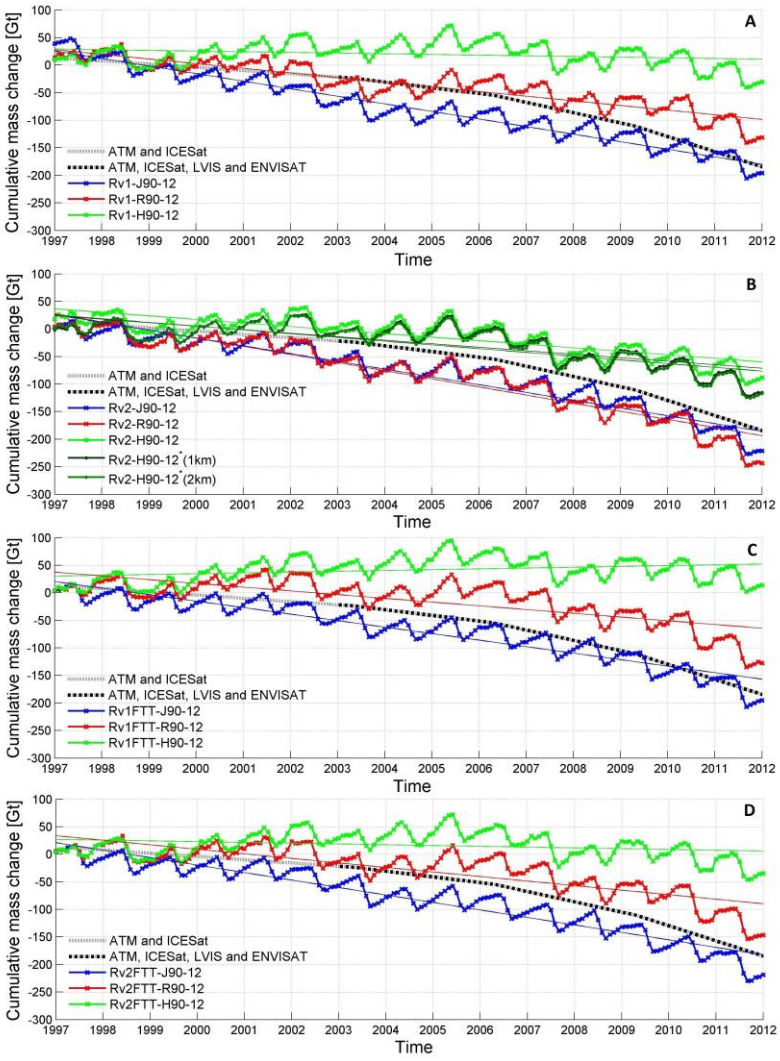

Figure 19: Simulated monthly cumulative mass loss (1997-2012) on a 2 km grid with their respective trend lines versus observed cumulative mass loss (1997-2012) for the bed geometry from Bamber et al. (2001) (A, C) and for Bamber et al. (2013)(B, D), without FTT (A, B) and with the FTT mechanism (C, D) for HIRHAM5 (green), RACMO2 (red) and BOX (blue). The dark green line (1 km, Rv2-H90-12*) represents the modelled cumulative mass loss where yearly mean 1990-2000 climate for HIRHAM5 was used during the regional equilibrium simulation. Note that Rv2-H90-12* performed on 1 km and Rv2-H90-12* performed on 2 km are superimposed over the period 1997-2012 (Table A4).

As a rule of thumb, I always removed the drift by subtracting the mass loss modelled during the control simulation (i.e., where a constant 1960-1990 or 1989-1990 climate is used) from the forced simulation (forward runs) mass loss on a

time-step (monthly) basis (Gupta et al., 2012). The simulated cumulative mass loss after drift removal is presented in Table A4.

4.3 Discussion

The approach used allowed me to evaluate the three climatic datasets from a glacier internal dynamic perspective. For these initial set of experiments, the terminus positions remained fixed and in consequence the modelled dynamic response of JI due to advance and/or retreat of the front was negligible. Consequently, the modelled ice thickness, horizontal velocities and mass loss estimates were solely influenced by glacier internal dynamics and the atmospheric forcing applied (Sect. 2). I found large variations in the simulated mass loss relative to the climate model used (up to ~155 Gt, simulations Rv2-H90-12 and Rv2-R90-12), the spin-up method (up to ~67 Gt, simulations Rv2-R90-12 and Rv2FTT-R90-12) but also relative to the bed topography used (up to ~112 Gt, simulations Rv1-R90-12 and Rv2-R90-12).

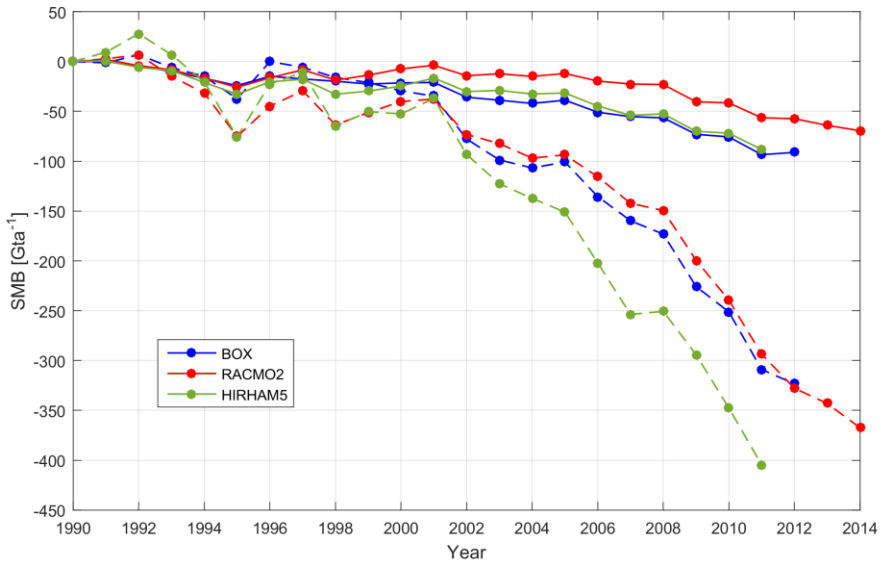

Figure 20: The mass change due to SMB for BOX (blue line), RACMO2 (red line) and HIRHAM5 (green line) for the whole computational domain (dashed line) and in the mask showed in Fig. 1B (solid line). For BOX and RACMO2, I removed the 1960-1990 baseline.

In terms of simulated mass loss, the modelled results versus observations agree well until 2000 (Fig. 19). Starting in 2001, the simulations with HIRHAM5 tend to underestimate the mass loss trend. The same trend is better captured when RACMO2 is used and overestimated when the model is forced with BOX (Fig. 19). The differences in mass loss become evident mainly after 2000, when according to observations an increase in mass loss caused by surface processes is reported (i.e., 22 % increase for the period 2009-2012 relative to period 2003-2006; Khan et al., 2014). Therefore, this disagreement between the three climatic datasets modelled

after 2000 could be potentially generated by differences in the absolute values for precipitation and surface melting with the subsequent run-off. This hypothesis seems plausible as all the models (HIRHAM5, RACMO2 and BOX) are able to capture the temporal behaviour before 2000, when the mass loss was dominated by dynamically driven discharge (Nick et al., 2013). However, when analysing the SMB forcing used for the period 1990-2014, HIRHAM5 and BOX present similar trends (see Fig. 20, i.e. the solid lines), while RACMO2 suggests up to 20 Gt less SMB loss.

I could reduce the uncertainty by building anomalies with respect to the reference period 1961–1990, as a 30 year average is considered a meaningful climatology (van den Broeke et al., 2009), but this is not possible for my experiments, as HIRHAM5 covers only the period 1989–2012. Further, I ran two additional simulations with a 1 km and a 2 km grid using HIRHAM5 as the climate forcing, but this time using a mean 1990–2000 climate for my initial and regional equilibrium simulations. The results are presented in Fig. 19B. I found that by integrating forward in time using an initial state and regional equilibrium simulation based on a 10 year average HIRHAM5 climate, I am able to increase the simulated mass loss by 29 Gt (from 88.29 Gt to 116.89 Gt). Therefore, I am inclined to suggest that the mismatch in the modelled mass loss relative to BOX and RACMO2, may be caused by the different input climatic data used in the initialization (i.e., mean 1961-1990 climate for RACMO2 and BOX, and mean 1989-1990 climate for HIRHAM5). Alternatively, the mismatch may also be generated by the different distribution of SMB loss within the domain (see Figs. 2 and 3) or due to the fact that the model (i.e., the parameters) was initially calibrated based on simulations performed with BOX. BOX and RACMO2 are correlated (Fig. 20), and therefore the good agreement between the two is expected. However, the uncertainty involved in estimating the mass balance components (van den Broeke et al., 2009) for 1990–2012 and the different formulations of the models is generally the reason for the differences observed in the simulated mass loss estimates.

The difference between modelled and observed behaviour varies significantly between the experiments (Table A4). My simulations show a large sensitivity of the modelled horizontal surface velocities and ice thickness to the bed topography used and less significant to the climate forcing applied (Figs. 15, 16, 17 and 18). An improvement for all the experiments is observed when the bed from Bamber et al. (2013) is used. Even in this relatively simple model, where any buttressing effects due to advance and retreat of the terminus are neglected as the terminus remains fixed, the influence of bed topography and improved ice thickness can be easily acknowledge. In terms of the spin-up method used, the prediction errors are reduced when the "FTT" mechanism is used. However, the tendency with the "FTT" is to underestimate the surface velocities and the ice thickness, which may

finally lead to an underestimation of the ice discharge (Figs. 15 and 16). In terms of the grid resolution used, I did not found differences in the modelled mass loss between simulations performed with a 1 km and a 2 km grid (Fig. 19B).

Based on the above results, I chose to perform all my further simulations without the "FTT" mechanism and to use the bed topography from Bamber et al. (2013). The benefits for using the "FTT" mechanism are not enough to sustain its further use. The "FTT" mechanism introduces a series of limitations e.g. at each time step the ice thickness is forced to the present day thickness without a legitimate physical reason. Therefore, I found the "FTT" mechanism unsuitable for modelling past temporal variability or for performing prognostic runs that allow the advance and/or retreat of the terminus.

Previous studies, but based on a flowline approach (Vieli et al., 2011; Nick et al., 2013), have suggested that representing the processes that act at the marine boundary (i.e., calving and ocean melt) are important for understanding and modelling the retreat and/or advance of marine terminating glaciers like JI. Therefore, all further simulations include the superposition of two calving mechanisms (Sect. 3.4) that allow for glacier terminus advance and retreat due to calving.

CHAPTER 5

Study 2: Jakobshavn Isbræ numerical simulations (1840-2012)

The goal of this study is to model the behaviour of JI since the end of the Little Ice Age (LIA; 1840-2012). I forced the model with yearly atmospheric forcing (i.e., air temperature and SMB from BOX; Fig. 2) and I used both constant (i.e., -1.7 °C) and variable surface ocean water temperature (see Sect. 2, Fig. 5). The input surface ocean water temperature represents here (Sect. 3.6) the mean surface ocean temperature in the grid cells adjacent to the JI terminus (i.e., T_o in Eq. 34). In this regional model, all boundaries (calving fronts, grounding lines, upper, and lower surfaces) were free to evolve in time both during the regional equilibrium and the forward simulations. Along the ice shelf calving front, I superimposed a physically based calving (eigen-calving) parametrization (Winkelmann et al., 2011; Levermann et al., 2012) and a basic calving mechanism (Albrecht et al., 2011) that allowed the glacier terminus to advance and retreat under the applied forcings. The values of the ice sheet model parameters used (see Sect. 3 for the underlying equations) are included in Table A5 and Table A6.

I started my simulations with a constant surface ocean temperature and I altered parameters controlling the ice dynamics in the regional equilibrium simulations (e.g. the flow enhancement factor, the exponent of the pseudo-plastic basal resistance

model, the till effective fraction overburden, etc.) and parameters related with ice shelf melt, ocean temperature, and calving (i.e., the ice thickness threshold in the basic calving mechanism) in the forward simulations. Consequently, these parameters were modified only during the regional JI runs. In order to reproduce observed frontal positions (~15 positions for the period 1900-2012), I performed approximately 100 regional JI simulations.

I further performed additional simulations with variable surface ocean temperature as taken from the Met Office Hadley Centre dataset (Sect. 2.2), which I then adjusted (see Fig. 5) to accurately match the observed trend in mass change for the period 1997-2012. At this stage, I did not altered any parameters (i.e., all the parameters have the same values as used in the constant ocean forcing simulations).

From these results, I will present here the two simulations (i.e., with constant and variable surface ocean temperature) that best captured (i.e., I estimated the residual between modelled and observed ice mass change and selected the smallest residual signal) the full observed evolution of JI during the period 1840–2012 (see Fig. A10). I validated the model by comparing model results for horizontal surface velocities, ice thickness changes, and mass loss time series with existing observations (Sect. 2.4). However, it should be considered that before the ‘90s the available observations are relatively sparse in time and space, and often uncertain, making the validation of the model difficult.

This is the first study, to my knowledge, that aims and succeeds to capture with a 3-D dynamic numerical model the temporal behaviour of JI since the end of the LIA. The study is unique both in approach and results obtained. The study is associated with Paper iii (manuscript) attached in Appendix H.

5.1 Observations vs. modelling results

5.1.1 1902-1946

Observations suggest that the terminus of JI retreated significantly from 1850. The observations available during this period are based on trimlines and field campaigns made to the glacier by early Danish explorers (e.g. Engell). Engell, which visited the glacier several times, suggests thinning over the period ~1850-1902 (Csatho et al., 2008). These observations are in agreement with my modelling results (see Figs. 21 and 22B). During this period, the ocean forcing that I used at the terminus is constant and leads in my model to gradual thinning of JI and terminus retreat without any shift (i.e., increase) in ocean temperature. In my model, the terminus continues to retreat until ~1915 when the retreat is halted and the terminus remains relatively stable for the next ~10 years. The available scientific literature for this period is relatively limited but does suggest large surface lowering that increases towards the interior of the ice sheet (e.g. Csatho et al., 2008). Starting in 1920, the modelled terminus retreat and modelled flow speed of JI accelerates (Figs. 21 and 22). During this period (i.e.,

1925-1932), JI develops in my simulations a larger ~2-4 km floating tongue, which is calved off by the end of 1932. Thereafter, only a small floating ice tongue is modelled. Following the retreat of the terminus, the simulation produces speeds high as 20 km a^{-1}. This first modelled terminus retreat (~8 km) and flow acceleration of JI that occurs in ~1930 is triggered as the grounding line retreated over a reversed bed slope (Fig. 21A,C). The magnitude of this modelled flow acceleration is similar with that of modelled present day accelerations of JI (e.g. 2003; Figs. 21, A6 and A7).

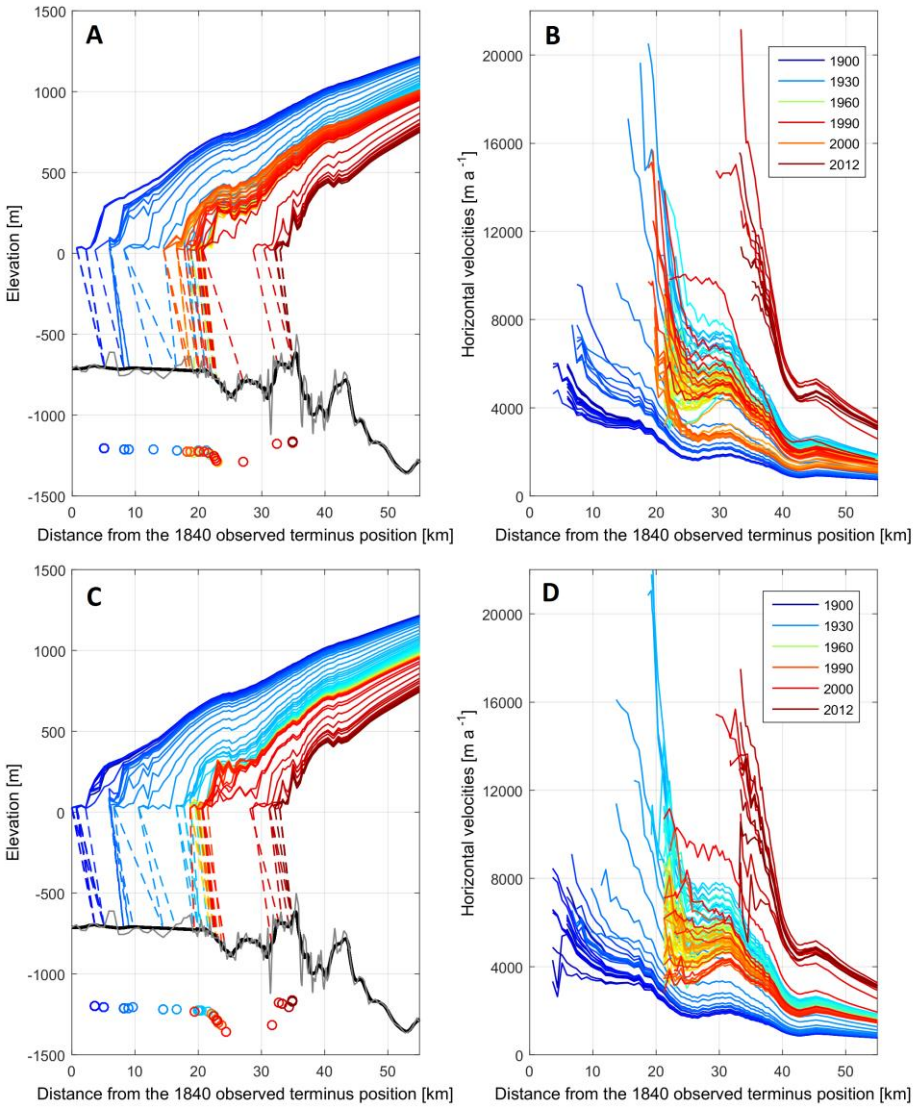

Figure 21: Modelled surface elevation (> 50 m) and grounding line position (A) and modelled horizontal velocities (B) at JI along the dotted flowline shown in Fig 1D in a simulation with variable surface ocean temperature for the period 1900-2012. The black line represents the bedrock topography from Bamber et al. (2013) and the grey line represents a smoothed version of the same bed topography. Modelled surface elevation (> 50 m) and grounding line position (C) and modelled horizontal velocities (D) at

JI in a simulation with constant surface ocean temperature (i.e., -1.7 °C) for the period 1900-2012. The colour scale ranges from dark blue (1900), light blue, green (1960), yellow, orange to red (2012) (see the legend). The dots represent modelled grounding line positions where the colours follow closely the colour scale presented above. Note the acceleration in speed between 1925-1930 and between 1998-2003 corresponding to the final breakup of the floating tongue.

However, and in contradiction with present day JI flow accelerations, this acceleration is short lived and once the grounding line reached higher ground (~1935), the modelled velocities decreased but still remained slightly larger than those simulated before the acceleration (~50 % increase in point S1; Fig. 22). In my simulations, this initial acceleration of JI is responsible for large surface lowering (Fig. 22B), and may explain the surface lowering documented by Weidick (1969) and Csatho et al. (2008) during this period. Although, there is observational evidence to confirm the large terminus retreat (e.g. terminus positions for 1931 and 1946; Csatho et al. (2008)), this initial flow acceleration of JI is not documented in any other scientific publication.

Weidick (1969) suggests based on observations of lichen colonies and moraines near the lake Nunatap Tasia (i.e., close to JI's 1930 terminus) that the surface lowering was intermittent and stops once JI enters its cooling phase (~1950; Figs. 2 and 5). In agreement with Weidick, after 1940, the modelled terminus remains relatively stable with no episodes of modelled terminus retreat, thinning or flow acceleration (Figs. 21 and 22). A similar behaviour is modelled in the simulation performed with constant ocean forcing suggesting that most probably, in my model, calving at the terminus is reduced because JI grounding line reached a pinning point (see Fig. 21). These model results agree well with observations (e.g. Csatho et al. (2008)), which suggest that this location (i.e., near the Ice Rumple, Fig. 11 in Csatho et al. (2008)) represents a pinning point for JI until 1998.

5.1.2 1946-1997

After 1940s, the modelled terminus positions remain relatively stable (Figs. 21 and 22) but JI continues to lose mass until the 70's when the climate begins to cool (Figs. 2, 5, 22B and 26). As a result of colder climatic conditions (i.e., 0.5 °C decrease in ocean temperature; Fig. 5), in the simulation with variable ocean forcing, the glacier is slightly thickening and the terminus advances by ~2-4 km between 1980 and 1990. In agreement with my modelling results, observations (Csatho et al., 2008) suggest that thickening started at JI most probably in mid-1980s. Overall, during the period 1946-1997, the modelled frontal extent and the grounding line position remain relatively stable (Figs. 21 and 22), a result that is consistent with observations (Csatho et al., 2008). Similarly, this behaviour remains unchanged even if a constant ocean forcing is applied at the terminus suggesting that most probably the bed geometry played an essential role during this period.

Figure 23 shows observed and modelled horizontal velocities for 1985, 1988 and 1989. Although, the modelled horizontal velocities for this period are slightly larger than the observed horizontal velocities (e.g. RMSE 2988.6 m a^{-1} for 1985), the difference in speed is significant only in the grid cells adjacent to JI's terminus (see Fig. A6).

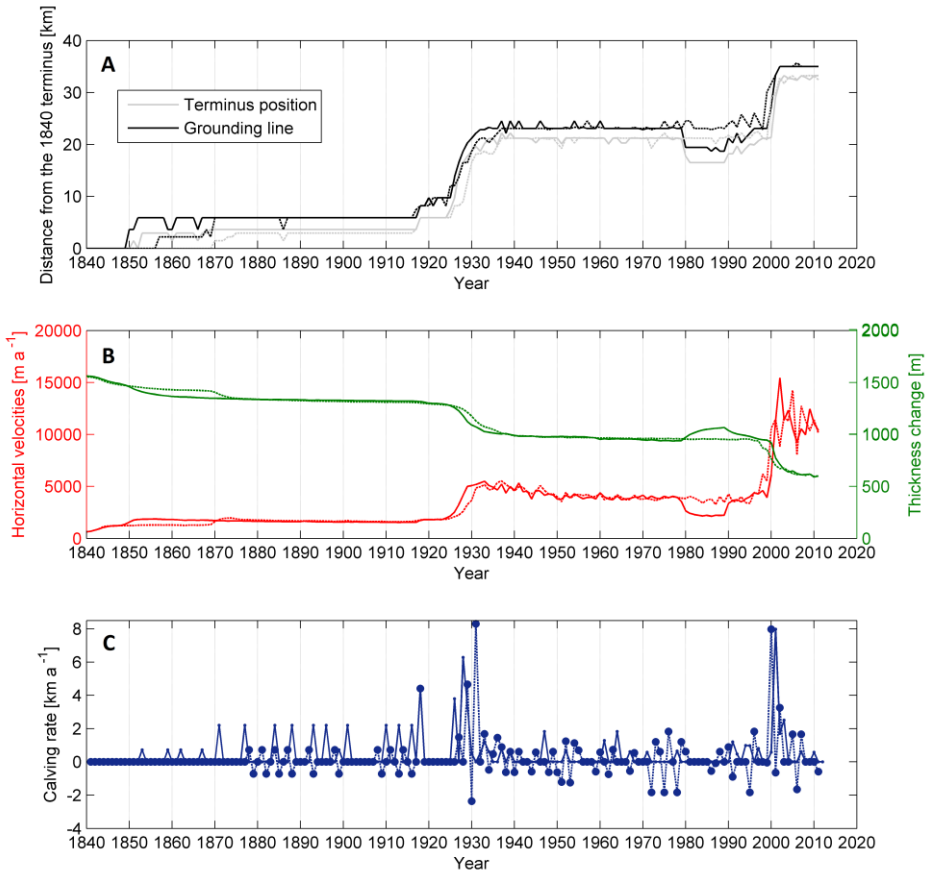

Figure 22: (A) Modelled grounding line and terminus position (floating ice tongues thinner than 50 m are not shown). (B) Modelled horizontal velocities and ice thickness changes at the point location S1 shown in Fig. 1C. (C) Modelled calving rates in km a^{-1} for the period 1840-2012.

Csatho et al. (2008) suggested that JI's terminus may have become afloat sometimes after 1946. A larger floating ice tongue starts to develop in my simulations in ~1870, ~1920 and ~1980. Generally, these modelled ice tongues are shorter lengthwise than those suggested by observations (Csatho et al., 2008). Beside the 1870 floating ice tongue which is calved only in ~1915, the 1920s and 1980s ice tongues are calved within several years after their development (Fig. 21). After 1990, only a small floating ice tongue is modelled (<2 km; Figs. 21 and 22) and the simulated terminus retreat tends to follow closely the modelled grounding line retreat.

5.1.3 1998-2012

According to observations (Joughin et al., 2004; Luckman and Murray, 2005; Motyka et al., 2011; Bevan et al., 2012), the first post-1990 acceleration of JI occurred in 1998, which coincides with my modelled results. In my simulation, the acceleration, starts a year later, in 1999, and is sustained until 2003.

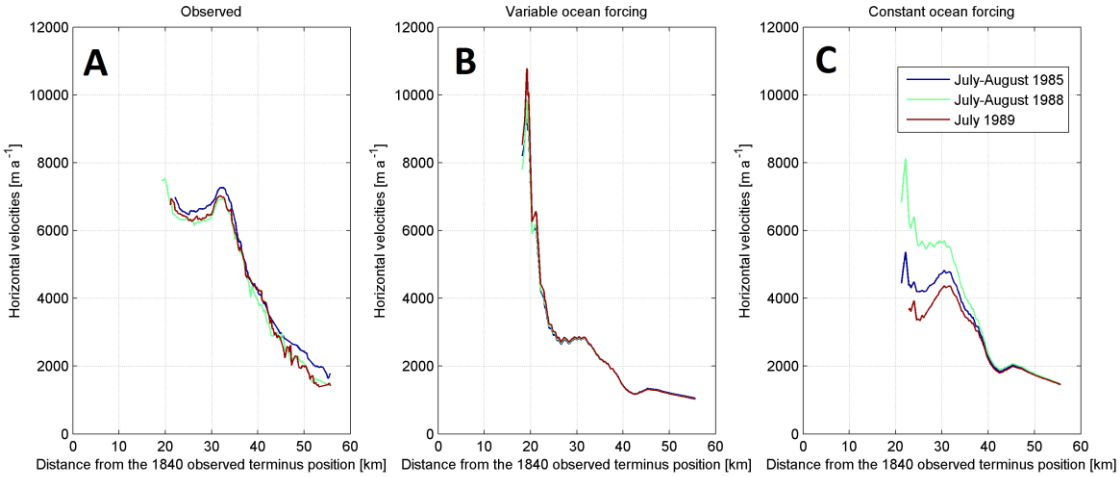

Figure 23: (A) Observed horizontal velocities at JI along the dotted flowline shown in Fig 1D for July-August 1985, July-August 1988, and July 1989. (B) Modelled yearly mean horizontal velocities in a simulation with variable surface ocean temperature for 1985, 1988 and 1989. (C) Modelled yearly mean horizontal velocities in a simulation with constant surface ocean temperature for 1985, 1988 and 1989.

The acceleration occurs as the terminus retreats from a basal high through an overdeepening. During this period, modelling results suggest a retreat of the southern tributary by ~8-10 km, which correlates with existing observations (Thomas, 2004). A retreat of a similar magnitude is modelled for the grounding line position. In my model, a floating ice tongue starts to develop in 1998, however this ice tongue is rapidly calved and generally the modelled terminus retreat tends to follow closely the modelled grounding line retreat, i.e. only a small floating ice tongue is modelled. During the 1998-2003 flow acceleration, the simulation produces speeds high as 16 km a^{-1} (~ 220 % increase relative to 1997). The modelled velocities decreased to 12 km a^{-1} (~ 140 % increase relative to 1997) in the subsequent years and remained at the same magnitude with the sparse observations from that time (e.g. Joughin et al., 2012). Figure 24 shows observed and modelled horizontal velocities for 2000-2001, 2005-2006, 2006-2007 and 2008-2009. Overall, a good agreement is obtained with RMSE values that range between 90.8 m a^{-1} to 802.2 m a^{-1} (Table A7). Similarly, Fig. 25 shows observed and modelled ice thickness changes at points S1, S3 and S6 (see Fig. 1C) with RMSE values that range over the period 2003-2012 between 3 m and 33 m (Table A8). Further, and similarly with Vieli et al. (2001), I am not able to simulate the observed retreat of the southern tributary after 2010. Observed front positions

(Joughin et al., 2014) suggest that by the summer 2010 JI was already retreating over the sill and on the over deepening indicated by the red star in Fig. 29. This recent behaviour of JI is, in fact, the topic of Study 3.

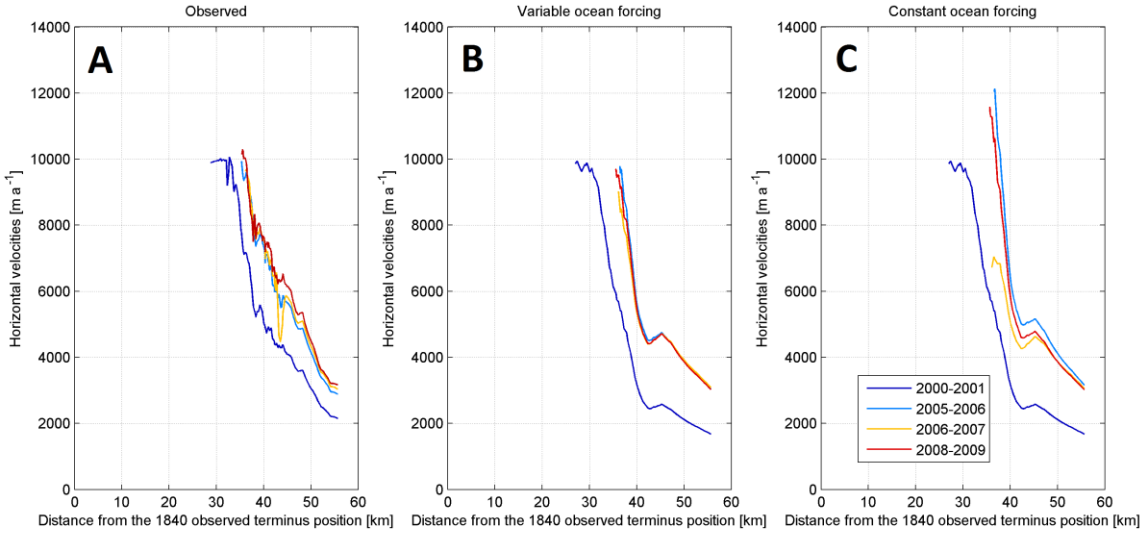

Figure 24: (A) Observed horizontal velocities at JI along the dotted flowline shown in Fig 1D for 2000-2001, 2005-2006, 2006-2007 and 2008-2009. (B) Modelled yearly mean horizontal velocities at JI along the dotted flowline shown in Fig 1D in a simulation with variable surface ocean temperature and (C) a simulation with constant surface ocean temperature for 2000-2001, 2005-2006, 2006-2007 and 2008-2009.

5.1.4 Modelled ice mass change

The mass loss begins in my model in 1870 and correlates with the sustain terminus retreat and thinning discussed in Sect. 5.1.1. Following the initial acceleration of JI which starts in 1920, the modelled mass change accelerates thereafter. Mass change estimates of 437.6 Gt or 10.6 Gt a^{-1} are modelled in the simulation with variable ocean forcing between 1920-1960. Although, the modelled terminus positions remain relatively stable (Fig. 21 and 22A), after late 1940's, JI continues to lose mass until the 70's when the climate begins to cool (Figs. 2, 5 and 26). Overall, the period 1970-1997 is characterized in my model by a slowdown in mass change. Observational data (e.g. atmospheric and oceanic temperature in the JI region; Sect 2) suggest that during this period the observed mass change slows as a consequence of colder climate conditions (see Fig. 5). Similarly, in my simulation the slowdown in mass is triggered by a decrease in ocean temperature of 0.5 °C (Fig. 5). After 1997, JI's mass change starts to accelerate again as a consequence of warmer climate conditions (i.e., 0.8 °C increase in ocean temperature; Fig. 5). Consequently, the constant ocean forcing simulation failed to capture the observed variability in mass during the period 1970-2012. In the simulation with variable ocean forcing the mass change for the period 1990-2012 is 253.2 Gt or 11 Gt a^{-1}. Table A9 and Table A10

summarizes mass loss estimates and major terminus collapses at JI for the period 1840-1880, 1880-1920, 1920-1960, 1960-1990, and 1990-2012.

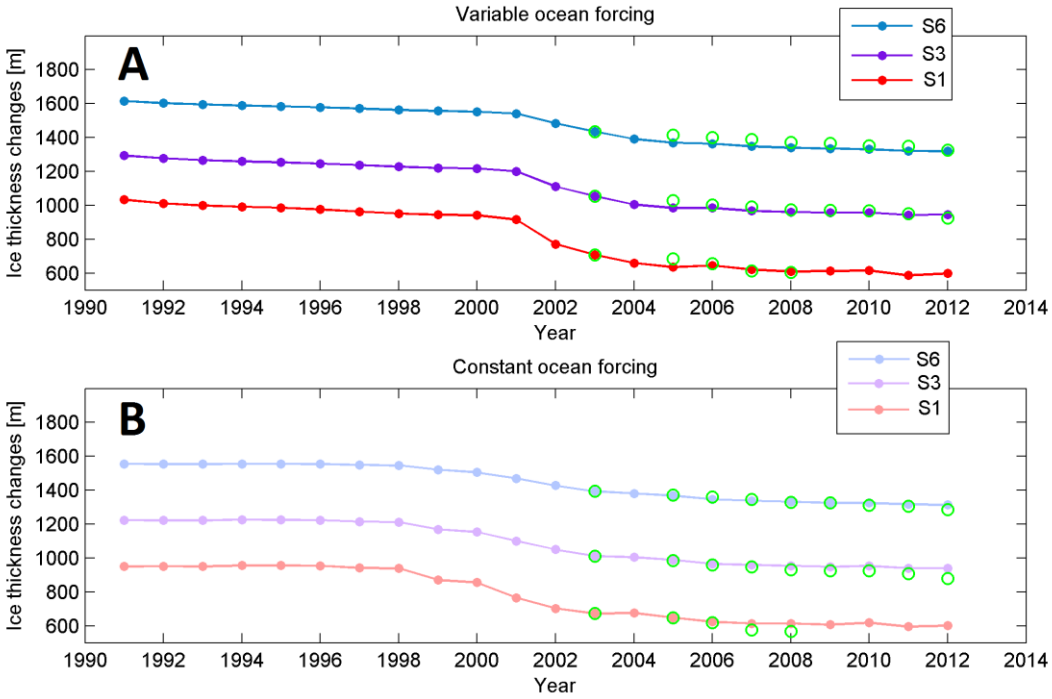

Figure 25: Time series of modelled (filled circles) versus observed (empty circles with light green edges) ice thickness changes (Krabill, 2014) (for the period 1990–2012 at the locations (S1, S3, and S6) shown in Fig. 1C) in the simulation with variable ocean surface temperature (A) and constant ocean surface temperature (B).

Figure 26 shows observed and modelled mass change for the simulations that include variable and constant ocean forcing. The observed rate of ice volume changes are estimated from airborne and satellite altimetry over the period 1997-2012 and are converted to rates of mass change as detailed in Sect. 2.4. For the period 1997-2012, I found a good agreement between modelled and observed mass change (see Fig. 26). The modelled cumulative mass loss for the period 1840-2012 is 1214.5 Gt (~3.4 mm SLE), of which 77 % (~937.3 Gt) is dynamic in origin while the remaining 23 % (~ 271 Gt) is attributed to a decrease in SMB (Fig. 26). For the period 1990-2014 dynamically driven discharge has been shown to control Jakobshavn's mass loss (Nick et al., 2013). Similarly, here I found that dynamical driven discharge controlled JI mass loss since the end of the LIA.

5.2 Discussion

The present study is the first that aimed and succeeded to capture reasonably well JI's behaviour in the last century. This longer-term reconstruction of glacier behaviour back to the end of the Little Ice Age provides new insight in understanding JI's behaviour over more than 100 years and has the capability to ensure long term

calibrated projections. During the period 1900-2012, I calibrated the model to match the observed terminus positions available at JI (~15) as well as observed mass change estimates for the period 1997-2012. Overall, I obtained a good agreement between observed and modelled time series of horizontal velocities and ice thickness changes (e.g. Fig. 24). In agreement with Csatho et al. (2008), I identified three major periods of rapid thinning: 1902–1913, 1930–1959 and 1999–present (Figs. 21, 22 and 26).

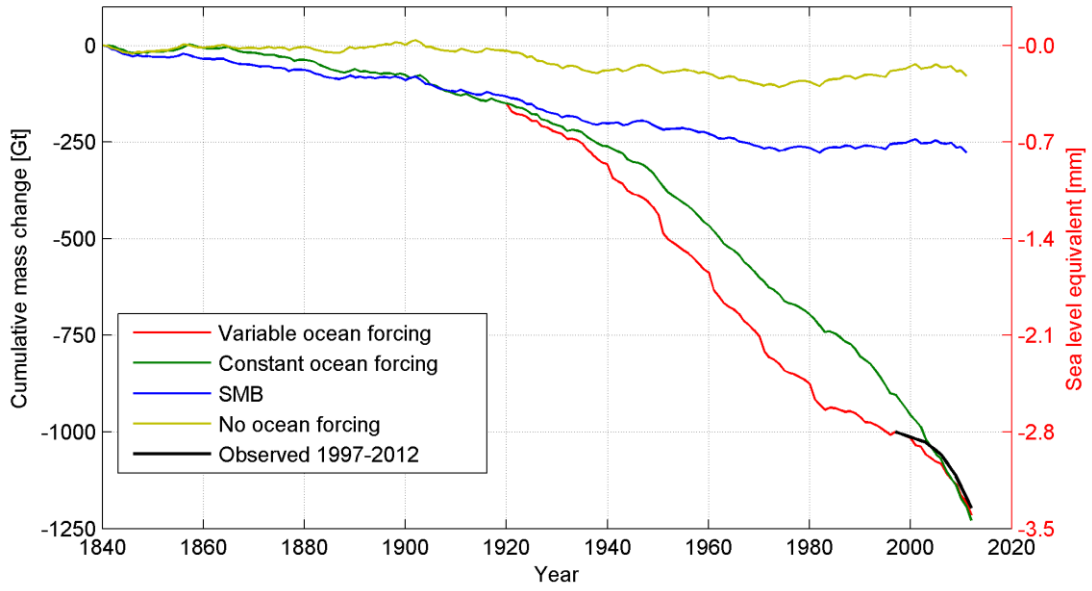

Figure 26: Modelled and observed cumulative mass change for Jakobshavn Isbræ. The blue curve represents the mass change due to SMB (Box et al., 2013) after the 1960–1990 baseline is removed (~271 Gt). The "golden olive" curve represents the total modelled mass change in a simulation with variable atmospheric forcing and no ocean forcing. The green curve represents the total modelled mass change including both SMB and ice dynamic changes modelled in the simulation with constant ocean temperature (1228.3 Gt). The red curve represents the total modelled mass change including both SMB and ice dynamic changes in the simulation with variable ocean temperature (1214.5 Gt). The black curve represents the total observed mass change including both SMB and ice dynamic changes. The modelled mass change for the period 1997–2012 in a simulation with variable ocean forcing is ~209 Gt and ~307 Gt in a simulation with constant ocean forcing. The observed mass change is ~ 200 Gt (Krabill, 2014).

The first modelled acceleration of JI is in 1930 when the grounding line retreated over a reversed bed slope. In my simulations, this initial acceleration of JI is responsible for large surface lowering, and may explain the surface lowering observed by Weidick (1969) and Csatho et al. (2008) during this period. The 1930

acceleration in terminus retreat and flow speed is captured even in a simulation with constant ocean forcing (with one year delay), suggesting that the acceleration is probably not triggered by an increase in ocean temperature (e.g. warm ocean waters entering the Ilulissat fjord that could destabilize JI). This first modelled retreat and flow acceleration of JI illustrates that the dynamic response to a loss of buttressing is transient and it is largely topographically controlled.

Further, according to observations, JI started to float sometime around 1946 and by 1990 the glacier is characterized by a large floating tongue (> 10 km; e.g. Motyka et al., 2011) that I am not able to simulate during the forward simulations. Although, in my model (Figs. 21 and 22A), the glacier develops larger floating tongues in ~1870 (~4-6 km), in 1920 (~4 km) and 1980 (~4 km), they are rapidly calved. Generally, the tendency in my simulations is for the modelled terminus retreat to follow the modelled grounding line retreat, i.e. each year only a small floating ice tongue (e.g. <2 km) is modelled (Fig. 22A). The mismatch between the observed and the modelled floating ice tongue may represent an incomplete modelling of the physics at the terminus (e.g. I do not take into account seasonal fluctuations in ocean surface temperature) or other various limitations (e.g. bed topography model constraints). Alternatively, it may also represent a limitation of the melting parametrization used that for my choice of parameters (I remind here Fmelt) could just not favour the development of very large floating ice tongues, limitations of the calving mechanisms used, or a combination of both. Following the melting parametrization, the highest melt rates are modelled in the proximity of the glacier grounding lines and decrease with elevation such that the lowest melt rates are closer to the central to frontal area of the modelled ice shelf. In my model, the eigencalving parametrization cannot resolve individual calving events, and, thus, the introduction of the basic calving mechanism was necessary in order to accurately match observed front positions. The basic calving mechanism, which drives most of the calving modelled in my simulations (over 90 %; see Sect. 6.3), removes any ice at the calving front not calved by the eigen-calving parametrization thinner than 400 m in the forward runs. The physical concept behind this basic calving mechanism is that generally, ice shelf calving fronts are thicker than 150–300 m (The PISM Authors, 2014). Therefore, large melt rates at the grounding line (see Sect. 6.3) as produced by the ice shelf melting parametrization can accelerate the grounding line retreat and increase calving through the basic calving mechanism. Remember, that I calibrated the model such that it matches observed terminus positions, and so my choice for the basic calving mechanism thickness threshold (e.g. 400 m) could directly affect my choice of the melting parameter, Fmelt.

Finally, the modelled cumulative mass loss for the period 1840-2012 is ~1214.5 Gt, of which 77 % is dynamic in origin and 23 % is attributed to a decrease in SMB (Fig. 26). Therefore, in the last century, and similarly with the period 1990-2014, JI's mass change was predominately dynamically controlled. Dynamic losses are caused by

outlet glacier terminus retreat and are closely related to the bed geometry. They usually occur after the terminus retreated from a basal high through an overdeepening (Nick et al., 2013). In my simulations, and similarly with Nick et al. (2013), these episodes of rapid retreat occur at different time intervals but generally at the same location (see the location for the 1930 and 2003 accelerations in the simulation with variable ocean forcing vs. the simulation with constant ocean forcing; Fig. 21). Although, the constant ocean forcing simulation succeeds to reasonably simulate the overall observed terminus retreat and mass loss magnitude, my simulations show that is not able to capture the observed JI variability in mass change, especially over the last 30 years. Furthermore, in a simulation with variable atmospheric forcing and no ocean forcing, the terminus remains relatively stable in the proximity of the 1880 observed terminus position. Therefore, the ocean influence in JI's behaviour over the last century is significant and most of JI's retreat during 1840–2012 is driven by the ocean parametrization used and the glacier's subsequent response, which is largely governed by bed geometry (Fig. 26).

Further, and similarly with Vieli et al. (2001), I am not able to simulate the observed retreat of the southern tributary after 2010. This relatively recent behaviour of JI (i.e., 1990-2014) as well as the seasonal driven terminus advance and/or retreat and its correlation with speed fluctuations and glacier dynamics are further investigated in Study 3.

CHAPTER 6

Study 3: Jakobshavn Isbræ numerical simulations (1990-2014)

The goal of this study is to model the recent behaviour of JI (i.e., 1990-2014). Relative to Study 2, here, I wish to focus more on the yearly to seasonal driven terminus advance and/or retreat and speed fluctuations of JI during the period 1990-2014. The period 1990-2014 is abundant in observations and ensures better constrains for the regional model. As a novelty, here I validated the model for the period 2006-2014 using measurements of GPS derived uplift. I forced the model with monthly atmospheric forcing (i.e., air temperature and SMB from RACMO2; Fig. 2) and I used a constant surface ocean water temperature (T_o) of -1.7 °C, which here represented the mean surface ocean temperature in the grid cells adjacent to the JI terminus (Fig. 5). In this regional model, all boundaries (calving fronts, grounding lines, upper, and lower surfaces) were free to evolve in time both during the regional equilibrium and the forward simulations. Along the ice shelf calving front, I superimposed a physically based calving (eigen-calving) parametrization (Winkelmann et al., 2011; Levermann et al., 2012) and a basic calving mechanism (Albrecht et al., 2011) that allowed for glacier terminus advance and retreat.

I performed (on a 2 km grid) a total number of fifty simulations with different sets of parameters (excluding preparatory and additional experiments on the 1 km). During these simulations I altered the parameters obtained in Study 2 controlling the ice dynamics (e.g. the flow enhancement factor, the exponent of the pseudo-plastic basal resistance model, the till effective fraction overburden, etc.) but also parameters related with ice shelf melt, ocean temperature, and calving (i.e., the ice thickness threshold in the basic calving mechanism). These parameters are modified only during the regional JI runs such that the model reproduced the frontal positions and the ice mass change observations at JI during the period 1990-2014 (Fig. 27) and 1997-2014 (Fig. 31), respectively. From these results, I present here the simulation that best captures the full observed evolution of JI during the period 1990–2014 (Fig. 33). I further performed a model sensitivity analysis to parameters controlling ice dynamics, basal processes, ice shelf melt, atmospheric conditions and the ocean parametrization. The values of the ice sheet model parameters used (see Sect. 3 for the underlying equations) are included in Table A11 and Table A12.

In general, the study shows significant progress in modelling the temporal variability of the flow at JI. The study is associated with Paper ii (see Sect. 1.2).

6.1 Observations vs. modelling results

I investigate the processes driving the dynamic evolution of JI and its variation in velocity between 1990 and 2014 with a focus on the first post-1990 speedup of JI (1998) and the 2003 breakup of the ice tongue. I present modelled vs. observed behaviour of annual scale variations in velocities, terminus and grounding line positions. The overall results from the simulations suggest a gradual increase in velocities that agree well with observations (Joughin et al., 2014) (Fig. 28). Three distinct stages of acceleration are identified in Fig. 28 and discussed in detail below.

6.1.1 1990–1997

The first speedup produced by the simulation is caused by a retreat of the front position by approximately 2 to 4 km between 1990 and 1991. There is no observational evidence to confirm that this retreat actually occurred. The simulated retreat is probably a modelling artefact as the geometry obtained during the regional equilibrium simulation is forced with monthly atmospheric forcing and new oceanic conditions. This simulated acceleration (Figs. 28 and 30) is caused in my model by a reduction in buttressing due to a reduction in lateral resistance (Van der Veen et al., 2011), which is generated by the gradual retreat of the front and which triggers a dynamic response in the upstream region of JI.

Starting in 1992, the modelled and observed terminus positions agree. Apart from the acceleration in 1991–1992, no significant seasonal fluctuations in flow rate are found in my simulations for this period, a result that is consistent with observations (Echelmeyer et al., 1994). From 1993 a stronger sub-annual velocity signal begins to

emerge in my simulation that continues and intensifies in magnitude during 1994 and 1995.

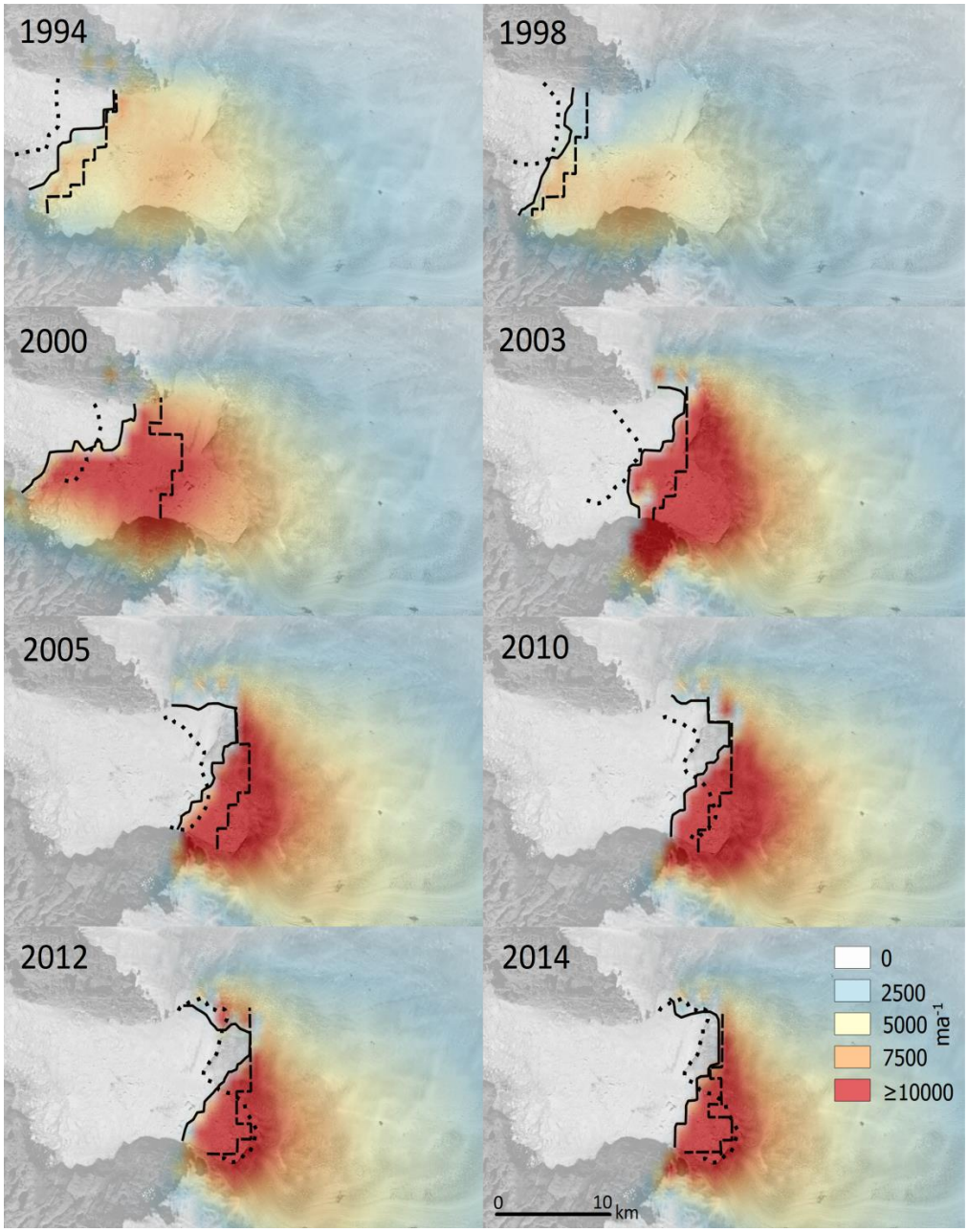

Figure 27: Modelled velocities at Jakobshavn Isbræ for December are shown for eight different years. The black line represents the modelled front positions, the black dotted line denotes the observed front position and the thick black dashed line represents the modelled grounding line position. The velocities are superimposed over a Landsat 8 image acquired in August 2014.

Modelled mean-annual velocities for 1992 and 1995 are consistent with observed velocities for the same period (Joughin et al., 2008; Vieli et al., 2011). In 1996 and

1997, the frontal extent and the grounding line position remain relatively stable (Figs. 27, 29 and 30), and no significant seasonal fluctuation in ice flow rate is observed in the simulation. These model results agree well with observations, which indicate that the glacier speed was relatively constant during this period (Luckman and Murray, 2005).

6.1.2 1998–2002

According to observations (Joughin et al., 2004; Luckman and Murray, 2005; Motyka et al., 2011; Bevan et al., 2012), the initial acceleration of JI occurred in May-August 1998, which coincides with my modelled results. In my simulation, the 1998 acceleration is generated by a retreat of the ice tongue's terminus in 1997-1998, which may be responsible for reducing buttressing (Fig. 30). Thinning, both near the terminus and inland (up to 10 km away from the 1990 front position), starts in my model in the summer of 1995 and continues to accelerate after 1998 (Figs. 28, 29 and 30). The modelled behaviour agrees well with the observed behaviour (Krabill et al., 2004).

Although thinning appears to have increased in my model during three continuous years, it produced only minor additional speedup during the period prior to 1998 (Figs. 27, 29 and 30). In my simulation, JI's speed increased in the summer of 1998 by ~80 % relative to the summer of 1992 (Fig. 28), at which time the grounding line position starts to retreat thereafter (Figs. 27, 29 and 30). Observations (Luckman and Murray, 2005) do not show this level of speedup, and there are no observations of the grounding line position at this time with which to assess my model performance. Overall, modelling results suggest an advance of the terminus between 1999 and 2000 and a retreat of the southern tributary between 2000 and 2002 by ~4 km, which correlates with existing observations (Thomas, 2004). In my simulation, this retreat of the terminus triggers a decrease of resistive stresses at the terminus (Fig. 30). Concurrent with the 1998-2002 terminus retreat, the grounding line retreats in my model by ~6 km (Figs. 27, 29, and 30).

6.1.3 2003–2014

In the late summer of 2003, the simulated flow velocity increases (Fig. 28). This acceleration of JI is driven in my simulations by the final breakup of the ice tongue (see Figs. 27 and 29). The period 2002-2003 is characterized in my model by substantial retreat of the front (~4-6 km) and the grounding line (~4 km), which starts in June 2002 and continues throughout 2003. The simulated retreat that occurred in 2003 and the loss of large parts of the floating tongue (Figs. 27 and 29) caused a major decrease in resistive stresses near the terminus (Fig. 30).

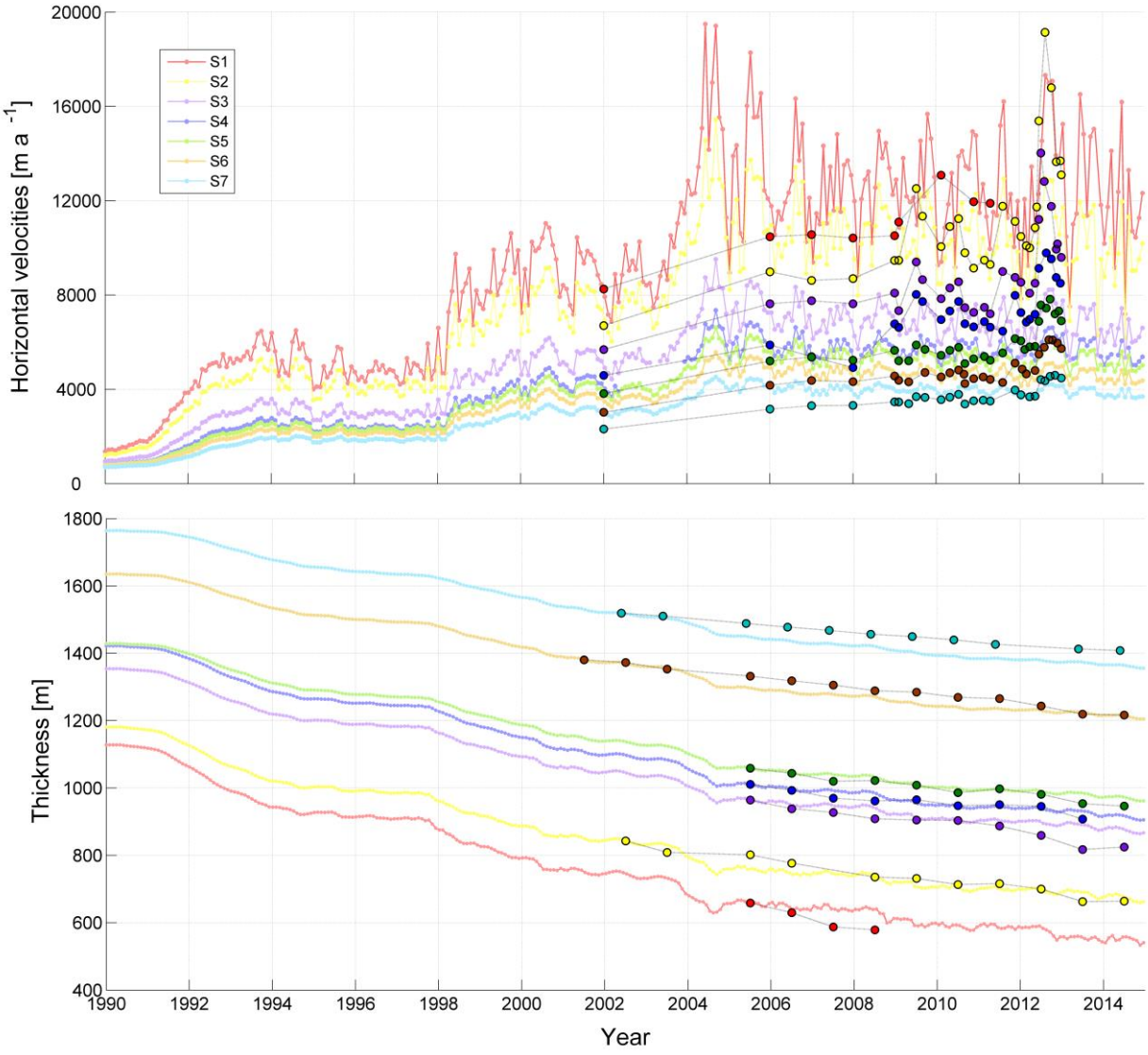

Figure 28: Time series of modelled (filled circles) versus observed (filled circles with black edges) velocities (Joughin et al., 2010) (top figure) and ice thickness changes (Krabill, 2014) (bottom figure) for the period 1990-2014 at locations (S1 to S7) shown in Fig. 1C. The same colour scheme is used for the modelled and the observed data. The observed velocities prior to 2009 are mean winter velocities and are largely consistent with my modelled winter estimates for the same period. The observed thickness has been adjusted to match the model thickness at the first available observation (i.e., by summing the modelled ice thickness corresponding to the first available observation with the observed thickness changes).

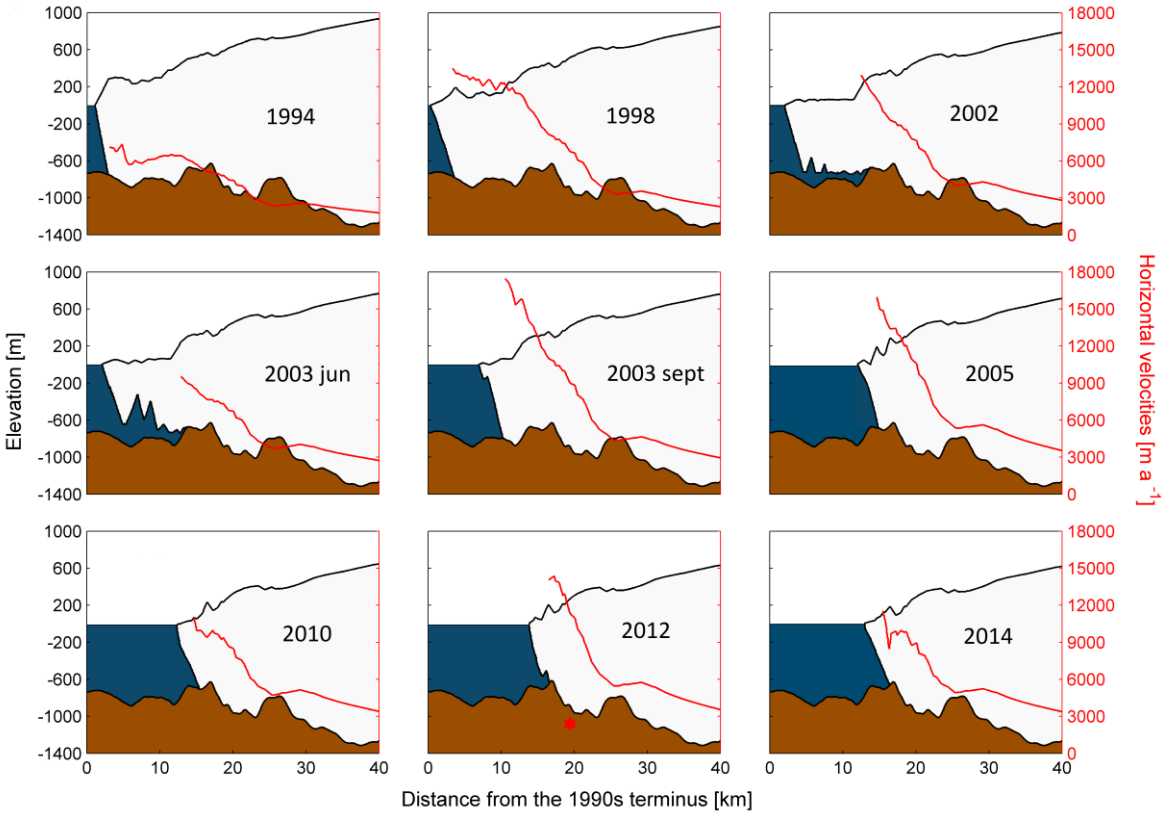

Figure 29: Modelled evolution of surface elevation (floating ice tongues thinner than 50 m are not shown) and horizontal velocities of Jakobshavn Isbræ for December along the flow-line shown in Fig. 1C. Note the acceleration in speed between 1994-1998 and between June 2003 and September 2003 corresponding to the final breakup of the floating tongue. The red star denotes the observed 2012 terminus position.

By 2004, the glacier had thinned significantly (Figs. 28 and 29) both near the front and further inland in response to a change in the near-terminus stress field (Fig. 30). During the final breakup of the ice tongue, the simulation produces speeds high as 20 km a^{-1} (~120 % increase relative to 1998). The modelled velocities decreased to 16 km a^{-1} (~80 % increase relative to 1998) in the subsequent months and remained substantially higher than the sparse observations from that time (e.g. Joughin et al., 2012).

The high velocities modelled at JI after the loss of its floating tongue are further sustained in my simulation by the thinning that occurred after 2003 (Fig. 28), which continues to steepen the slopes near the terminus (Fig. 29), and is accompanied by a seasonal driven (sub-annual scale) retreat and advance of the front. This simulated thinning is combined in the following years with a reduction in surface mass balance due to increased melting and runoff (van den Broeke et al., 2009; Enderlin et al., 2014, Khan et al., 2014). The period 2004-2014 is characterized in my simulation by relatively uniform velocity peaks with strong sub-annual variations (Fig. 28). During

this period, only a small floating ice tongue is modelled and the terminus remained relatively stable, with no episodes of significant retreat.

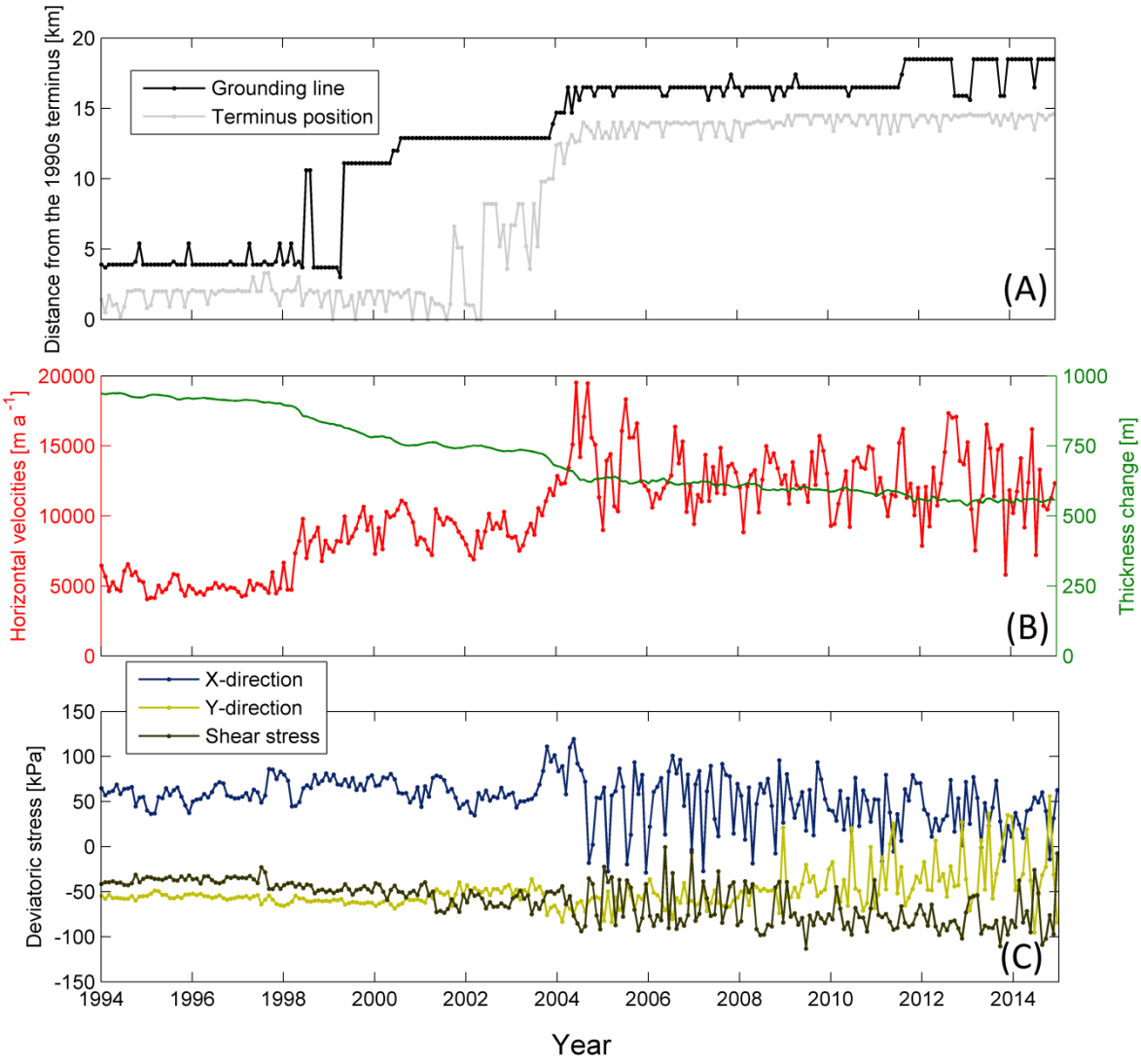

Figure 30: (A) Modelled grounding line and terminus position (floating ice tongues thinner than 50 m are not shown). (B) Modelled horizontal velocities and ice thickness changes at the point location S1 shown in Fig. 1C. (C) Modelled 2-D deviatoric stresses (in the X direction, the Y direction, and the shear stress) at the point location S1 shown in Fig. 1C.

In agreement with previous studies (e.g. Joughin et al. 2012), my results suggest that the overall variability in the modelled horizontal velocities is a response to variations in terminus position (Fig. 30). In my simulation, the retreat of the front reduced the buttressing at the terminus and generated a dynamic response in the upstream region of JI which finally led to flow acceleration. In contrast, when the front advanced the modelled flow slowed as the resistive stresses at the terminus were reinforced. This

buttressing effect tends to govern JI's behaviour in my model. Regarding the overall terminus retreat, my simulations suggest that it is mostly driven by the sub-shelf melting parametrization applied (Fig. 34). Although, the heat flux supplied to the shelf evolves in time based on the modelled terminus geometry, the input ocean temperature is kept constant throughout the simulations. This constant ocean forcing at the terminus leads, in my simulation, to gradual thinning of JI and favours its retreat without any shift (e.g. increase) in ocean temperature. In terms of seasonality, the only seasonal signal in the model is introduced by the monthly atmospheric forcing applied (Sect. 2.1). However, the modelled sub-annual variability in terms of terminus retreat and velocities does not always follow the seasonal signal (Fig. 28). I investigate this higher than seasonal variability in Sect. 6.3.

6.1.4 Ice mass change

Figure 31 shows observed and modelled mass change for the period 1997 to 2014. The observed rate of ice volume changes is estimated from airborne and satellite altimetry over the same period and is converted to rates of mass change as detailed in Sect. 2.4. Overall I found good agreement between modelled and observed mass change (Fig. 31), and my results are in agreement with other similar studies (Howat et al., 2011; Nick et al., 2013). Dynamically driven discharge is known to control Jakobshavn's mass loss between 2000 and 2010 (Nick et al., 2013). The modelled cumulative mass loss is 269 Gt, of which 93 % (~251 Gt) is dynamic in origin while the remaining 7 % (~18 Gt) is attributed to a decrease in SMB (Fig. 31). Further, the present-day unloading of ice causes the Earth to respond elastically. Thus, I can use modelled mass changes to predict elastic uplift. I compared modelled changes of the Earth's elastic response to changes in ice mass to uplift observed at four GPS sites (Fig. 32). Both model predictions and observations consistently suggest large uplift rates near the JI front (20 mm a^1 for station KAGA) and somewhat minor uplift rates (~5 mm a^{-1}) at distances of >100 km from the ice margin.

Although the terminus has ceased to retreat in my simulations after 2009 (Figs. 29 and 30), the modelled mass loss, and more importantly the dynamic mass loss, continues to accelerate (Fig. 31). My results show (Fig. 30) that during this period, the mass change is mostly driven by the sub-annual terminus retreat and advance, which continues to generate dynamic changes at JI through seasonal (sub-annual scale) reductions in resistive stresses (Fig. 30).

6.2 Ice sheet model sensitivity analysis

This section focuses on the ice sheet model sensitivity to parameters controlling ice dynamics, basal processes, ice shelf melt, atmospheric conditions and the ocean parametrization. The values of the ice sheet model parameters used (see Sect. 3 for the underlying equations) are included in Table A11 and Table A12. The parameterization that best captures the full evolution of JI during the period 1990–

2014 is further referred as the reference run (red line in Fig. 33). The parameter values used during this simulation are included in Table A12 (3rd column).

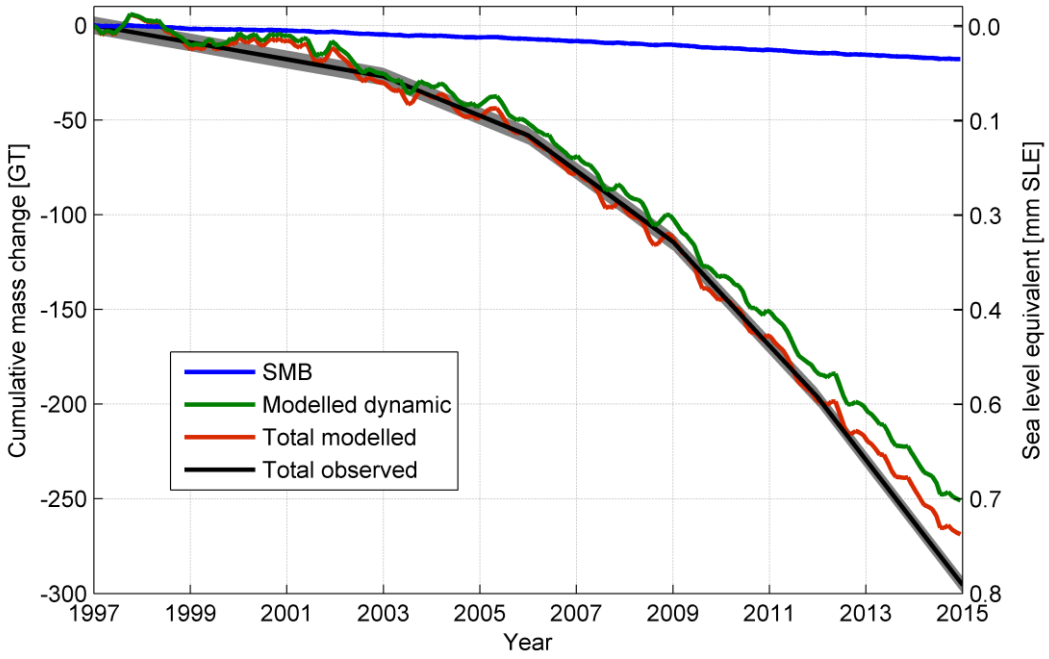

Figure 31: Modelled and observed cumulative mass change for Jakobshavn Isbræ. The blue curve represents the mass change due to SMB (Noël et al., 2015) after the 1960-1990 baseline is removed. The green curve represents the modelled ice dynamics mass change (i.e., modelled mass change minus SMB change). The red curve represents the total modelled mass change including both SMB and ice dynamic changes. The black curve with grey error limits represents the total observed mass change including both SMB and ice dynamic changes. The modelled mass change for the period 1997-2014 is ~269 Gt and the observed mass change is ~296 Gt.

6.2.1 Sensitivity to parameters controlling ice dynamics, basal processes, and ice shelf melt

The evolution in time of the cumulative mass change for different values of the flow enhancement factor is shown in Fig. 33 (top-left). The figure shows that for smaller values of the E_{SIA} (i.e., smaller than the reference run) the flow slows overall and therefore the modelled mass loss decreases as discharge decreases. The opposite behaviour, i.e. flows accelerates and mass loss increases is seen for larger values of the E_{SIA}. A small delay in the terminus retreat (~1 year relative to the 2003 retreat from the reference run) is observed for E_{SIA}=1. The timing of the retreat is therefore sensitive to changes in E_{SIA}, while magnitude wise, it seems

that the peaks and the flow accelerations modelled in the reference run (see Fig. 33) are mostly controlled by the bed geometry and remain unaltered by changes in E_{SIA}.

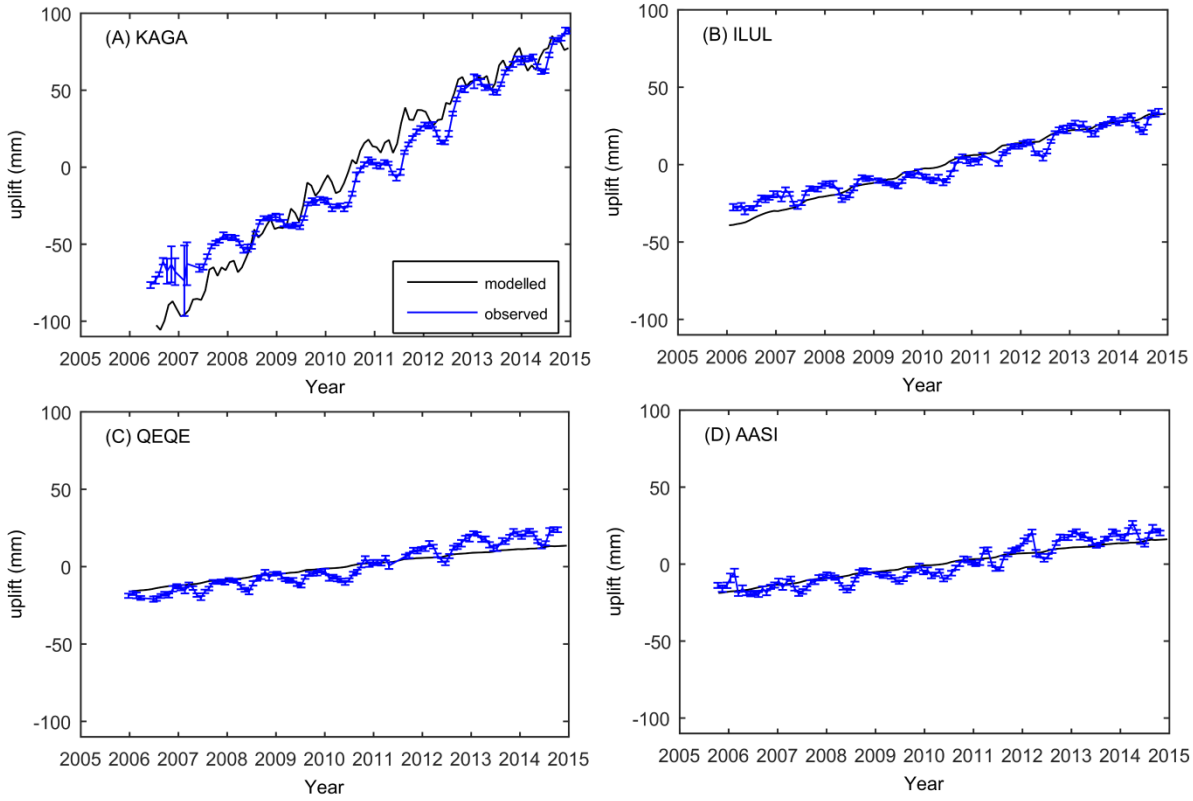

Figure 32: Observed versus modelled uplift in mm for the stations KAGA (A), ILUL (B), QEQE (C) and AASI (D). The positions of the four GPS stations are presented in Fig. 1A.

In my model, the ice deforms as a result of basal shear stress and therefore, for values of q smaller than the reference run (see Fig. 33. top-right), the basal shear stress decreases making the mass loss and the terminus retreat to slow (e.g. +4 years relative to the 2003 retreat observed in the reference run). For values of q larger than the one used in the reference run, the basal shear stress increases making the mass loss and the terminus retreat accelerate (e.g. -4 years relative to the 2003 retreat observed in the reference run).

As seen in Fig. 33 (bottom-left), the model shows a high sensitivity relative to the value of the till effective fraction overburden used. The figure shows that for smaller values of δ (i.e., smaller than the reference run), the glacier grows in size and no retreat of the front is observed, while for larger values of δ, the terminus retreat accelerates holding by 1998 the 2003 position observed in the reference run (i.e., -4 years relative to the 2003 reference run retreat).

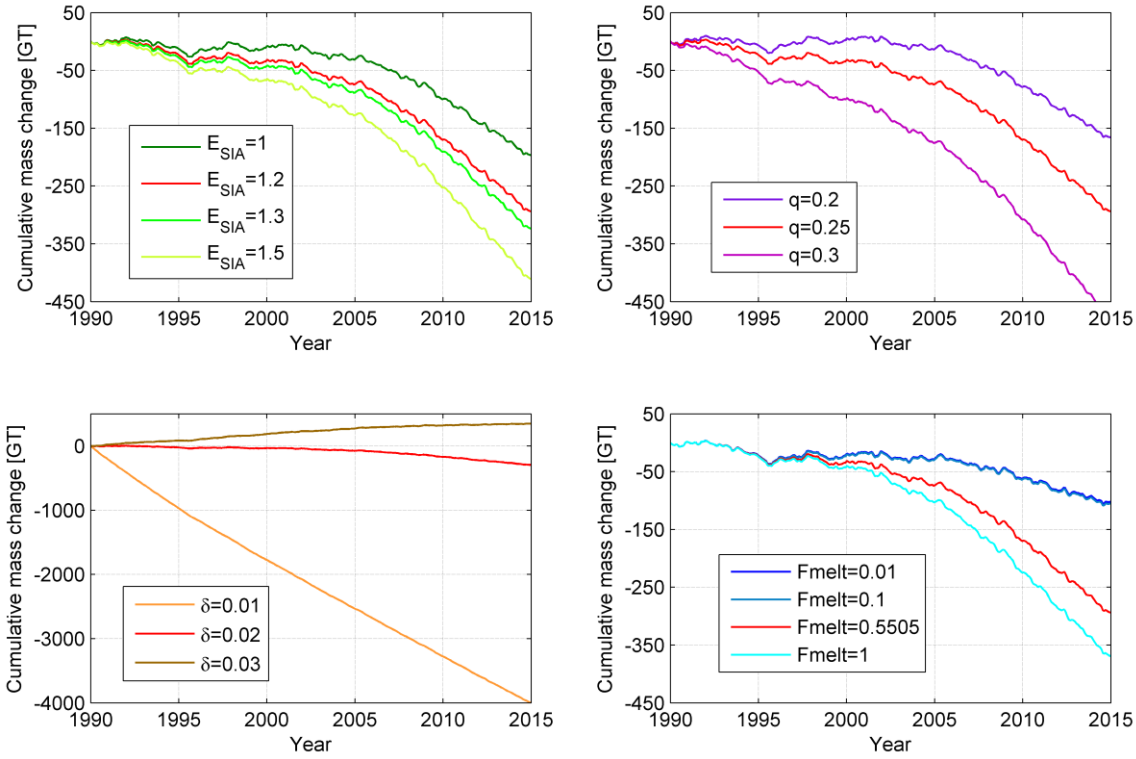

Figure 33: Sensitivity experiments for parameters controlling ice dynamics, basal processes and ice shelf melt. In the right bottom plot, the curves for Fmelt=0.01 and Fmelt=0.1 are superimposed.

F_{melt} is a model parameter used in the heat flux equation and included in the parameterization for ice shelf melting (see Eq. 34). F_{melt} plays an important role in the terminus and groundling line retreat and/or advance. As shown in Fig. 33 (bottom-right), smaller values of F_{melt} (i.e., smaller than in the reference run) result in low magnitude melt rates leading to a decrease in mass loss. The opposite behaviour is encountered for larger values of F_{melt} (i.e., larger than the reference run). The magnitude of the melt rates increases and therefore, the terminus and the grounding line retreat accelerate resulting in a mass loss increase.

6.2.2 Atmospheric forcing and ocean parametrization

Figure 34 shows the cumulative mass change at JI during the period 1990–2014 for different forcing combinations. I studied the sensitivity of the model to atmospheric forcing by performing a simulation where I kept the atmospheric forcing constant (mean 1960-1990 temperature and SMB). By comparing this with a simulation that includes full atmospheric variability (monthly temperature and SMB), I see that in terms of terminus retreat and velocities the modelled sub-annual variability does not always correlate with the observed seasonal signal (Fig. 35).

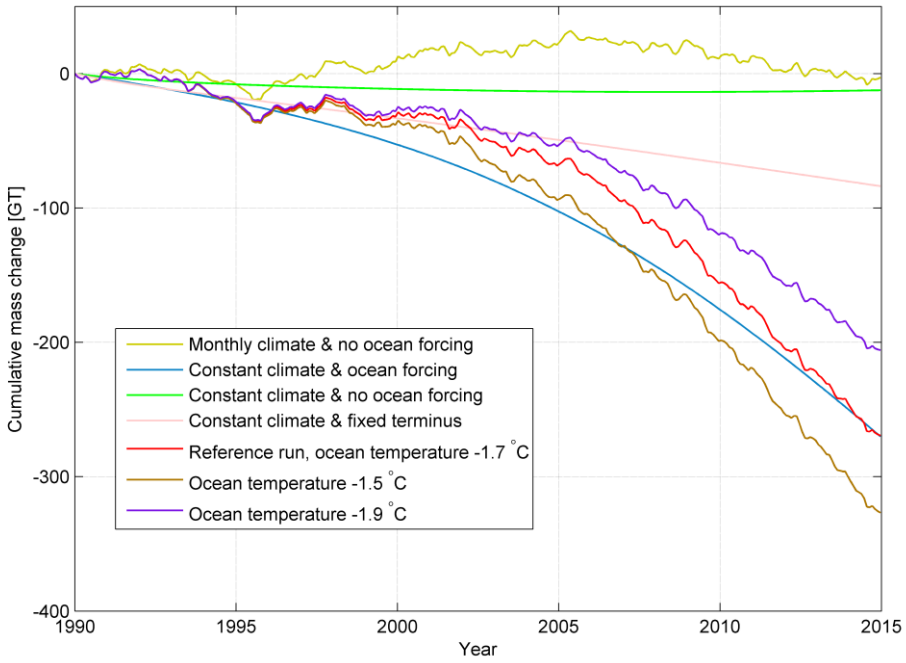

Figure 34: Cumulative mass change at JI during the period 1990–2014 for different forcing combinations. Monthly climate refers to a forcing with 1990-2014 monthly temperature and SMB as taken from RACMO2.3 (Noël et al., 2015). During the so called "constant climate" run (blue line) the monthly atmospheric forcing consists of mean 1960-1990 temperature and SMB (RACMO2.3, Noël et al., 2015). During the "no ocean" runs the parameterization for ice shelf melting is turned off (yellow and green lines). During the fixed terminus run (light pink line) the front is held fixed to the 1990 observed position. The cumulative mass change at JI for different ocean temperatures is shown with brown (-1.5 °C), red (-1.7 °C) and purple (-1.9 °C) lines. The reference run (red line) refers to the simulation that best captures the full evolution of JI between 1990-2014.

In particular, the simulations suggest that to only a relatively small degree some of the variability appears to be influenced by the atmospheric forcing applied (Fig. 35), which also represents the only seasonal input into the model. Compared with a simulation with ocean and monthly atmospheric forcing, in a simulation with constant climate (Figs. 34 (blue line) and 35), the retreat of the terminus relative to the 2003 retreat observed in the reference run is delayed by 1 year. Overall, my results suggest that the atmospheric forcing (see Fig. 34, yellow, blue and red lines) plays a secondary role in JI's retreat (i.e., relative to the oceanic forcing). As shown in Fig. 34, the overall oceanic contribution to JI's retreat is significant and a simulation with no oceanic forcing results in a small growth of the glacier (see yellow line in Fig. 34) rather than a retreat.

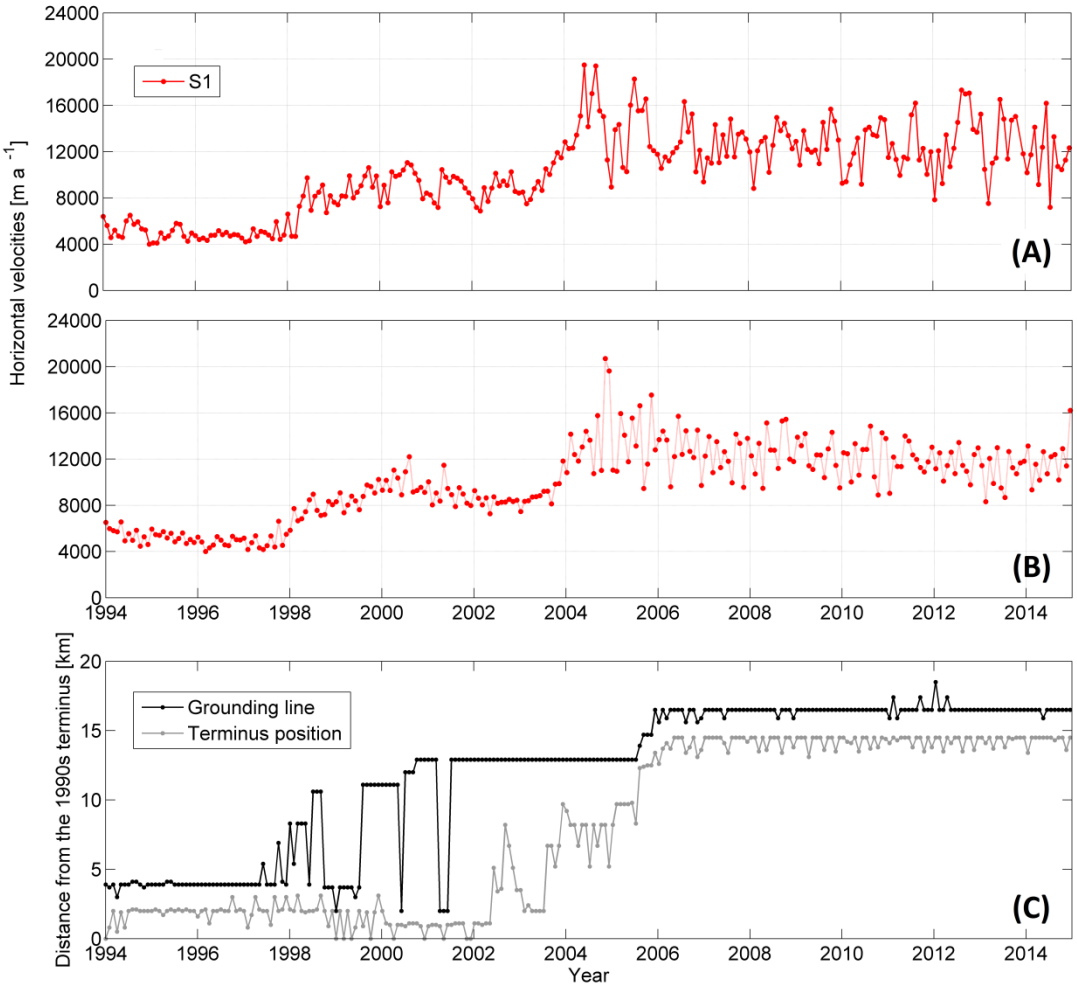

Figure 35: Time series of modelled velocities for the period 1990-2014 at the point location S1 shown in Fig. 1C with monthly climate forcing (i.e., monthly 1990-2014 SMB and temperature) (A) and constant monthly climate forcing (i.e., mean 1960-1990 SMB and temperature) (B). (C) Modelled grounding line and terminus position (ice thickness > 50 m) with constant climatic forcing.

As depicted from Fig. 34 the model is sensitive to changes in ocean temperature. In my model, a decrease in ocean temperature of 0.2 °C is equivalent to a decrease in mass loss of ~70 Gt as the magnitude of the melt rate decreases and the retreat of the terminus slows (e.g. in the simulation with T_o= -1.9 °C (see Fig. 34), the 2003 retreat modelled in the reference run occurs only in 2014). On the other hand, an increase in ocean temperature is equivalent to an increase in mass loss (see Fig. 34) as the retreat of the terminus accelerates.

6.2.3 Grid resolution

Some of the greater than seasonal frequency could be an issue with resolution in the model. I examined this sensitivity by performing additional runs at a higher spatial

resolution. Simulations on a 1 km grid did show some improvement with respect to surface speed sub-annual variability (Fig. 38), suggesting that in my model the stress redistribution might be sensitive to the resolution of the calving event (i.e., 2x2 km or 1x1 km). However, given the short period spanned by these simulations, the stress redistribution does not change the overall modelled results, as seen in Figs. 36 and 37. Although, I acknowledge that some of this variability is due to the grid resolution, part of it may also be related to unmodeled physical processes acting at the terminus.

I suggest that additional contributions to the seasonality, e.g. from ice mélange or seasonal ocean temperature variability, which are not included in my model could potentially influence the advance and retreat of the front at seasonal scales (Fig. 35). Furthermore, simulations performed on a 1 km grid showed similar ice thickness (Fig. 36) and surface speed (i.e., shape of the flow; Fig. 37) trends and patterns.

6.3 Discussion

Representing the processes that act at the marine boundary (i.e., calving and ocean melt) are important for understanding and modelling the retreat/advance of marine terminating glaciers like JI. Determining terminus positions by using the superposition of a physically based calving (eigencalving) parametrization (Winkelmann et al., 2011; Levermann et al., 2012) and a basic calving mechanism (Albrecht et al., 2011) is motivated by the model's ability to maintain realistic calving front positions (Levermann et al., 2012). The eigen calving style cannot resolve individual calving events, and, thus, the introduction of the basic calving mechanism was necessary in order to accurately match observed front positions. Preparatory experiments have shown that overall calving is mostly driven in my model by the basic calving mechanism used, and that the eigen calving parametrization is more important in modelling sub-annual to seasonal fluctuations of the terminus. My simulations suggest that the superposition of these two calving mechanisms performs well for relatively narrow and deep fjords as those characterized by JI. The benefit of using such a combination of calving laws is that it can evolve the terminus position with time and thus calving feedbacks are not ignored. As the terminus retreats, the feedback between calving and retreat generates dynamic changes due to a reduction in lateral shear and resistive stresses (Fig. 30). In a simulation in which the terminus position is kept fixed to the 1990s position, the velocity peaks are uniform (i.e., no acceleration is modelled except for some small seasonal related fluctuations generated by the atmospheric forcing applied), and the mass loss remains relatively small (~70 Gt). Consistent with Vieli et al. (2011), I found that the feedback between calving and retreat is highly important in modelling JI's dynamics. As introduced in Sect. 2, my approach here was to adjust the terminus in the JI region to simulate the 1990s observed front position and surface elevation based on 1985 aerial photographs (Csatho et al., 2008). The glacier terminus in

1990s was floating (Csatho et al., 2008; Motyka et al. 2011). Motyka et al. (2011) calculated the 1985 hydrostatic equilibrium thickness of the south branch floating tongue from smoothed surface DEMs and obtained a height of 600 m near the calving front and 940 m near the grounding zone.

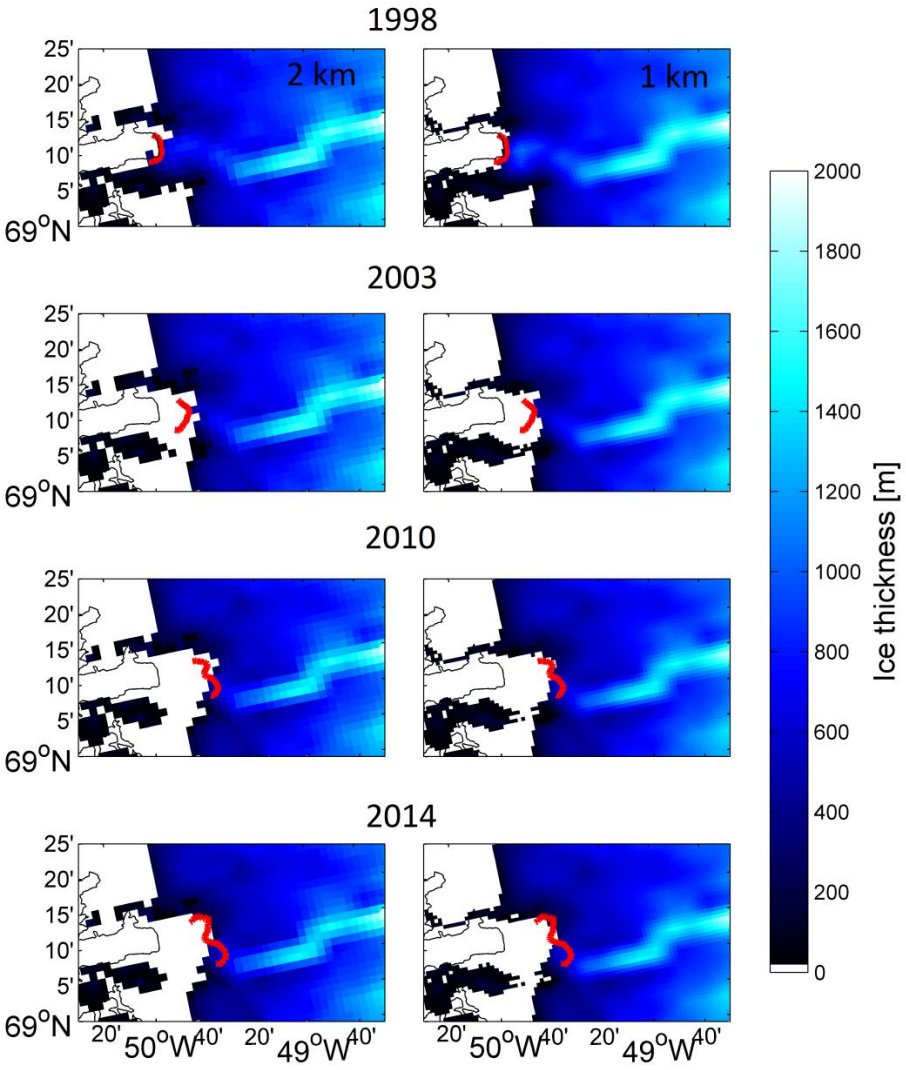

Figure 36: Modelled ice thickness at JI on a 2 km (left) and a 1 km (right) grid. The solid red lines represent the observed positions of the terminus for the different years plotted.

In this study, however, I computed the thickness as the difference between the surface elevation and the bed topography, and allow the glacier to evolve its own terminus geometry during the equilibrium simulation. Preparatory experiments have shown that in my model (disregarding its initial geometry floating/ grounded terminus) JI attains equilibrium with a grounding line position that stabilizes close to the 1990s observed terminus position. According to observations, JI is characterized in 1990 by a large floating tongue (> 10 km; e.g. Motyka et al., 2011) that I am not

able to simulate during the equilibrium runs. In my model (Figs. 29 and 30), the glacier starts to develop a large floating tongue (~10 km) in 1999. Starting in 2000, the floating tongue is comparable in length and thickness with observations and the model is able to simulate, with a high degree of accuracy, its breakup that occurred in late summer 2003 and the subsequent glacier acceleration.

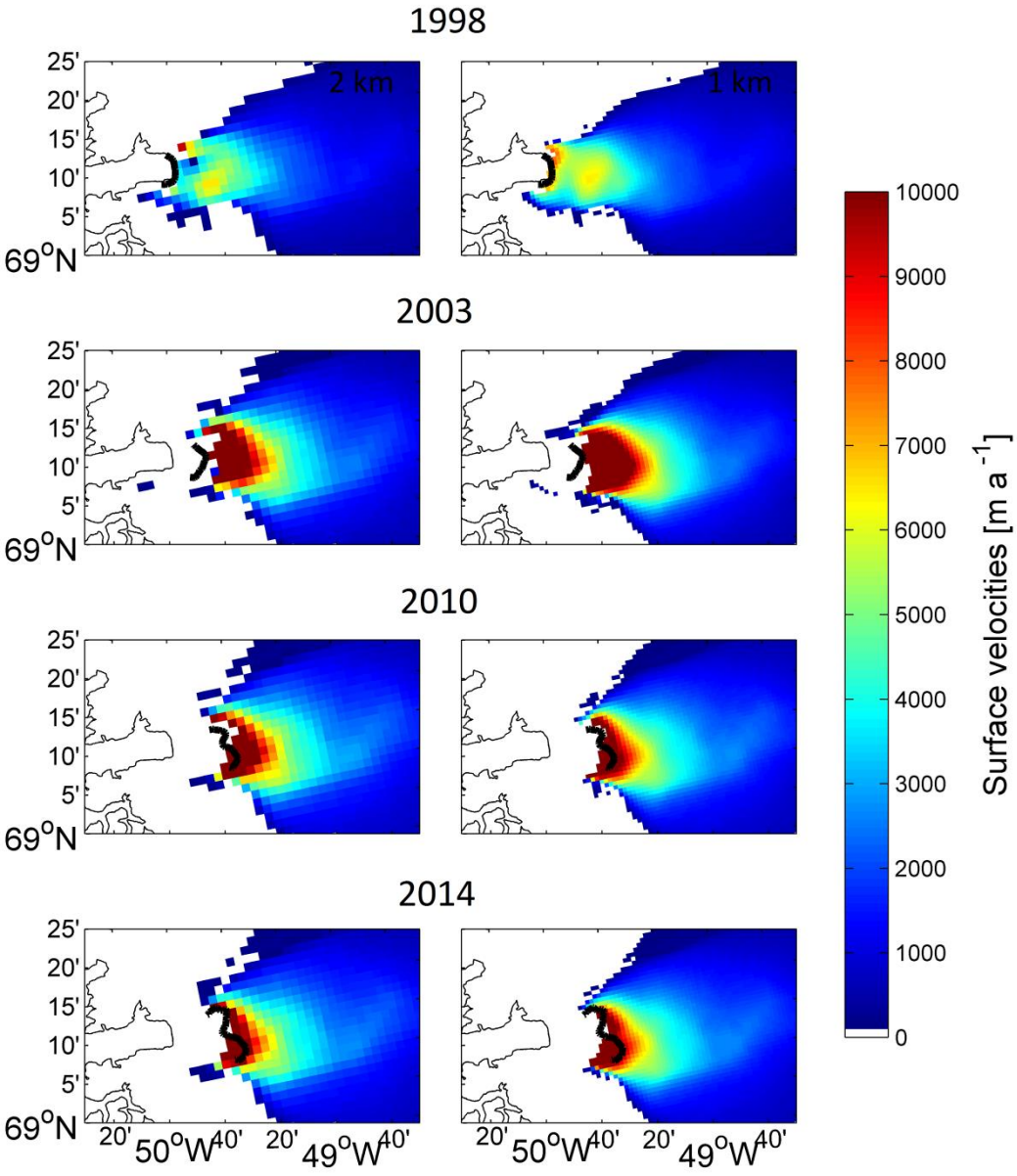

Figure 37: Modelled horizontal surface velocities at JI on a 2 km (left) and a 1 km (right) grid. The solid black lines represent the observed positions of the terminus for the different years plotted.

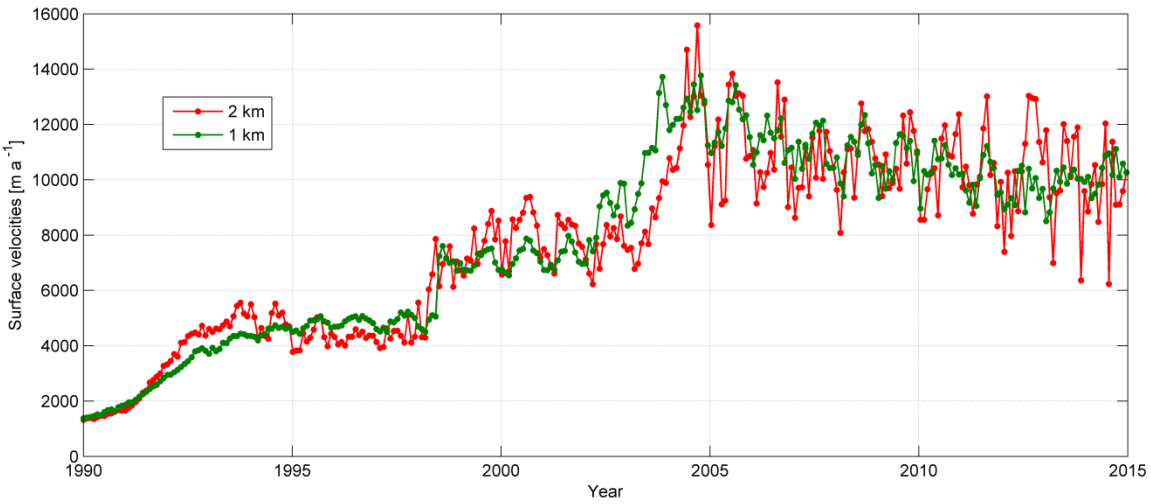

Figure 38: Time series of modelled horizontal velocities on a 2 km and a 1 km grid for the period 1990-2014 at the point location S2 shown in Figure 1C.

The geometry of the terminus plays an important role in parameterizing ice shelf melting, and therefore my pre-1999 geometry will influence the magnitude of the basal melt rates (Sect. 3.6). The difference in geometry results in modelled basal melt rates that are larger for the period 1999-2003, when JI begins to develop a large floating tongue and when the calving front was already largely floating. Relative to other studies, e.g. Motyka et al. (2011), my melt rate for 1998 is ~2 times larger (Fig. 39 and Table A13). While I choose here to compare the two melt rates in order to offer a scale perspective, I acknowledge the difference in geometry between the two studies.

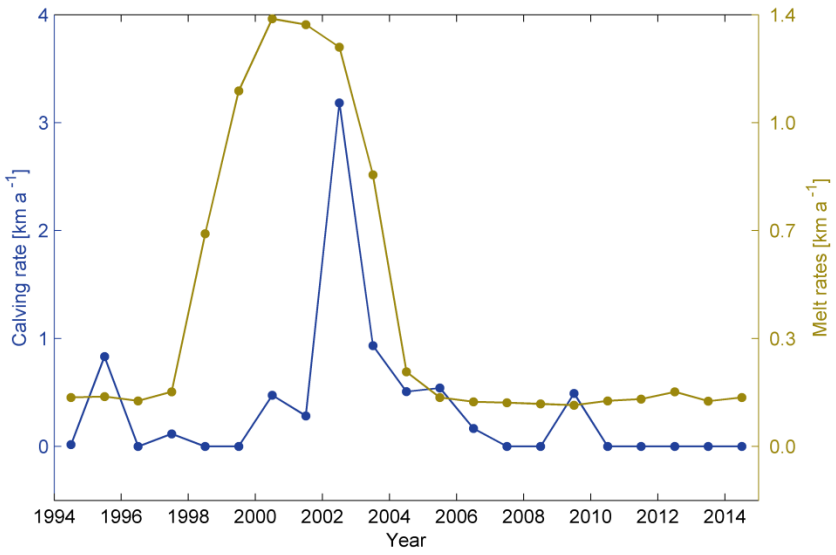

Figure 39: Calving rates versus basal melt rates for the period 1994-2014 in km a^{-1}. Note the 1995 and 2010 accelerations in calving rate which do not correlate with an increase in basal melt rates.

Starting in 2010, the retreat of the terminus modelled in my simulations did not correlate well with observations (Fig. 27). The observed terminus and the grounding line retreat do not cease after 2010. Furthermore, observed front positions (Joughin et al., 2014) suggest that by the summer 2010 JI was already retreating over the sill and on the over deepening indicated by the red star in Fig. 29. The observed retreat is not reproduced in my simulations suggesting that additional feedbacks and/or forcings most likely affect the glacier. Alternatively, the mismatch between observations and simulation results may represent an incomplete modelling of the physics, inaccuracies in atmospheric/oceanic conditions, or other various limitations (e.g., bed topography model constraints and grid resolution issues). The particular influence of these potential issues on my model is detailed below.

The basal topography of JI's channels represents a large source of uncertainty. JI is a marine terminating glacier whose bedrock topography is characterized by a long and narrow channel with deep troughs (Fig. 7) that contribute to its retreat and acceleration, e.g. once the grounding line starts to retreat on a down-sloping bed, the flow increases, leading to further retreat and acceleration (Vieli et al., 2011). The timing and the magnitude of these retreats depend on bed topography and the glacier width changes (Jamieson et al., 2012; Enderlin et al., 2013). Accurate modelling of the grounding line behaviour is, therefore, important for JI's dynamics as its retreat removes areas of flow resistance at the base and may trigger unstable retreat if the glacier is retreating into deeper waters. In my simulation, the grounding line position stabilizes downstream of the sill after 2005 (Figs. 27 and 29), which is in accordance with previous modelling studies (Vieli et al., 2001; Vieli et al., 2011). Vieli et al. (2011) found that, by artificially lowering the same bed sill by 100 m, the grounding line eventually retreats and triggers a catastrophic retreat of 80 km in just over 20 years. In an equivalent experiment with Vieli et al. (2011) but performed with my model, lowering the bed sill by 100 m, did not result in a retreat of the grounding line over the sill. Regarding the grid resolution, simulations performed on a 1 km grid did not improve my simulations of ice thickness (Fig. 36) or surface speed (i.e., trend, overall magnitude, and shape of the flow; Fig. 37).

From a climatic perspective, the summer of 2012 was characterized by exceptional surface melt covering 98 % of the entire ice sheet surface, including the high elevation Summit region (Nghiem et al., 2012; Hanna et al., 2014). Overall, the 2012 melt-season was two months longer than the 1979–2011 mean and the longest recorded in the satellite era (Tedesco et al., 2013). Furthermore, the summer of 2012 was preceded by a series of warm summers (2007, 2008, 2010 and 2011) (Hanna et al., 2014). Surface melt above average was already recorded in May-June 2012 (see Fig. 3 from NSIDC (2015)) when most of the 2011-2012 winter accumulation melted and over 30 % of the ice sheet surface experienced surface melt. An intense and long melt year leads to extensive thinning of the ice and has the potential to enhance hydrofracturing of the calving front due to melt water draining into surface crevasses

(MacAyeal et al., 2003; Joughin et al., 2013; Pollard et al., 2015) resulting in greater and/or faster seasonal retreat and an increase in submarine melt at the terminus and the sub-shelf cavity (Schoof, 2007; Stanley et al., 2011; Kimura et al., 2014; Slater et al., 2015).

The seasonal retreat of JI's terminus started relatively early in 2012, with a large calving event having already occurred in June. While it seems difficult to attribute this particular calving event solely to processes related to the 2012 melt season, it does seem probable that the series of warm summers (2007-2011) together with the 2012 exceptional melt season could have enhanced hydrofracturing of the calving front. In turn, this could have induced a retreat of the terminus that cannot be captured by my model (i.e., in its present configuration the model does not account for the influence of meltwater runoff and its role in the subglacial system during surface melt events). In my model, the atmospheric forcing applied (Sect. 2.1) can influence JI's dynamics only through changes in surface mass balance (SMB) (i.e., accumulation and ablation). While these changes in ice thickness affect both the SIA and the SSA (Sect. 2.1), the effect in the SIA is very weak as the driving stresses are not affected by a few meters of difference in thickness induced by SMB variability. In the SSA, the coupling is achieved via the effective pressure term in the definition of the yield stress (see Sect. 3 for detailed equations). The effective pressure is determined by the ice overburden pressure (i.e., ice thickness) and the effective thickness of water in the till, where the latter is computed by time-integrating the basal melt rate. Compared with SIA, this effect is stronger and may explain why in my model some seasonal velocity peaks could potentially be influenced by the atmospheric forcing applied (Fig. 35).

Finally, regarding the ocean conditions, warm water temperatures in the fjord were recorded in 2012. Besides a cold anomaly in 2010, which was sustained until early 2011, the period 2008-2013 is characterized by high fjord waters temperatures - equal to or warmer than those recorded in 1998-1999 (Gladish et al., 2015). In my model, the ice melt rates are determined from the given conditions in temperature (-1.7 °C), and salinity (35 psu) of the fjord waters, and the given geometry (Sect. 3.6). The fact that I am able to model JI's retreat with a constant ocean temperature suggests that the retreat and acceleration observed at JI are not likely to be controlled by the year to year variability in ocean temperatures. This conclusion agrees with the observational study of Gladish et al. (2015) who analysed ocean temperature variability in the Ilulissat fjord with JI variability and who found that after 1999 there was no clear correlation. My results do not, however, imply that the ocean influence in JI's retreat is negligible (Fig. 34), but rather that the glacier most likely responds to changes in ocean temperature that are sustained for longer time periods, e.g. decadal time scales.

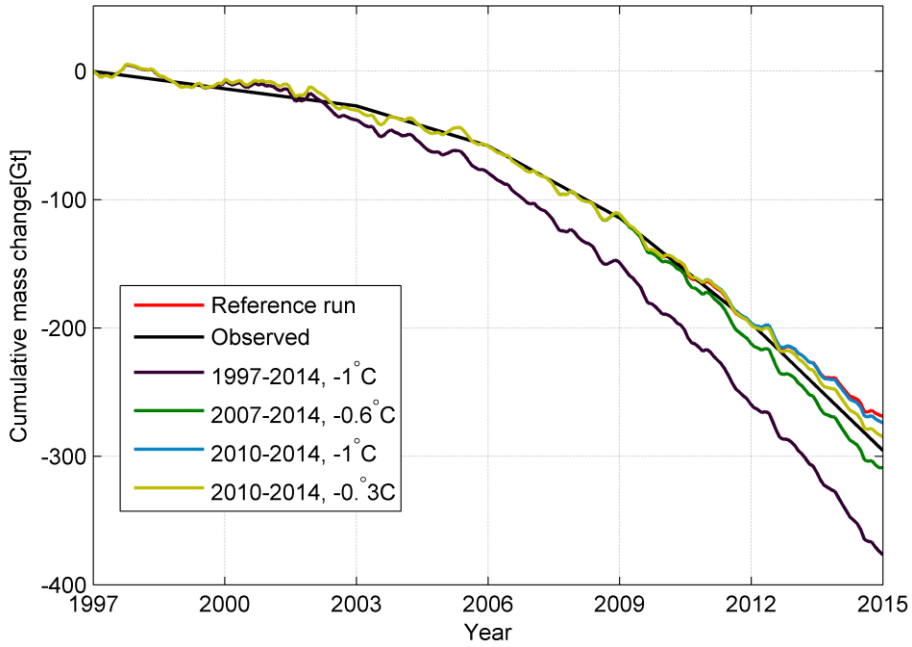

Figure 40: Cumulative mass change at JI for different ocean temperature experiments. In the experiment indicated by a dark green line, the reference ocean temperature (-1.7 °C) is adjusted from 2007-2014 with +1.1 °C, where +1.1 °C represents the mean surface ocean temperature between 2007 and 2014 (Gladish et al. 2015). In the experiment represented by the light blue line, the reference ocean temperature (-1.7 °C) is adjusted from 2010-2014 with +0.7 °C. In the remaining two experiments the input ocean temperature is adjusted starting 1997 (dark purple line) and 2010 (dark yellow line) with ocean temperature change calculated relative to 1990s (Gladish et al. 2015). These two experiments are consistent with observations of ocean temperature at the mouth of the Ilulissat fjord (Gladish et al. 2015). The curves for the reference run (red line), the "2010-2014, -1°C" experiment (light blue) and the "2010-2014, -0.3°C" experiment (dark yellow) are superimposed for the period 1990-2010. Note the large mass loss modelled in the experiment "1997-2014, -1°C" (dark purple line).

Two additional experiments, where the input ocean temperature (T_o) was increased to -1 °C indicate that higher melt rates beneath the grounding line could potentially explain the retreat observed after 2010. In my first experiment, the input T_o was increased from -1.7 °C to -1 °C starting 1997 (~0.7 °C relative to 1990). This temperature increase is consistent with observed ocean temperatures at the mouth of the Ilulissat fjord (Gladish et al., 2015) and generated in my simulation, for the period 1997-2014, an accelerated retreat of the front that does not correlate with observations (Fig. 41). Similarly, mass loss estimates from the simulations are significantly larger (by ~50 %; Fig. 40) than those calculated from airborne and satellite altimetry observations (Sect. 2.4).

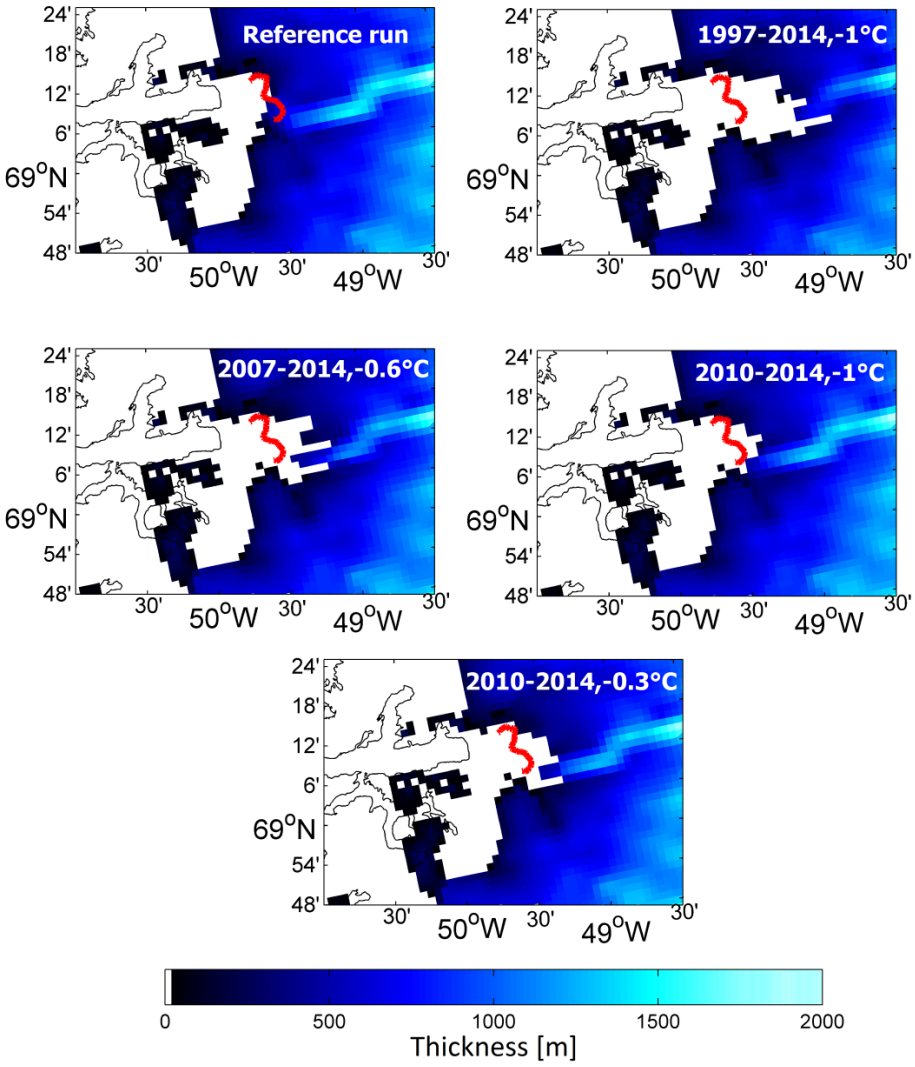

Figure 41: Terminus positions at the end of the forward run corresponding to December 2014 for the experiments introduced in Fig. 40 above. The red line represents the observed 2014 terminus position. Note the large terminus retreat for the experiment "1997-2014, -1°C" (top-right).

Overall, the experiment shows that an increase in ocean temperature that starts in 1997 and is sustained until 2014 generates modelled estimates for the period 1998-2014 that do not agree with observations. In the second experiment, T_o was increased to -1 °C starting in 2010 (~+0.7°C at the base of the shelf in 2010). For the period 2010-2014, my model predicted a faster retreat of the front that correlated well with observations (Fig. 41), and an increase of mass loss by ~7 Gt (Fig. 40). This experiment shows that an increase in ocean temperature beginning in 2010 could potentially explain the retreat observed thereafter.

CHAPTER 7

Study 4: Jakobshavn Isbræ prognostic simulations (2013-2100)

The goal of this study is to perform prognostic simulations (projections) of JI's behaviour in the 21st century. Using my historic simulation (i.e., Study 2; Sect. 5) I projected forward in time for the period 2013-2100. The results obtained in Study 2 and Study 3, suggested that the ocean influence in JI's behaviour over the last century is significant. Therefore, for the 21st century runs, 2013-2100, the model is forced by two climate projection scenarios, RCP 4.5 and RCP 8.5 (Fig. 4), and five SST scenarios (Fig. 5). I forced the model with yearly atmospheric forcing (i.e., air temperature and SMB from HIRHAM5, Sect. 2.1.2) and I used both constant (i.e., -1.3 °C) and variable surface ocean water temperature (Fig. 5). To ensure a smooth transition in air temperature and SMB between the BOX climate used in Study 2 and the RCP scenarios (Sect. 2.1.2), I computed and forced the latter as anomalies with respect to the mean 2000-2010 BOX air temperature and SMB (Peter Langen, personal communication).

For the input surface ocean temperature used (which represents the mean surface ocean temperature in the grid cells adjacent to the JI terminus), I computed (i.e., relative to a starting temperature of -1.3 °C; see Fig. 5) 10 year intervals of SST

changes, which I then used as an input to the meting parametrization (Sect. 3.6). The 10 years intervals of SST (10×9) were obtained by considering a linear increase in ocean surface temperature (Yin et al., 2011) and are divided in mild (Scenario A, 0 °C increase), intermediate (Scenario B, 1 °C increase), and harsh (Scenario C, 3°C increase) (see Sect. 2.2.2). Additionally, I performed two simulations where I assumed for the period 2020-2040 a decrease in surface ocean temperatures similar with the period 1970-1990 (Sect. 2.2.2; Scenario D1 and Scenario D2).

Similar with Study 2 and Study 3, in this regional model, all boundaries (calving fronts, grounding lines, upper, and lower surfaces) were free to evolve in time both during the regional equilibrium and the forward simulations. Along the ice shelf calving front, I superimposed a physically based calving (eigen-calving) parametrization (Winkelmann et al., 2011; Levermann et al., 2012) and a basic calving mechanism (Albrecht et al., 2011) that allowed the glacier terminus to advance and retreat under the applied forcings. The values of the ice sheet model parameters used (see Sect. 3 for the underlying equations) are included in Table A14.

In this study, I would like to focus on modelling the terminus advance and/or retreat and the speed fluctuations observed at JI during the period 2013-2100. First and foremost, the study wishes to experiment if any major collapses should be expected at JI in the next century and their relation with an increase/decrease in surface ocean temperatures, especially as JI is known to retreat after 2012 on a downward-sloping, marine-based bed. Secondly, the study wishes to constrain the previous modelled mass loss estimates (e.g. Nick et al., 2013) that should be expected from the JI basin in the next century and hence, the contribution to the SLR.

For this purpose, I performed 10 regional JI simulations (excluding any preparatory and additional experiments). The simulations are summarized in Table 2.

This is the first study, to my knowledge, where the prognostic simulations are built on a numerical model that has been calibrated for more than 100 years (i.e., Study 2). The study is unique both in approach and results obtained. The study is associated with Paper iii (manuscript) attached in Appendix H.

7.1 Results

7.1.1 Modelled terminus retreat, surface elevation and horizontal surface velocities

The modelled terminus retreat and/or advanced under the different climate forcing scenarios (Fig. 5 and Table 2) is shown in Fig. 42. Under both the RCP 4.5 and the RCP 8.5, the simulations indicate a retreat of the terminus for the period 2013-2100 of ~30 km in Scenario A, ~30 km in Scenario B, and ~40 km in Scenario C. While, one major terminus collapse is modelled in 2071 in Scenario A, and 2047 in Scenario

B, two major terminus collapses are modelled in Scenario C. According to Scenario C, the major terminus collapse (~30 km) at JI will occur in 2034 and will be

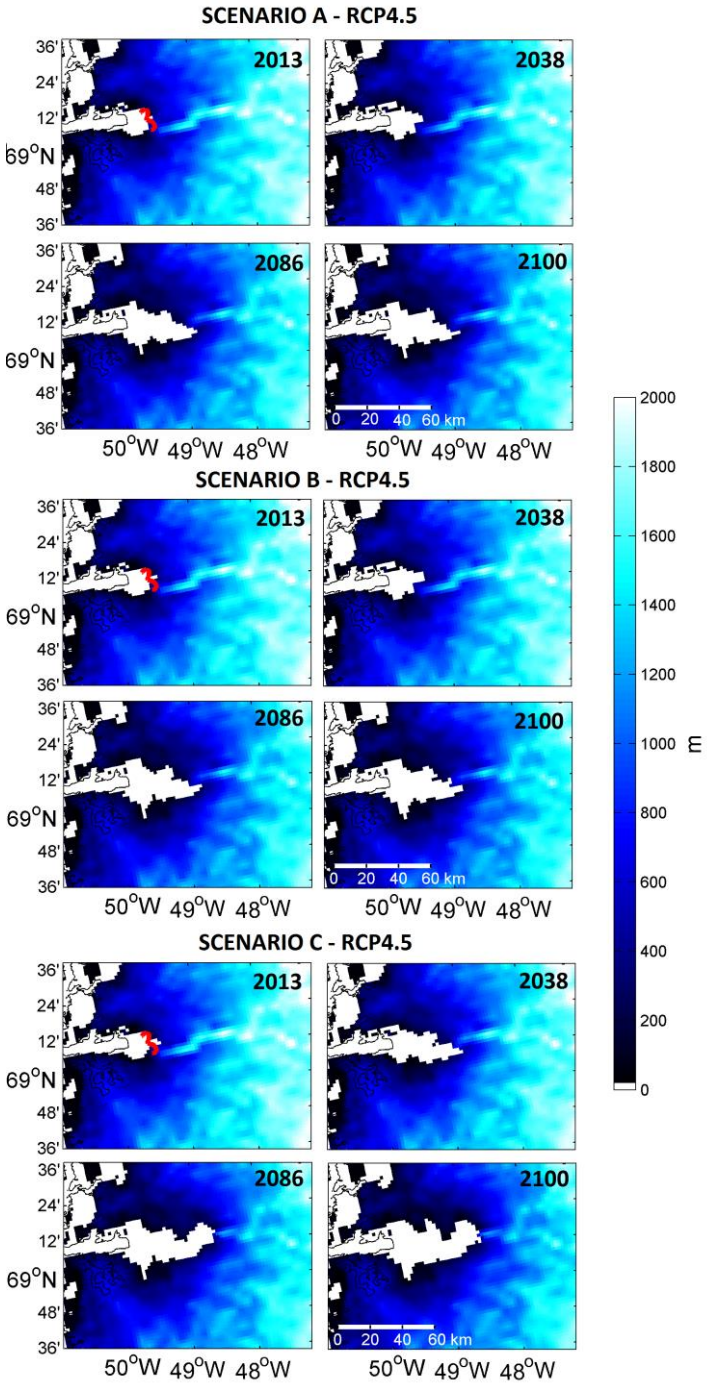

Figure 42: Modelled terminus retreat at JI between 2013-2100 for Scenario A, Scenario B and Scenario C built under RCP 4.5. The colorbar shows the ice thickness in meters. The red line denotes the 2012 observed terminus position.

followed by a similar but less significant event (~10 km) in 2083. In my simulations, these modelled episodes of rapid retreat occur at different time intervals but generally at the same location (see Fig. 43).

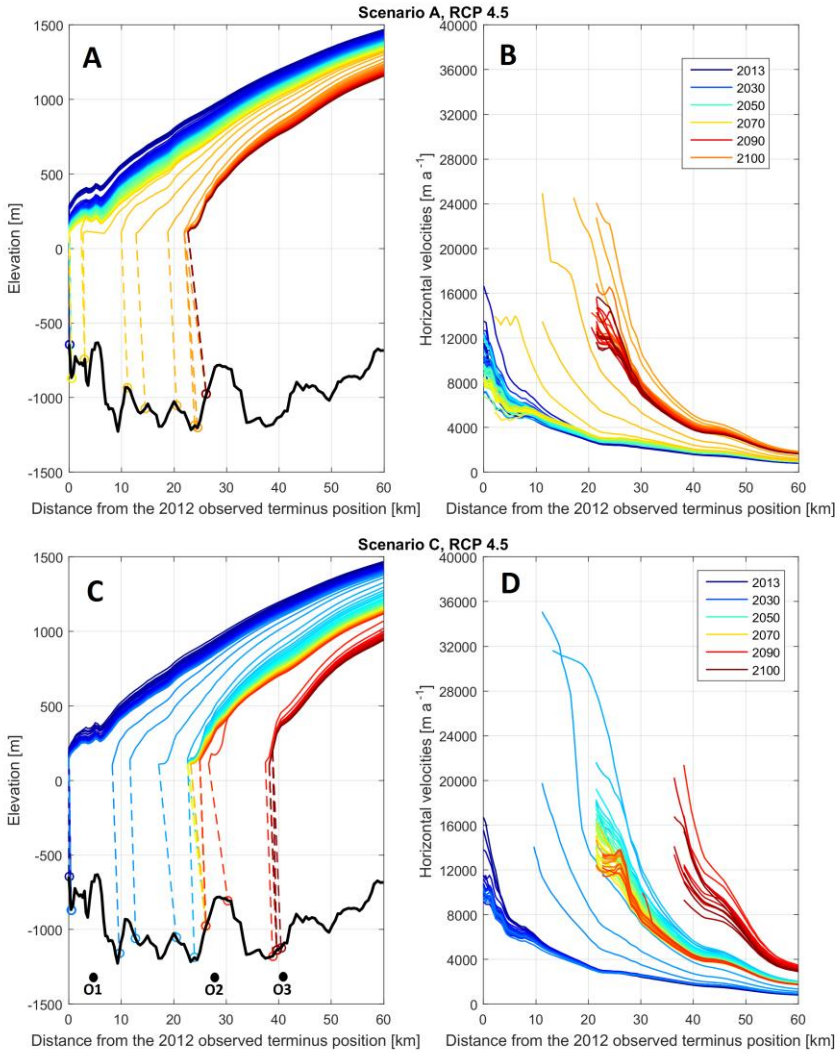

Figure 43: Modelled surface elevation (>100 m) and grounding line position (A) and modelled horizontal velocities (B) at JI along the dashed flow-line shown in Fig. 1D during the period 2013-2100 for Scenario A. Modelled surface elevation (>100 m) and grounding line position (C) and modelled horizontal velocities (D) at JI along the flow-line shown in Fig. 1C during the period 2013-2100 for Scenario C. The black line represents the bedrock topography from Bamber et al. (2013). The colour scale ranges from dark blue (2013), light blue, green (2050), yellow, orange to red (2100) (see the legend). The dots represent modelled grounding line positions where the colours follow closely the colour scale used for surface elevation and horizontal velocities. The location of point O1 shows the position of the first sill. The location point O2 shows the position of the second sill and denotes a possible pinning point for JI. The location of point O3 denotes a second possible pinning point.

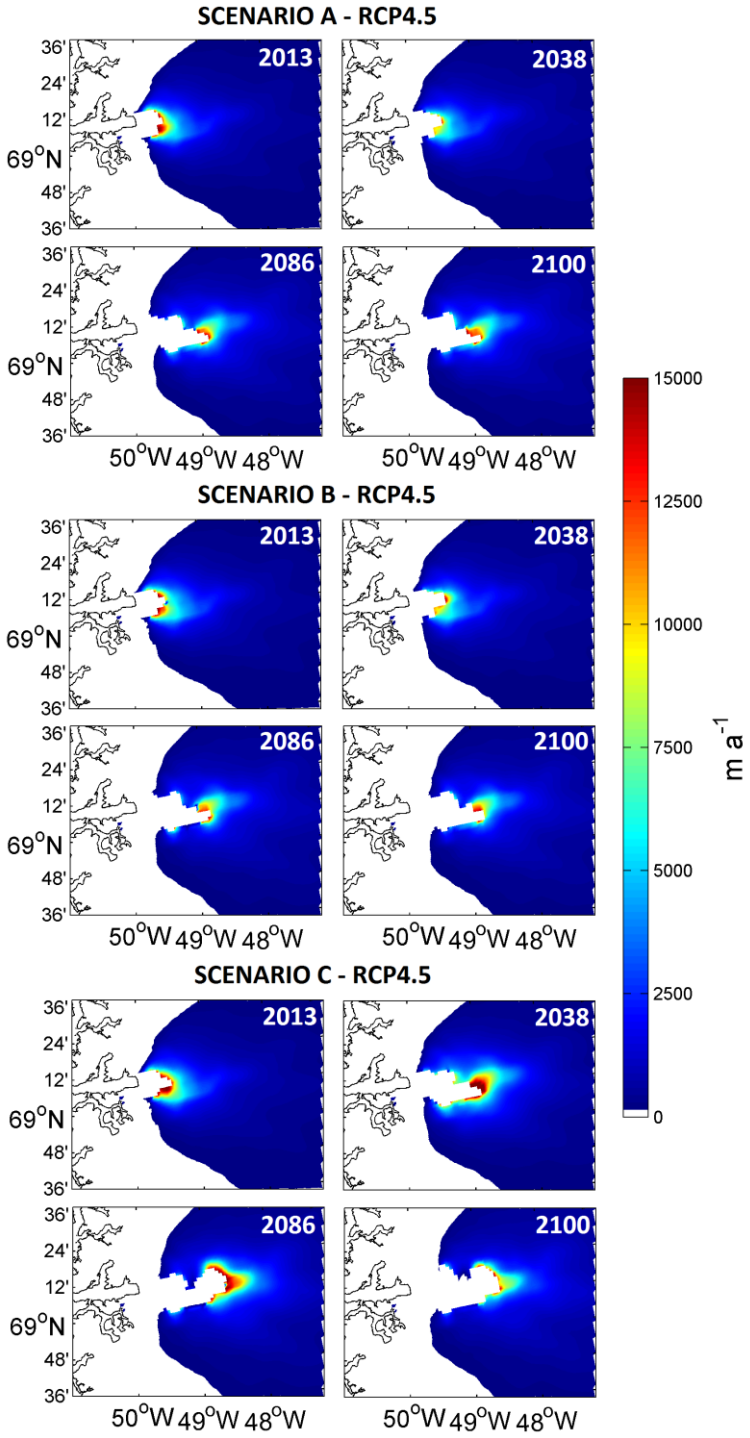

Figure 44: Modelled horizontal surface velocities at JI between 2013-2100 for Scenario A, Scenario B and Scenario C built under RCP 4.5. The colorbar shows the magnitude of the horizontal surface velocities in m a^{-1}.

The modelled horizontal velocities under the different climate forcing scenarios (Fig. 5, and Table 2) are shown in Figs. 43 and 44. In Scenario A, the velocities remain relatively stable during the period 2013-2070 (~12 000 m a^{-1}) and accelerate once the

terminus starts to retreat on the downward-sloping bed (Fig. 43A,B). Speeds as high as 24 000 m a^{-1} are modelled during the terminus retreat (~2071). Nonetheless, after the retreat ceased, the horizontal velocities decreased to 16 000 m a^{-1} (Fig. 43B), value that they maintained until the end of the century. Similarly to Scenario A, in Scenario C, two flow accelerations are simulated in 2034 and 2083, which correlate with the two modelled terminus retreat events (Fig. 43C,D). In Scenario C, speeds as high as 35 000 m a^{-1} are modelled during the first major terminus collapse, and as high as 20 000 m a^{-1} during the second but less significant terminus collapse. According to Scenario C, by the end of the century the modelled horizontal velocities decrease to values that range between 10000 m a^{-1} to 14 000 m a^{-1} as the terminus ceased to retreat and stabilized at the lower end of the upward-sloping bed. In contradiction with present day observed and modelled JI flow accelerations, both accelerations seem to be short lived and once the grounding line reached higher ground (~2050 and ~2080), the modelled velocities decreased to values similar or smaller (i.e., ~2090) than those simulated before the acceleration (Fig. 43). In my simulations, the modelled accelerations in flow speed correlate with the modelled terminus retreat. Further, and similar with the modelled terminus retreat, the modelled flow accelerations occur at different time intervals (i.e., relative to the climate forcing applied) but generally at the same location (see Fig. 43).

7.2 Modelled ice mass changes

After 2013, the mass loss continues to accelerate in my simulations and correlates with the terminus retreat and thinning discussed in Sect. 7.1. Following the initial and major acceleration of JI which occurs in 2071 in Scenario A and 2034 in Scenario C, the modelled mass change accelerates thereafter. Overall, an acceleration in mass is modelled every time a retreat of the terminus occurs (e.g. in ~2040 and ~2080 in Scenario C). Mass change estimates that vary between 2019 Gt or 24 Gt a^{-1} (Scenario A) and 3275 Gt or 38 Gt a^{-1} (Scenario C) are modelled between 2016-2100. The mass change estimates are at the same magnitude with those suggested by Nick et al. (2013). Table 3 summarizes mass loss estimates and major terminus collapses at JI for the period 2016-2100.

Figure 45 shows observed and modelled mass change estimates for Scenario A, Scenario B and Scenario C. Separating the dynamic and the SMB derived mass loss between the different simulations performed, I found that between 74 % and 86 % of the mass loss is dynamic in origin, while only 14 % to 26 % is caused by a decrease in SMB. For the period 1990-2014 dynamically driven discharge has been shown to control Jakobshavn's mass loss (Nick et al., 2013). Similarly, here, the dynamical driven discharge will continue to control JI's mass change by the end of the century.

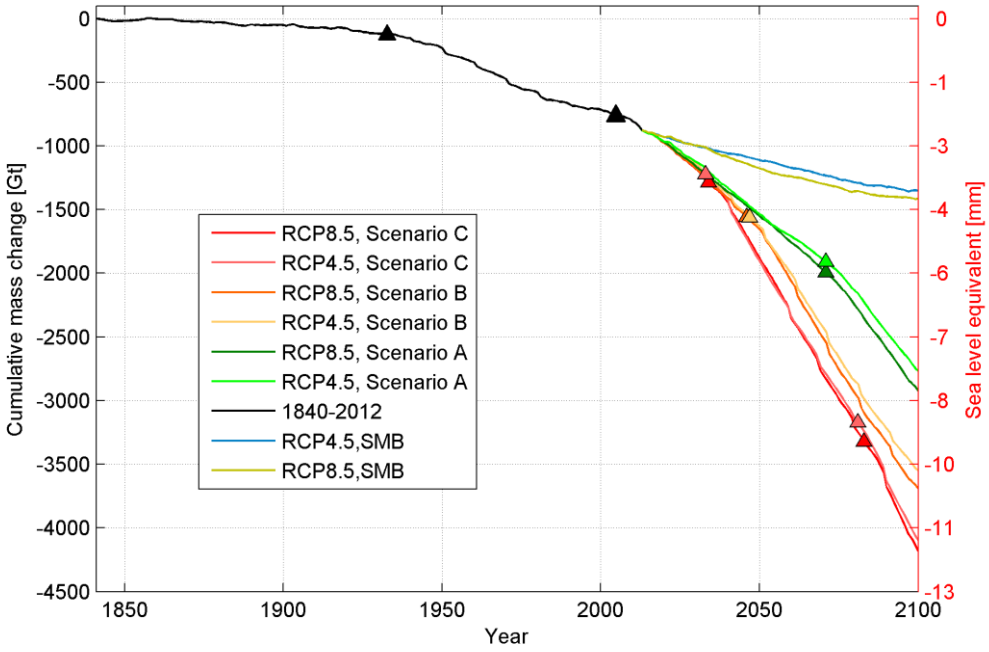

Figure 45: Modelled and observed cumulative mass change for Jakobshavn Isbræ for the period 1840-2100. The black curve denotes the mass change simulated between 1840-2012 in Study 2 (Sect. 5). The light blue curve represents the mass change due to SMB under the RCP 4.5 scenario (Sect. 2.1.2) after the 2000–2010 baseline is removed (~453 Gt). The "golden olive" curve represents the mass change due to SMB under the RCP 8.5 scenario (Sect. 2.1.2) after the 2000–2010 baseline is removed (~515 Gt). The red to light green curves represent the total modelled mass change for the period 2013-2100 for Scenario A, Scenario B and Scenario C under RCP 4.5 and RCP 8.5 scenarios. The filled triangles denote modelled major terminus collapses for the period 1840-2100.

Table 3: Modelled mass loss estimates (dynamic vs. SMB mass), mass loss rates, major terminus collapses, and mass loss increase (i.e., relative to 1840-2012) at JI during the period 2016-2100.

Scenarios		Mass loss (Gt)	Mass loss type (%)		Mass loss rate (Gta^{-1})	Major terminus collapse (year)	Increase relative to 1840-2012 (%)
			Dynamic	SMB			
Scenario A	RCP8.5	2018.73	74	26	24	2071	81 %
(+0 °C)	RCP4.5	1859.94	76	24	22	2071	67 %
Scenario B	RCP8.5	2786.70	82	18	33	2046	149 %
(+1 °C)	RCP4.5	2641.03	83	17	32	2047	136 %
Scenario C	RCP8.5	3274.71	84	16	39	2033;2081	192 %
(+3 °C)	RCP4.5	3191.04	86	14	38	2034;2083	184 %

The estimates regarding the overall contribution to SLR for the period 2016-2100 vary between ~5.2 mm SLE (or 127 % relative to 1840-2012) in Scenario A to ~ 9.1 mm SLE (or 248 % relative to 1840-2012) in Scenario C.

7.3 Discussion

The 21st century simulations resulted in large mass loss estimates even for the mildest of the scenarios used (Table 3). In contrast with the 1930 acceleration, in the 21st century, JI's terminus continues to retreat over a downward-sloping, marine-based bed into deeper water and therefore sustained high velocities are modelled throughout the century. Further, I found that in my simulations, these modelled episodes of rapid retreat occurred at different time intervals but generally at the same location (see Fig. 43). The 2033 collapsed of the terminus under Scenario C resulted in a doubling of the modelled speed (i.e., relative to present day values; Fig. 43D). However, in contradiction with present day observed and modelled JI flow accelerations, these 21st century accelerations seem to be short lived and once the grounding line reached higher ground (i.e., ~2050 and ~2085 in Scenario C), the modelled velocities decreased to values similar or smaller (i.e., ~2090) than those simulated before the acceleration (Fig. 43). Even in the best case scenario (Scenario A, i.e. no increase in ocean temperatures), once the terminus succeeded to retreat over the sill and into the large over deepening that characterizes JI's bed (indicated by point O1 in Fig. 43), an irreversible collapse of the terminus was triggered. This shows that although, the terminus retreat was likely initiated by the ocean parametrization used, the prime driver for JI's subsequent response remained its own bed topography.

As seen in the simulations performed with Scenario C, after the first major collapse of the terminus (i.e., ~2033), the front remained relative stable for the next 24 years in the proximity of point O2 (Fig. 43). Therefore, this location close to the point O2 has all the necessary features to become a new pinning point for JI in the next century. According to Scenario C, by the end of the century the modelled horizontal velocities decrease to values that range between 10000 m a^{-1} to 14 000 m a^{-1} as the terminus ceased to retreat and stabilized at the lower end of an upward-sloping bed (point O3 in Fig. 43). Therefore, once the terminus and grounding line will reach the location of point O3, this new geometry of JI and the fact that the grounding line will start to retreat on an upward-sloping bed will most probably result in a decrease in speeds.

Further, I forced the model between 2020 and 2040 with 20 years of cooling similar to what occurred between 1970-1990 (Fig. 5). I found that 0.5 °C of oceanic cooling (Scenario D2) will slow down the retreat – resulting in a much smaller chance of early 21st century collapse. I also found that 0.9 °C of oceanic cooling (Scenario D1) will make JI advance to its 1990 position. In both cooling scenarios, the major

terminus retreat is delayed with ~20 years relative to Scenario C (~2055; Fig. 43). In contrast with Scenario D1, in Scenario D2, two terminus collapses are model in ~2054 and ~2097.

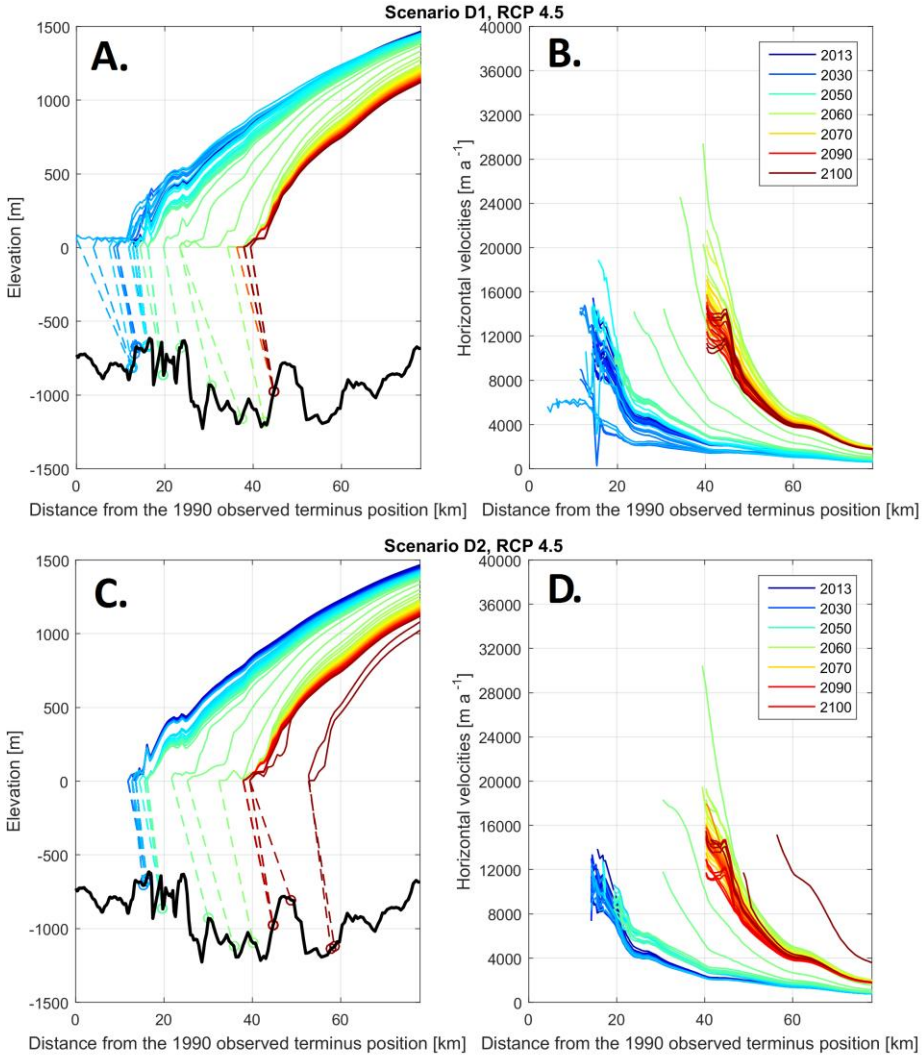

Figure 46: Modelled surface elevation (> 0 m) and grounding line position (A), and modelled horizontal velocities (B) at JI along the flow-line shown in Fig. 1C during the period 2013-2100 for Scenario D1. Modelled surface elevation (> 0 m) and grounding line position (C), and modelled horizontal velocities (D) at JI along the flow-line shown in Fig. 1C during the period 2013-2100 for Scenario D2 .The black line represents the bedrock topography from Bamber et al. (2013). The colour scale ranges from dark blue (2013), light blue, cyan (2050), green, yellow, orange to red (2100) (see the legend). The dots represent modelled grounding line positions with colours that follow closely the colour scale presented above.

In the best case scenario with regards to future warming, expected mass loss of JI amounts to ~1860 Gt by the year 2100, equivalent of 5.2 mm global sea-level rise.

In the worst case scenario with regards to future warming, expected mass loss of JI amounts to ~3275 Gt by the year 2100, equivalent of 9.1 mm global sea-level rise.

CHAPTER 8

Discussion

This chapter highlights the main findings of the thesis and brings together the discussion performed at the end of each study.

Study 2, Study 3 and Study 4 have shown that representing the processes that act at the marine boundary (i.e., calving and ocean melt) is important for understanding and modelling the retreat and/or advance of Jakobshavn Isbræ. In order to allow the glacier terminus to advance and/or retreat due to calving, I have used the superposition of two calving mechanisms (Sect. 3). The benefit of using such a combination of calving laws is that it can evolve the terminus position with time under the applied forcings and thus, potential calving feedbacks are not ignored. Generally, I find that the superposition of these two calving mechanisms performs well for relatively narrow and deep fjords as those characterized by JI. Preparatory experiments have shown that calving is mostly driven in my model by the basic calving mechanism used (> 90 % of the overall mass loss) and that the eigen-calving parametrization is important in modelling sub-annual to seasonal fluctuations of the terminus. The introduction of the basic calving mechanism was needed in order to accurately match observed front positions. However, the basic calving mechanism is not deeply rooted in JI's calving triggering processes, other than the fact that ice shelf calving fronts are generally thicker than 150–300 m (The PISM Authors, 2014). Therefore, and although, I found that the superposition of these two calving

mechanisms performed relatively well for JI, it represents just a compromise solution. Generally, more physically based calving laws (e.g., especially when prognostic simulation are involved) are needed. However, to represent calving front dynamics in a 2-D or 3-D ice sheet model remains significantly difficult. Even today, the amount of calving laws available for 3-D ice sheet models is very limited and rarely, physically based.

In terms of the bed topography, I used the dataset from Bamber et al. (2013) where the overall bathymetry was obtained by interpolating various bathymetric data from the entire Arctic Ocean (i.e., IBCAO v3 maps). In the Jakobshavn fjord, the bathymetric data are supplemented with soundings performed by CReSIS (Sect. 2). As seen in my simulations, the terminus retreat and flow acceleration are largely topographically controlled and thus, any errors in the bed topography could potentially affect the modelling results. For example, after the terminus and the grounding line retreat from a basal high through an overdeepening, flow acceleration is modelled. If the overdeepning is improperly shaped, this can influence both the terminus retreat and the flow acceleration. The Ilulissat fjord is frozen all year round making it inaccessible for research vessels and thus, the bathymetry data available in this region is generally limited. To overcome this issue, I have tried to supplement the available bathymetry set with data available in the Ilulissat fjord from annual surveys and instrumented seals (Gladish et al., 2015a,b). The seals are known to generally feed at the bottom of the fjords and therefore they could provide additional knowledge about the bathymetry. The dataset has been provided by Carl Gladish (personal communication). Overall, I have found good agreement with the bathymetry from Bamber et al. (2013) (Abbas Khan, personal communication). Nonetheless, the basal topography of JI's channels should be accounted as a possible source of uncertainty.

Regarding the grid resolution, sensitivity experiments performed on a 1 km grid (Sect. 6.2.3) did not show significant improvement with respect to ice thickness (Fig. 36) or surface speed (i.e., shape of the flow and overall magnitude; Fig. 37). These findings agree with Della-Giustina (2011). In terms of the spatial distribution of the flow, my simulations produce a more wide but overall short flow (i.e., relative to the distance it reaches inland), while observations suggest a more narrow flow that feeds deeper into the ice sheet (Joughin et al., 2012). However, the overall distribution of modelled and observed velocities suggests an overall good fit with observations (e.g. Fig. 17 in Study 1). A study published recently by Aschwanden et al. (2016) showed progress in modelling the spatial resolution of the flow (i.e., for "isbræ" type glaciers) by using high resolution ice thickness data, by (i.e., main changes relative to my set of parameters) tuning q, the exponent of the pseudo-plastic basal resistance model that controls the basal shear in Eq. 25, and by tuning the bed roughness in the SIA (i.e., the bed roughness controls how the SIA stress balance models ice flow over bumpy bedrock topography). Performing a similar experiment but for my JI

model, I obtained improvement relative to the spatial distribution of the modelled flow (Fig. A13), but as my sensitivity experiments showed, increasing q in my model results in a faster retreat of the terminus and a doubling of the modelled mass loss for each 0.1 of increase (Fig. 33). This does not imply that the two setups are incompatible, but highlights that generally, more thought and tuning of the parameters involved is required for making the transition smooth. Further, the same study by Aschwanden et al. (2016) showed that a resolution of 2 km is enough to reasonable capture the flow at JI. The particular influence of these potential limitations on my model was detailed in Study 3.

In Study 2, I modelled the behaviour of JI since the end of the LIA (1840-2012). The present study is the first that aimed and succeeded to capture reasonably well JI's behaviour in the last century. This longer-term reconstruction of glacier behaviour back to the end of the LIA provided new insight in understanding JI's behaviour over more than 100 years and had the capability to ensure long term calibrated projections. Overall, I obtained a good agreement between observed and modelled time series of horizontal velocities and ice thickness changes (Figs. 23, 24 and 25). I found a first modelled acceleration of JI in 1930 when the grounding line retreated over a reversed bed slope (Fig. 21). In my simulations, this initial acceleration of JI was responsible for large surface lowering, and can explain the surface lowering observed by Weidick (1969) and Csatho et al. (2008) during this period (Figs. 22 and 26). Although, the acceleration could potentially be inferred from observations of terminus retreat which during that period suggest a large retreat of the terminus (Csatho et al., 2008), it was neither modelled before nor referenced in any other scientific publication. Further, this acceleration illustrates that the dynamic response to a loss of buttressing is transient and it is largely topographically controlled. The 1930 acceleration in terminus retreat and flow speed was captured even in a simulation with constant ocean forcing (Fig. 21B), suggesting that the acceleration was probably not triggered by an increase in ocean temperature (e.g. warm ocean waters entering the Ilulissat fjord that could destabilize JI). Nonetheless, I found that overall, the ocean influence in JI's behaviour over the last century is significant and most of JI's retreat during 1840–2012 is driven by the ocean parametrization used and the glacier's subsequent response, which is largely governed by bed geometry (Fig. 26).

The period 1960-1990 is characterized in my model by stable terminus positions and an overall slowdown in mass loss. Observational data (i.e., atmospheric and oceanic temperature in the JI region) suggests that, during this period, the observed terminus retreat decelerates, most probably, as a consequence of colder climate conditions (Sect. 2). Similarly, in my simulation, the slowdown modelled in terms of terminus retreat is triggered by an overall decrease in ocean temperature of 0.5 °C (i.e., between 1970 to 1990). Further, and in agreement with existing observations, I found

a second acceleration that occurs in my model between 1999-2003 (Figs. 21 and 22) and is largely controlled by the bed topography (see Fig. 21). Therefore, in my simulations, and similarly with Nick et al. (2013), these episodes of rapid retreat occur at different times but generally at the same location (see the location for the 1930 and 2003 accelerations in the simulation with variable ocean forcing vs. the simulation with constant ocean forcing; Fig. 21).

In Study 3, I attempted and succeeded to model the recent behaviour of JI (i.e., 1990-2014). Relative to Study 2, here, I focused more on glacier dynamics - the seasonal driven terminus advance and/or retreat and speed fluctuations of JI during the period 1990-2014. Overall, I obtained a good agreement of my model output with time series of measured horizontal velocities, observed thickness changes, and GPS derived elastic uplift of the crust. I found that representing the processes that act at the marine boundary (i.e., calving and ocean melt) is the key for modelling the temporal variability of the flow at JI. In a simulation in which the terminus position is kept fixed to the 1990s position (Study 1), the velocity peaks are uniform (i.e., no acceleration is modelled except for some small seasonal related fluctuations generated by the atmospheric forcing applied). In agreement with previous studies (e.g. Joughin et al., 2012), my results suggest that the overall variability in the modelled horizontal velocities is a response to variations in terminus position (e.g. Fig. 29). Further, my model reproduced two distinct flow accelerations in 1998 and 2003 that are consistent with observations. The first was generated by a retreat of the terminus and moderate thinning prior to 1998; the latter was triggered by the final breakup of the floating tongue. During this period, JI attained in my simulations unprecedented velocities as high as 20 km a^{-1}. Additionally, the final break-up of the floating tongue generated a reduction in buttressing that resulted in further thinning. In this model, the seasonal variability was likely driven by processes related to the atmospheric forcing applied (e.g. temperature and SMB variability), which in fact represented the only seasonal input used in the model. The greater-than seasonal frequency seen in this study was attributed to grid resolution and missing seasonal-scale processes (e.g. ice mélange variability or seasonal ocean temperature variability) in the model. Therefore, for modelling seasonal scale processes grid resolutions >2 km are probably indicated. The grounding line migration will also benefit from finer resolutions.

Similar with Study 2, the results obtained in Study 3 suggested that most of the JI retreat during 1990–2014 was driven by the ocean parametrization and the glacier's subsequent response, which was largely governed by its own bed geometry (e.g. Figs. 29, 30 and 34). Finally, the 2010–2012 observed terminus retreat (Joughin et al., 2014) was reproduced neither in Study 2 nor in Study 3, most likely due to inaccuracies in basal topography or misrepresentations of the atmospheric forcing and the ocean parametrization that I used. Additional sensitivity experiments showed

that an increase in ocean temperature of 0.7 °C for the period 2010–2014 may trigger a retreat of the terminus that agrees better with observations (Fig. 40).

Further, according to observations, JI terminus became afloat sometime around 1946 and by 1997 the glacier is characterized by a large floating tongue (> 10 km; e.g. Motyka et al., 2011) that I am not able to simulate in Study 2 or in Study 3 (Figs. 21 and 29). In Study 3, the glacier starts to develop a larger floating tongue (~10 km) in 1999. Starting in 2000, the floating tongue is comparable in length and thickness with observations and the model is able to simulate, with a high degree of accuracy, its break-up that occurred in late summer 2003 and the subsequent glacier acceleration. In Study 2, a larger floating ice tongue starts to develop in ~1870, ~1920 and ~1980. Generally, these modelled ice tongues are shorter lengthwise than those suggested by observations (Csatho et al., 2008) and except the 1870 floating ice tongue which is calved only in ~1915, the 1920s and 1980s ice tongues are calved within several years after their development (Fig. 21). In my simulations, the modelled terminus retreat tends to follow closely the modelled grounding line retreat, i.e. only a small floating ice tongue is modelled (~2 to 4 km). Comparing Study 2 with Study 3, I found that generally when the model is forced with seasonal forcing (e.g. monthly atmospheric forcing in Study 3), the model tends to favour the development of larger floating tongues. Not being able to simulate a large floating tongue before 2000, may suggest limitations of the bed topography used (e.g. the bed geometry simply does not sustains the development of such large floating tongues) or missing seasonal-scale processes (e.g. ice mélange variability or seasonal ocean temperature variability). Alternatively, it may also represent a limitation of the melting parametrization used which for my choice of parameters could not favour the development of large floating ice tongues, limitations of the calving mechanisms used, or a combination of both. These potential limitations were discussed in detail for each study (see Sect. 5 for Study 2 and Sect. 6 for Study 3).

The geometry of the terminus plays an important role in parametrizing ice shelf melting (Sect 3.), and therefore misshapen geometries (e.g. my 1990-1999 geometry in Study 3) will influence the magnitude of the basal melt rates (Sect. 6.3). Overall, differences in geometry result in modelled mean basal melt rates that tend to increase exponentially when JI begins to develop a larger floating tongue. For example, in Study 3, the modelled mean melt rates for the period 1999–2003 are large and likely overestimated (Table A13).

The results obtained in Study 2 (Sect. 5), suggested that the ocean influence in JI's behavior over the last century is significant. Therefore, in Study 4, I used the historic simulation performed in Study 2, and I projected forward in time for the period 2013-2100 using two RCP Scenarios and five SST scenarios (Fig. 5). As seen in Fig. 43, in the 21st century, JI's terminus continues to retreat over a downward-sloping, marine-

based bed into deeper water and therefore, in my simulations, sustained high velocities are modelled throughout the century. In terms of terminus retreat, I found that even in the best case scenario (Scenario A, i.e. no increase in ocean temperatures), once the terminus succeeds to retreat over the sill and into the large over deepening that characterizes JI bed (indicated by point O1 in Fig. 43), an irreversible collapse of the terminus is triggered. In the worst case scenario (i.e., Scenario C), two collapses of the terminus should be expected by the end of the century with a retreat of up to 40 km along JI's downward-sloping bed. Similar with Study 2 and Study 3, these modelled episodes of rapid retreat occur at different time intervals but generally at the same location. Yet again, I found that although the terminus retreat is likely initiated by the ocean parametrization used, the prime driver for JI's subsequent response remains its own bed topography. Relative to present day observed and modelled JI flow accelerations (e.g. Study 3), I found that these 21st century accelerations are generally short lived and once the grounding line reached higher ground (i.e., ~2050 and ~2085 in Scenario C), the modelled velocities decreased to values similar or smaller (i.e., ~2090) than those simulated before the acceleration (Fig. 43). In scenario, D1 and D2, I forced the model between 2020 and 2040 with 20 years of cooling similar to what occurred between 1970-1990 (Fig. 5). I found that 0.5 °C of oceanic cooling (Scenario D2) will slow down the retreat – resulting in a much smaller chance of early 21st century collapse. I also found that 0.9 °C of oceanic cooling (Scenario D1) will make JI advance to its 1990 position. In both cooling scenarios, once cooling stops, the terminus retreat continues and the major terminus collapse is only delayed with ~20 years (i.e., relative to Scenario C; Fig. 43).

Finally, the modelled cumulative mass loss for the period 1840-2012 is 1214.5 Gt, of which 77 % is dynamic in origin and 23 % is attributed to a decrease in SMB (Fig. 26). Mass change estimates that vary between 2019 Gt or 24 Gt a^{-1} (Scenario A) and 3275 Gt or 38 Gt a^{-1} (Scenario C) are modelled between 2016-2100 (Fig. 45). From these values between 74 % and 86 % of the mass change is dynamic in origin, while only 14 % to 26 % is caused by a decrease in SMB.

8.1 Limitations

Beside the limitations mentioned above (e.g. bed topography), I will further introduce some general limitations of ice sheet models which also need to be taken into account.

First, observations play a fundament role in ice sheet modelling. While some of them are used as input data, large parts are used to validate the models. Even today the available observations are often uncertain, sparse in time and space and indirect (e.g. trimlines). These may result in poorly constrained models and physical parameters. Compared to Study 3, in Study 2 the amount of available observations before 1990 is

relatively low. Therefore, overall Study 3 performed only for the period 1990-2014 should represent a better constrained model.

Secondly, basal conditions are generally unknown, with the basal drag being one of the most uncertain model parameters. The basal drag plays a key role in determining sliding, i.e. when the driving stress exceeds the basal drag, sliding occurs. Generally, inverse methods can be used to infer the basal drag, however when modelling the temporal behaviour, the basal drag distribution changes with the bed topography variability and the ice thickness evolution as the terminus retreats (e.g. for JI the terminus retreats over 45 km from 1840 to 2007). Therefore, inferring for the basal drag is only suitable and effective in relatively short simulations or for those glaciers characterized by relatively stable terminus positions and consequently, stable ice geometries.

Thirdly, the modelling approach will always be biased by the modeler own choices and decisions, especially when tuning large sets of parameters to match observations (i.e., the choices are not always random). As an example, in Study 2, I calibrated the model such that it matches observed terminus positions, and so my choice for the basic calving mechanism thickness threshold (e.g. 400 m) could directly affect my choice of the melting parameter, Fmelt, and vice versa.

CHAPTER 9

Conclusions & outlook

In this thesis, a three-dimensional, time-dependent regional outlet glacier model is used to investigate the processes driving the dynamic evolution of JI between 1840 and 2100. The model was forced with different climate variables: near-surface air temperature, surface mass balance (SMB), sea-surface temperature and salinity (Sect. 2). The model parameters were calibrated such that the model reproduced observed front positions (Figs. A3 and 27) and ice mass change observations (Figs. 26 and 31) at JI over the periods 1840–2014 and 1997–2014, respectively. I obtained a good agreement of my model output with time series of measured horizontal velocities, observed thickness changes, and GPS derived elastic uplift of the crust (Fig. 32). The present thesis represents the first study, to my knowledge, that aimed and succeeded to capture with a 3-D dynamic numerical model the temporal behaviour of JI since the end of the LIA. The longer-term reconstruction of modelled glacier behaviour back to the end of the LIA provided new insight in understanding JI's behaviour over more than 100 years and had the capability to ensure long term calibrated projections. Overall, the study is unique both in approach and results obtained, and shows significant progress in modelling the temporal variability of the flow at JI.

My results suggest that the ocean influence in JI's behaviour over the last century is significant and most of the JI retreat during 1840–2014 is driven by the ocean parametrization and the glacier's subsequent response, which is largely governed by its own bed geometry (Fig. 26). In agreement with previous studies (e.g. Joughin et

al., 2012), my simulations suggest that the overall variability in the modelled horizontal velocities is a response to variations in terminus position (e.g. Fig. 29). In my simulations, the retreat of the front reduces the buttressing at the terminus and generates a dynamic response in the upstream region of JI which finally leads to flow acceleration. This buttressing effect tends to govern JI's behaviour in all my simulations (Fig. 30). Similar to previous studies (Nick et al., 2009; Vieli and Nick, 2011; Joughin et al. 2012), my results show that JI's dynamic changes are triggered at the terminus (e.g. Figs. 21, 26, 29 and 34).

In all of the simulations, I am not able to simulate the large floating tongue (> 10 km; e.g. Motyka et al., 2011) that characterized JI before 1997. I attribute this to limitations related with the bed topography, the melting parametrization, the calving mechanisms or to missing seasonal-scale processes (e.g. ice mélange variability or seasonal ocean temperature variability) at the terminus. Alternatively, it may also represent a combination of more processes. Sensitivity experiments performed on a 1 km grid did not show significant improvement with respect to ice thickness (Fig. 36) or surface speeds (i.e., shape of the flow and overall magnitude; Figs. 37 and 38). However, for modelling seasonal scale processes I suggest using grid resolutions higher than 2 km.

Overall, between 1840-2100, I found five terminus retreats and flow accelerations. An initial, and most probably the first significant acceleration of JI after the end of LIA, is modelled in ~1930. The 1930 acceleration could potentially be inferred from observations of terminus retreat which between 1930 and 1946 (see Fig. 21) suggest a large terminus retreat of ~8 km (see Fig. 8). In my simulations, this initial terminus retreat and flow acceleration of JI resulted in large speeds (~20 000 m a^{-1}), and were overall responsible for bringing the magnitude of the horizontal velocities at the level observed in ~1980 (see Fig. 21). Two other terminus retreat and flow accelerations consistent with observations (Joughin et al., 2012) were modelled in 1998 and 2003 (Fig. 29). In the 21st century runs, JI's terminus continues to retreat over a downward-sloping, marine-based bed into deeper water and therefore sustained high velocities are modelled throughout the century. Projections for the period 2013-2100, reveal one possible terminus collapse in ~2046 under Scenario A and two possible terminus collapses in ~2033 and ~2081 under Scenario C (Figs. 42 and 43). Except the modelled accelerations in 1998 and 2003, all the other modelled accelerations are generally short lived, i.e. once the grounding line reached higher ground, the modelled velocities decreased to values similar or smaller than those simulated before the acceleration (Fig. 43). In all the simulations, these modelled episodes of rapid retreat occur at different time intervals but generally at the same location, suggesting that although the ocean can dictate the timing (i.e., warm ocean results in accelerated terminus retreat, while cold ocean results in decelerated terminus retreat), the location will always remain unchanged. Overall, my simulations suggest that JI behaviour represents an ice-dynamical response to local ocean forcings. The degree

of cooling needed to reverse the current retreat trend is tested by forcing the model with 20 years of cooling similar to what occurred between 1970-1990. I found that 0.5 °C of oceanic cooling (Scenario D2) will slow down the retreat – resulting in a much smaller chance of early 21st century collapse. I also found that 0.9 °C of oceanic cooling (Scenario D1) will make JI advance to its 1990 position. However, with current models both cooling scenarios are considered unlikely (IPCC, 2013), and major retreat reoccurs once cooling stops. Thus, at least one major collapse of the terminus should be expected at JI by the end of the 21st century.

In terms of mass, I found that since the end of the LIA until the end of the 21st century JI's mass change was and will remain predominately dynamically controlled (between 74 % and 86 % of the mass change is dynamic in origin). In my model, these dynamic losses are caused by JI's terminus retreat. Usually, an acceleration in dynamic mass change was modelled after the terminus retreated from a basal high through an overdeepening (e.g. Figs. 21, 43 and 45). My simulations further suggested that the change in mass loss at JI is already triggered and that an eminent collapse of the terminus by the end of the century is inevitable. The modelled cumulative mass change for the period 1840-2012 is 1214.5 Gt or 7 Gt a^{-1}, equivalent to 3.4 mm of global sea level rise (Fig. 26). For the 21st century, the best case scenario with regards to future warming (i.e., Scenario A) suggested mass loss estimates that amount to 1860 Gt by the year 2100 or 24 Gt a^{-1} (67 % increase relative to 1840-2012), equivalent of 5.2 mm global sea-level rise (Fig. 45 and Table 3). In the worst case scenario with regards to future warming (Scenario C), expected mass loss of JI amounts to 3275 Gt or 39 Gt a^{-1} by the year 2100 (192 % increase relative to 1840-2012), equivalent of 9.1 mm global sea-level rise (Fig. 45 and Table 3).

9.1 Outlook

Successful prognostic models should replicate both the spatial and the temporal variability of the flow. While in this thesis, I show significant progress in the latter, the model would largely benefit if improvements are made relative to the spatial distribution of the flow. A recent study published by Aschwanden et al. in 2016 shows progress in modelling the shape of the flow. I believe a successful combination of the two studies may prove to be useful.

The second aspect that can be further improved is the calving mechanism. Although, I found that the superposition of the two calving laws used in this thesis performed relatively well for JI, it should only be seen as a compromise solution. To improve prognostic models, a full physically based calving law is needed. However, representing calving front dynamics in 3-D ice sheet models is difficult. The amount of calving laws available for 3-D ice sheet models is very limited and rarely, physically based. A recent calving mechanism developed by Bondzio et al. in 2016

using a level-set method to model calving dynamics could be further implemented in PISM and used to compare, and, why not, improve the performance of the current model.

Thirdly, the present thesis shows that with the right tuning PISM is capable to simulate temporal variability of outlet glacier behaviour with high degree of accuracy. The modelling approach is steady and could be therefore used to model other regions of the GrIS, e.g. Heilheim glacier or the NE Greenland ice stream.

References

Aðalgeirsdóttir, G., A. Aschwanden, C. Khroulev, F. Boberg, R. Mottram, P. Lucas-Picher, and J. H. Christensen. 2014. “Role of model initialisation for projections of 21st century Greenland Ice Sheet mass loss”. J. Glaciol. 60: 782-794. doi: 10.3189/2014JoG13J202.

Ahlstrøm, A. P., P. Gravesen, S. B. Andersen, D. Van As, M. Citterio, R.S. Fausto, S. Nielsen, H. Jepsen, S. Kristensen, E. L. Christensen, L. Stenseng, R. Forsberg, S. Hanson, D. Petersen, and PROMICE Project Team. 2008. “A new program for monitoring the mass loss of the Greenland ice sheet”. Geol. Surv. Den. Green. Bull 15: 61-64.

Albrecht, T., M. Martin, M. Haseloff, R. Winkelmann, and A. Levermann. 2011. “Parameterization for subgrid-scale motion of ice-shelf calving fronts.” The Cryosphere 5: 35–44. doi:10.5194/tc-5-35-2011.

Amundson, J. M., M. Fahnestock, M. Truffer, J. Brown, M. P. Lüthi, and R. J. Motyka. 2010. “Ice mélange dynamics and implications for terminus stability, Jakobshavn Isbræ, Greenland.” J. Geophys. Res. 115: F01005. doi:10.1029/2009JF001405.

Aschwanden, A., E. Bueler, C. Khroulev, and H. Blatter. 2012. “An enthalpy formulation for glaciers and ice sheets.” J. Glaciol. 58(209): 441–457. doi:10.3189/2012JoG11J088.

Aschwanden, A., G. Aðalgeirsdóttir, and C. Khroulev. 2013. “Hindcast to measure ice sheet model sensitivity to initial states.” The Cryosphere 7: 1083–1093. doi:10.5194/tcd-6-5069-2012.

Aschwanden, A., M. A. Fahnestock and M. Truffer. 2016. “Complex Greenland outlet glacier flow captured”. Nat. Commun. 7(10524). doi: 10.1038/ncomms10524.

Bamber, J. L., R. L. Layberry, and S. P. Gogenini. 2001. “A new ice thickness and bed data set for the Greenland Ice Sheet 1: Measurement, data reduction, and errors”. J. Geophys. Res. 106(D24): 33,773-33,780. doi: 10.1029/2001JD900054.

Bamber, J. L., J. A. Griggs, R. T. W. L. Hurkmans, J. A. Dowdeswell, S. P. Gogineni, I. Howat, J. Mouginot, J. Paden, S. Palmer, E. Rignot, and D. Steinhage. 2013. “A new bed elevation dataset for Greenland.” The Cryosphere 7: 499–510. doi:10.5194/tc-7-499-2013.

Beckmann, A., and H. Goosse. 2003. “A parameterization of ice shelf–ocean interaction for climate models.” Ocean Model 5(2): 157–170. doi:10.1016/S1463-5003(02)00019-7.

Bevan, S. L., A. J. Luckman, and T. Murray. 2012. “Glacier dynamics over the last quarter of a century at Helheim, Kangerdlugssuaq and other major Greenland outlet glaciers.” The Cryosphere 6: 923–937. doi:10.5194/tc-6-923-2012.

Bindschadler, R. A., S. Nowicki, A. Abe-Ouchi, A. Aschwanden, H. Choi, J. Fastook, G. Granzow, R. Greve, G. Gutowski, U. Herzfeld, C. Jackson, J. Johnson, C. Khroulev, A. Levermann, W. H. Lipscomb, M. A. Martin, M. Morlighem, B. R. Parizek, D. Pollard, S. F. Price, D. Ren, F. Saito, T. Sato, H. Seddik, H. Seroussi, K. Takahashi, R. Walker, and W. L. Wang. 2013. “Ice-sheet model sensitivities to environmental forcing and their use in projecting future sea level (the SeaRISE project)”. J. Glaciol. 59(214): 195-224. doi: 10.3189/2013JoG12J125.

Blair, B., and M. Hofton. 2012. “IceBridge LVIS L2 Geolocated Ground Elevation and Return Energy Quartiles. Boulder, Colorado USA: NASA Distributed Active Archive Center at the National Snow and Ice Data Center. Digital media.” http://nsidc.org/data/ilvis2.html.

Broeke, M. van den, J. Bamber, J. Ettema, Eric Rignot, E. Schrama, W. J. van de Berg, E. van Meijgaard, I. Velicogna, and B. Wouters. 2009. “Partitioning recent Greenland mass loss.” Science 326(5955): 984–986. doi:10.1126/science.1178176.

Box, J. E. 2013. “Greenland ice sheet mass balance reconstruction. Part II: Surface mass balance (1840-2010)”. J. Climate 26(18): 6974-6989. doi: 10.1175/JCLI-D-12-00518.1.

Box, J. E., and W. Colgan. 2013. “Greenland ice sheet mass balance reconstruction. Part III: Marine ice loss and total mass balance (1840-2010)”. J. Climate 26(18): 6990-7002. doi: 10.1175/JCLI-D-12-00546.1.

Box, J. E., N. Cressie, D. H. Bromwich, J. Jung, M. van den Broeke, J. H. van Angelen, R. R. Forster, C. Miége, E. Mosley-Thompson, B. Vinther, and J. R. McConnell. 2013. ”Greenland ice sheet mass balance reconstruction. Part I: Net snow accumulation (1600-2009)”. J. Climate 26: 3919-3934. doi: 10.1175/JCLI-D-12-0037.

Bueler, E., C. S. Lingle, and J. A. Kallen-Brown. 2007. “Fast computation of a viscoelastic deformable Earth model for ice sheet simulation”. Ann. Glaciol. 46: 97–105. doi: 10.3189/172756407782871567.

Bueler, E., and J. Brown. 2009. “Shallow shelf approximation as a ‘sliding law’ in a thermodynamically coupled ice sheet model.” J. Geophys. Res. 114: F03008. doi:10.1029/2008JF001179.

Christensen, O. B., M. Drews, J. H. Christensen, K. Dethlof, K. Ketelsen, I. Hebestadt, and A. Rinke. 2006. ”The HIRHAM Regional Climate Model Version 5. Tech. Report DMI, Copenhagen”. pages 06-17.

Chylek, P., M. K. Dubey, and G. Lesins. 2006. “Greenland warming of 1920–1930 and 1995–2005”. Geophys. Res. Lett. 33: L11707. doi:10.1029/2006GL026510.

Clarke, L., J. Edmonds, H. Jacoby, H. Pitcher, J. Reilly, R. Richels. 2007. “Scenarios of Greenhouse Gas Emissions and Atmospheric Concentrations. Sub-report 2.1A of Synthesis and Assessment Product 2.1 by the U.S. Climate Change Science Program and the Subcommittee on Global Change Research”. Department of Energy, Office of Biological & Environmental Research, Washington, 7 DC., USA, 154 pp.

Csatho, B., T. Schenk, C. J. Van Der Veen and W. B. Krabill. 2008. “Intermittent thinning of Jakobshavn Isbræ, West Greenland, since the Little Ice Age.” J. Glaciol. 54(184): 131–144. doi: 10.3189/002214308784409035.

Cuffey, K. M. and W. S. B. Paterson. 2010. ”The Physics of Glaciers”, Elsevier, 4th Edn., ISBN 9780123694614.

Dee, D. P., S. M. Uppala, A. J. Simmons, P. Berrisford, P. Poli, S. Kobayashi, U. Andrae, M. A. Balmaseda, G. Balsamo, P. Bauer, P. Bechtold, A. C. M. Beljaars, L. van de Berg, J. Bidlot, N. Bormann, C. Delsol, R. Dragani, M. Fuentes, A. J. Geer, L. Haimberger, S. B. Healy, H. Hersbach, E. V. Hólm, L. Isaksen, P. Kållberg, M. Köhler, M. Matricardi, A. P. McNally, B. M. Monge-Sanz, J.-J. Morcrette, B.-K. Park, C. Peubey, P. de Rosnay, C. Tavolato, J.-N. Thépaut, and F. Vitart. 2011. “The ERA-Interim reanalysis: Configuration and performance of the data assimilation system”. Q. J. R. Meteorol. Soc. 137(656): 553-597. doi: 10.1002/qj.828.

de Juan, J., P. Elósegui, M. Nettles, T.B. Larsen, J.L. Davis, G.S. Hamilto, L.A. Stearns, M. L. Anderson, G. Ekström, L. Stenseng, S. A. Khan, R. Forsberg. 2010. “Sudden increase in tidal response linked to calving and acceleration at a large Greenland outlet glacier”. Geophys. Res. Lett. 37: L12501. doi:10.1029/2010GL043289.

Della-Giustina, D. N. 2011. “Regional modelling of Greenland’s outlet glaciers with the Parallel ice sheet model”. MSc thesis. University of Alaska Fairbanks.

Dziewonski, A. M., and D. L. Anderson. 1981. “Preliminary reference Earth model.” Phys. Earth Planet. Inter. 25: 297–356. doi:10.1016/0031-9201(81)90046-7.

Echelmeyer, K. A., W. D. Harrison, C. Larson, and J. E. Mitchell. 1994. “The role of the margins in the dynamics of an active ice stream”. J. Glaciol. 40(136): 527–538.

Eerola, K. 2006. “About the performance of the Hirlam version 7.0”. Tech. Rep. 51, Article 14. Technical report DMI, Copenhagen.

Enderlin, E. M., I. M. Howat, and A. Vieli. 2013. “High sensitivity of tidewater outlet glacier dynamics to shape.” The Cryosphere 7: 1007–1015. doi: 10.5194/tc-7-1007-2013.

Enderlin, E. M., I. M. Howat, S. Jeong, M. J. Noh, J. H. van Angelen, and M. R. van den Broeke. 2014. “An improved mass budget for the Greenland ice sheet.” Geophys. Res. Lett. 41: 866–872. doi:10.1002/2013GL059010.

Ettema, J., M. R. van den Broeke, E. van Meijgaard, W. J. van de Berg, J. L. Bamber, J. E. Box, and R. C. Bales. 2009. ”Higher surface mass balance of the Greenland ice sheet revealed by high-resolution climate modeling”. Geophys. Res. Lett. 36: L12501. doi: 10.1029/2009GL038110.

Ettema, J., M. R. van den Broeke, E. van Meijgaard, W. J. van de Berg, J. E. Box, and K. Stefen. 2010. ”Climate of the Greenland ice sheet using a high resolution climate model - Part 1: Evaluation”. The Cryosphere 4: 511-527. doi:10.5194/tc-4-511-2010.

Ewert, H., A. Groh, and R. Dietrich. 2012. “Volume and mass changes of the Greenland ice sheet inferred from ICESat and GRACE.” J. Geodyn. 59-60: 111–23. doi:10.1016/j.jog.2011.06.003.

Feldmann, J., T. Albrecht, C. Khroulev, F. Pattyn, and A. Levermann. 2014. “Resolution-dependent performance of grounding line motion in a shallow model compared with a full-Stokes model according to the MISMIP3d intercomparison.” J. Glaciol. 60(220): 353–360. doi:10.3189/2014JoG13J093.

Gladish, C. V., D. M. Holland, and C. M. Lee. 2015a. “Oceanic boundary conditions for Jakobshavn Glacier. Part II: Provenance and sources of variability of Disko Bay and Ilulissat icefjord waters, 1990–2011.” J. Phys. Oceanogr. 45: 33–63. doi: 10.1175/JPO-D-14-0045.1.

Gladish, C. V., D. M. Holland, A. Rosing-Asvid, J. W. Behrens, and J. Boje. 2015b. “Oceanic boundary conditions for Jakobshavn Glacier. Part I: Variability and renewal of Ilulissat icefjord waters, 2001–2014.” J. Phys. Oceanogr. 45: 3–32. doi: 10.1175/JPO-D-14-0044.1.

Gladstone, R. M., A. J. Payne, and S. L. Cornford. 2010. “Parameterising the grounding line in flow-line ice sheet models.” The Cryosphere 4: 605–19. doi:10.5194/tc-4-605-2010.

Glen, J. 1952. “Experiments on the deformation of ice”. J. Glaciol. 2: 111–114.

Greve, R., and H. Blatter. 2009. “Dynamics of Ice Sheets and Glaciers”. Springer. ISBN 10.1007/978-3-642-03415-2.

Hanna, E., X. Fettweis, S. Mernild, J. Cappelen, M. Ribergaard, C. Shuman, K. Steffen, L. Wood, and T. Mote. 2014. “Atmospheric and oceanic climate forcing of the exceptional Greenland ice sheet surface melt in summer 2012.” Int. J. Climatol. 34(4): 1022–1037. doi:10.1002/joc.3743.

Helm, V., A. Humbert, and H. Miller. 2014. “Elevation and elevation change of Greenland and Antarctica derived from CryoSat-2”. The Cryosphere 8(4): 1539-1559 . doi: 10.5194/tc-8-1539-2014.

Holland, D. M., R. H. Thomas, B. de Young, M. H. Ribergaard, and B. Lyberth. 2008. “Acceleration of Jakobshavn Isbræ Triggered by Warm Subsurface Ocean Waters.” Nat. Geosci. 1: 659–664. doi:10.1038/ngeo316.

Howat I. M., Y. Ahn, I. Joughin, M. R. van den Broeke, J. T. M. Lenaerts, and B. Smith. 2011. “Mass balance of Greenland's three largest outlet glaciers, 2000–2010.” Geophys. Res. Lett. 38(12): L12501. doi: 10.1029/2011GL047565.

Hutter K. 1983. “Theoretical Glaciology: Material Science of Ice and the Mechanics of Glaciers and Ice Sheets.” D. Reidel Publishing Co. Tokyo, Terra Scientific Publishing Co. xxxii, 510 p.

IPCC. 2013. “Climate Change 2013: The Physical Science Basis. Contribution of Working Group I to the Fifth Assessment Report of the Intergovernmental Panel on Climate Change.” Cambridge University Press, Cambridge, United Kingdom and New York, NY, USA: 1535 pp. doi:10.1017/CBO9781107415324.

Jakobsson, M., L. Mayer, B. Coakley, J. A. Dowdeswell, S. Forbes, B. Fridman, H. Hodnesdal, R. Noormets, R. Pedersen, M. Rebesco, H. W. Schenke, Y. Zarayskaya, D. Accettella, A. Armstrong, R. M. Anderson, P. Bienhoff, A. Camerlenghi, I. Church, M. Edwards, J. V. Gardner, J. K. Hall, B. Hell, O. Hestvik, Y. Kristoffersen, C. Marcussen, R. Mohammad, D. Mosher, S. V. Nghiem, M. T. Pedrosa, P. G. Travaglini, and P. Weatherall. 2012. ”The International Bathymetric Chart of the Arctic Ocean (IBCAO) Version 3.0.” Geophys. Res. Lett. 39: L12609. doi:10.1029/2012gl052219.

Jamieson, S. S. R., A. Vieli, S. J. Livingstone, C. Ó Cofaigh, C. Stokes, C.-D. Hillenbrand, and J. A. Dowdeswell. 2012. "Icestream stability on a reverse bed slope". Nat. Geosci. 5: 799–802. doi:10.1038/NGEO1600.

Jones, P. W. 1999. "First- and Second-Order Conservative Remapping Schemes for Grids in Spherical Coordinates". Mon. Weather Rev. 127(9): 2204–2210. doi: 10.1175/1520-0493(1999)127<2204:FASOCR>2.0.CO;2.

Joughin, I., W. Abdalati, and M. Fahnestock. 2004. "Large fluctuations in speed on Greenland's Jakobshavn Isbræ glacier." Nature 432: 608–610. doi:10.1038/nature03130.

Joughin, I., I. M. Howat, M. Fahnestock, B. Smith, W. Krabill, R. B. Alley, H. Stern, and M. Truffer. 2008. "Continued Evolution of Jakobshavn Isbrae Following Its Rapid Speedup." J. Geophys. Res. 113: F04006. doi:10.1029/2008JF001023.

Joughin, I, B. E. Smith, I. M. Howat, T. Scambos, and T. Moon. 2010. "Greenland Flow Variability from Ice-Sheet-Wide Velocity Mapping". J. Glaciol. 56(197): 415-430. doi:10.3189/002214310792447734.

Joughin, I., I. Howat, B. Smith, and T. Scambos. 2011. "MEaSUREs Greenland Ice Velocity: Selected Glacier Site Velocity Maps from InSAR". Boulder, Colorado, USA: NASA DAAC at the National Snow and Ice Data Center. doi:10.5067/MEASURES/CRYOSPHERE/nsidc-0481.001.

Joughin, I., B. E. Smith, I. M. Howat, D. Floricioiu, R. B. Alley, M. Truffer, and M. Fahnestock. 2012. "Seasonal to decadal scale variations in the surface velocity of Jakobshavn Isbræ, Greenland: Observation and model-based analysis." J. Geophys. Res. 117: F02030. doi:10.1029/2011JF002110.

Joughin, I., S. B. Das, G. E. Flowers, M. D. Behn, R. B. Alley, M. A. King, B. E. Smith, J. L. Bamber, M. R. van den Broeke, and J. H. van Angelen. 2013. "Influence of ice-sheet geometry and supraglacial lakes on seasonal ice-flow variability." The Cryosphere 7: 1185-1192. doi:10.5194/tc-7-1185-2013.

Joughin, I., B. E. Smith, D. E. Shean, and D. Floricioiu. 2014. "Brief Communication: Further summer speedup of Jakobshavn Isbræ." The Cryosphere 8: 209–214. doi:10.5194/tc-8-209-2014.

Keegan, K. M., R.M. Albert, J. R. McConnell and I. Baker. 2014. "Climate change and forest fires synergistically drive widespread melt events of the Greenland Ice Sheet." P. Natl. Acad. Sci. 111(22): 7964–7967. doi: 10.1073/pnas.1405397111.

Khan, S. A., L. Liu, J. Wahr, I. Howat, I. Joughin, T. van Dam, and K. Fleming. 2010. "GPS measurements of crustal uplift near Jakobshavn Isbræ due to glacial ice mass loss." J. Geophys. Res. 115: B09405. doi:10.1029/2010JB007490.

Khan, S. A., K. H. Kjær, N. J. Korsgaard, J. Wahr, I. R. Joughin, L. H. Timm, J. L. Bamber, et al. 2013. "Recurring dynamically induced thinning during 1985 to 2010 on Upernavik Isstrøm, West Greenland." J. Geophys. Res.118: 111–21. doi:10.1029/2012JF002481.

Khan, S. A., K. H. Kjær, M. Bevis, J. L. Bamber, J. Wahr, K. K. Kjeldsen, A. A. Bjørk, N. J. Korsgaard, L. A. Stearns, M. R. van den Broeke, L. Liu, N. K. Larsen, and I. S. Muresan. 2014. "Sustained Mass Loss of the Northeast Greenland Ice Sheet Triggered by Regional Warming." Nat. Clim. Change 4: 292–299. doi:10.1038/nclimate2161.

Khan, S. A. , K. K. Kjeldsen, K. H. Kjær, S. Bevan, A. Luckman, A. Aschwanden, A. A. Bjørk, and N. J. Korsgaard. 2014. "Glacier dynamics at Helheim and Kangerdlugssuaq glaciers, southeast Greenland, since the Little Ice Age". The Cryosphere 8: 1497–1507. doi:10.5194/tc-8-1497-2014.

Khan, S. A., A. Aschwanden, A. A. Bjørk, J. Wahr, K. K. Kjeldsen, and K. H. Kjær. 2015. "Greenland ice sheet mass balance: a review." Rep. Prog. Phys. 78(4). doi: 10.1088/0034-4885/78/4/046801.

Kimura, S., P. R. Holland, A. Jenkins, and M. Piggott. 2014. "The effect of meltwater plumes on the melting of a vertical glacier face." J. Phys. Oceanogr. 44: 3099-3117. doi: 10.1175/JPO-D-13-0219.1.

Krabill, W., W. Abdalati, E. Frederick, S. Manizade, C. Martin, J. Sonntag, R. Swift, R. Thomas, W. Wright, and J. Yungel. 2000. "Greenland Ice Sheet: High-Elevation Balance and Peripheral Thinning." Science 289: 428–430. doi:10.1126/science.289.5478.428.

Krabill, W., E. Hanna, P. Huybrechts, W. Abdalati, J. Cappelen, B. Csatho, E. Frederick, S. Manizade, C. Martin, J. Sonntag, R. Swift, R. Thomas, and J. Yungel. 2004. "Greenland Ice Sheet: Increased coastal thinning", Geophys. Res. Lett. 31: L24402. doi:10.1029/2004GL021533.

Krabill, W. B. 2014. "IceBridge ATM L2 Icessn Elevation, Slope, and Roughness, [1993-2014]. Boulder, Colorado USA: NASA Distributed Active Archive Center at the National Snow and Ice Data Center. Digital media. Updated 2014." http://nsidc.org/data/ilatm2.html.

Kuipers Munneke, P., S. R. M. Ligtenberg, B. P. Y Noel, I. M. Howat, J. E. Box, E. Mosley-Thompson, J. R. McConnell, et al. 2015. "Elevation change of the Greenland ice sheet due to surface mass balance and firn processes, 1960–2013." TCD 9: 3541–80. doi:10.5194/tcd-9-3541-2015.

Langen, P. L., R. H. Mottram, J. H. Christensen, F. Boberg, C. B. Rodehacke, M. Stendel, D. van As, A. P. Ahlstrøm, J. Mortensen, S. Rysgaard, D. Petersen, K. H. Svendsen, G. Aðalgeirsdóttir, J. Cappelen. 2015. "Quantifying energy and mass fluxes controlling Godthåbsfjord freshwater input in a 5 km simulation (1991-2012)". J. Climate 28: 3694–3713. doi: 10.1175/JCLI-D-14-00271.1

Larour, E., H. Seroussi, M. Morlighem, and E. Rignot. 2012. "Continental scale, high order, high spatial resolution, ice sheet modeling using the Ice Sheet System Model (ISSM)." J. Geophys. Res.-Earth 117: F01022. doi:10.1029/2011JF002140.

Levermann, A., T. Albrecht, R. Winkelmann, M. A. Martin, M. Haseloff, and I. Joughin. 2012. "Kinematic first-order calving law implies potential for abrupt ice-shelf retreat." The Cryosphere 6: 273–286. doi:10.5194/tc-6-273-2012.

Liepert, B. G.. 2002. "Observed reductions of surface solar radiation at sites in the United States and worldwide from 1961 to 1990". Geophys. Res. Lett. 29(10): F1421. doi:10.1029/2002GL014910.

Lingle, C. S. and J. A. Clark. 1985. "A numerical model of interactions between a marine ice sheet and the solid earth: Application to a West Antarctic ice stream". J. Geophys. Res., 90(C1):1100–1114.

Luckman, A., and T. Murray. 2005. "Seasonal variation in velocity before retreat of Jakobshavn Isbræ, Greenland." J. Geophys. Res. Letters 32: L08501. doi:10.1029/2005GL022519.

MacAyeal, D. R., T. A. Scambos, C. L. Hulbe and M. A. Fahnestock. 2003. "Catastrophic iceshelf break-up by an ice-shelf-fragment-capsize mechanism." J. Glaciol. 49(164): 22-36.

Martin, M. A., R. Winkelmann, M. Haseloff, T. Albrecht, E. Bueler, C. Khroulev, and A. Levermann. 2011. "The Potsdam Parallel Ice Sheet Model (PISM-PIK), Part II: Dynamical equilibrium simulation of the Antarctic Ice Sheet." The Cryosphere 5: 727–740. doi:10.5194/tc-5-727-2011.

Mengel, M., and A. Levermann. 2014. "Ice plug prevents irreversible discharge from East Antarctica." Nat. Clim. Change 4: 451–455. doi:10.1038/nclimate2226.

MET. 2015. "Met Office Hadley Centre observations datasets." Digital media. http://www.metoffice.gov.uk/hadobs/hadisst/data/download.html.

Moon, T., I. Joughin, B. Smith, and I. Howat. 2012. "21st-Century evolution of Greenland outlet glacier velocities." Science 336: 576–578. doi:10.1126/science.1219985.

Morlighem, M., E. Rignot, J. Mouginot, H. Seroussi and E. Larour. 2014. "Deeply incised submarine glacial valleys beneath the Greenland Ice Sheet", Nat. Geosci. 7: 418-422. doi:10.1038/ngeo2167.

Motyka, R. J., M. Truffer, M. Fahnestock, J. Mortensen, S. Rysgaard, and I. Howat. 2011. "Submarine melting of the 1985 Jakobshavn Isbræ floating tongue and the triggering of the current retreat." J. Geophys. Res. 116: F01007. doi:10.1029/2009JF001632.

Muresan, I. S., S. A. Khan, A. Aschwanden, C. Khroulev, T. Van Dam, J. Bamber, M. V. D. Broeke, B. Wouters, P. Kuipers Munneke, and K. H. Kjær. 2016. "Modelled glacier dynamics over the last quarter of a century at Jakobshavn Isbræ". The Cryosphere 10(2): 597-611. doi: 10.5194/tc-10-597-2016.

Nghiem, S. V., D. K. Hall, T. L. Mote, M. Tedesco, M. R. Albert, K. Keegan, C. A. Shuman, N. E. DiGirolamo, and G. Neumann. 2012. "The extreme melt across the Greenland ice sheet in 2012." Geophys. Res. Lett. 39: L20502. doi: 10.1029/2012GL053611.

Nick, F. M., A. Vieli, M. L. Andersen, I. Joughin, A. Payne, T. L. Edwards, F. Pattyn, and R. S. van de Wal. 2013. "Future sea-level rise from Greenland's main outlet glaciers in a warming climate." Nature 497: 235–238. doi:10.1038/nature12068.

Nick, F. M., A. Vieli, I. M. Howat, and I. Joughin. 2009. "Large-Scale Changes in Greenland Outlet Glacier Dynamics Triggered at the Terminus." Nat. Geosci. 2: 110–114. doi:10.1038/ngeo394.

Nielsen, K., S. A. Khan, G. Spada, J. Wahr, M. Bevis, L. Liu, and T. van Dam. 2013. "Vertical and horizontal surface displacements near Jakobshavn Isbræ driven by melt-induced and dynamic ice loss." J. Geophys. Res.-Sol. Ea. 118: 1837–1844. doi:10.1002/jgrb.50145.

Noël, B., W. J. van de Berg, E. van Meijgaard, P. Kuipers Munneke, R. S. W. van de Wal, and M. R. van den Broeke. 2015. "Summer snowfall on the Greenland Ice Sheet: a study with the updated regional climate model RACMO2.3." The Cryosphere Discussion 9: 1177-1208. doi: 10.5194/tcd-9-1177-2015.

NSIDC. 2015. "2014 melt season in review." National Snow and Ice Data Center (NSIDC). Accessed July 09, 2015. http://nsidc.org/greenland-today/2015/01/2014-melt-season-in-review/.

Nye, J. F. 1953. "The Flow Law of Ice from Measurements in Glacier Tunnels, Laboratory Experiments and the Jungfraufirn Borehole Experiment". Proc. R. Soc. London. Ser. A, 219, 477–489.

Parizek, B. R., and R. T. Walker. 2010. “Implications of initial conditions and ice–ocean coupling for grounding-line evolution.” Earth Planet. Sci. Lett. 300: 351–358. doi:10.1016/j.epsl.2010.10.016.

Paterson, W. and K. Cuffey. 2010. “The Physics of glaciers”. 3rd Edition. Volume 1994. ISBN 978-0750647427.

Pattyn, F., C. Schoof, L. Perichon, R. C. A. Hindmarsh, E. Bueler, B. de Fleurian, G. Durand, et al. 2012. “Results of the Marine Ice Sheet Model Intercomparison Project, MISMIP.” The Cryosphere 6: 573–588. doi:10.5194/tc-6-573-2012.

Pattyn, F., L. Perichon, G. Durand, L. Favier, O. Gagliardini, R. Hindmarsh, T. Zwinger, T. Albrecht, S. Cornford, D. Docquier, J. J. Fust, D. Goldberg, G. H. Gudmundsson, A. H. Humbert, M. Hütten, P. Huybrechts, G. Jouvet, T. Kleiner, E. Larour, D. Martin, M. Morlighem, A. J. Payne, D. Pollard, M. Ruckamp, O. Rybak, H. Seroussi, M. Thoma, and N. Wilkens. 2010. “Grounding-line migration in plan-view marine ice-sheet models: results of the ice2sea MISMIP3d intercomparison“. J. Glaciol. 59: 410–422. doi: 10.3189/2013JoG12J12910.3189/2013JoG12J129.

Peltier, W. R. 2004. “Global glacial isostasy and the surface of the ice-age Earth: The ICE-5G (VM2) model and GRACE.” Annu. Rev. Earth Planet. Sci. 32: 111–49. doi:10.1146/annurev.earth.32.082503.144359.

Petrov, L., and J. P. Boy. 2004. “Study of the atmospheric pressure loading signal in very long baseline interferometry observations.” J. Geophys. Res. 109: B03405. doi:10.1029/2003jb002500.

Pfeffer, W. T., T. H. Illangasekare and M. F. Meier. 1990. ”Analysis and modeling of melt-water refreezing in dry snow”. J. Glaciol. 36(123): 238-246.

Pfeffer, W. T., M. F. Meier, and T. H. Illangasekare. 1991. “Rentention of Greenland runoff by refreezing: implications for projected future sea level change”. J. Geophys. Res. 6(C12): 22117-22124.

Pollard, D., R. M. DeConto, and R. B. Alley. 2015. “Potential Antarctic Ice Sheet retreat driven by hydrofracturing and ice cliff failure.” Earth Planet. Sci. Lett. 412: 112–121. doi: 10.1016/j.epsl.2014.12.035.

Price, S. F., A. J. Payne, I. M. Howat, and B. E. Smith. 2011. “Committed sea-level rise for the next century from Greenland ice sheet dynamics during the past decade.” P. Natl. Acad. Sci. USA 108: 8978–8983. doi:10.1073/pnas.1017313108.

Riahi, K., A. Gruebler, and N. Nakicenovic. 2007. ”Scenarios of long-term socio-economic and environmental development under climate stabilization.” Technol. Forecast. Soc. 74(7): 887-935.

Rayner, N. A., D. E. Parker, E. B. Horton, C. K. Folland, L. V. Alexander, D. P. Rowell, E. C. Kent, and A. Kaplan. 2003. ”Global analyses of sea surface temperature, sea ice, and night marine air temperature since the late nineteenth century”. J. Geophys. Res. 108(D14): 4407. doi:10.1029/2002JD002670.

Rignot, E., J. L. Bamber, M. R. van den Broeke, C. Davis, Y. Li, W. J. van de Berg, and E. van Meijgaard. 2008. “Recent Antarctic ice mass loss from radar interferometry and regional climate modeling.” Nat. Geosci. 1: 106–110. doi:10.1038/ngeo102.

Roeckner, E., G. Bäuml, L. Bonaventura, R. Brokopf, M. Esch, M. Giorgetta, S. Hagemann, I. Kirchner, L. Kornblueh, E. Manzini, A. Rhodin, U. Schlese, U. Schulzweida, and A. Tompkins. 2003. “The atmospheric general circulation model ECHAM5. Part I: Model description.” Tech Rep. 349. Technical report Max Planck Institute for Meteorology, Hamburg.

Rogozhina, I., Z. Martinec, J. M. Hagedoorn, M. Thomas, and K. Fleming. 2011. “On the long-term memory of the Greenland Ice Sheet”. J. Geophys. Res. 116: F01011. doi: 10.1029/2010JF001787.

Seroussi, H., H. B. Dhia, M. Morlighem, E. Larour, E. Rignot, and D. Aubry. 2012. “Coupling ice flow models of varying orders of complexity with the Tiling method.” J. Glaciol. 58: 776–786. doi:10.3189/2012JoG11J195.

Schlesinger, M. E. 1994. “An oscillation in the global climate system of period 65-70 years”. Nature 367: 723–726. doi:10.1038/367723a0.

Schoof, C. 2007. “Ice sheet grounding line dynamics: steady states, stability, and hysteresis.” J. Geophys. Res. 112 (F03S28). doi:10.1029/2006JF000664.

Schoof, C. and R. Hindmarsh. 2010. “Thin-film flows with wall slip: an asymptotic analysis of higher order glacier flow models”. Quart. J. Mech. Appl. Math. 63:73–114. doi:10.1093/qjmam/hbp025.

Shapiro, N. M., and M. H. Ritzwoller. 2004. “Inferring surface heat flux distributions guided by a global seismic model: particular application to Antarctica.” Earth Planet. Sci. Lett. 223: 213–224. doi: 10.1016/j.epsl.2004.04.011.

Shepherd, A., E. R. Ivins, A. Geruo, V. R. Barletta, M. J. Bentley, S. Bettadpur, K. H. Briggs, D. H. Bromwich, R. Forsberg, N. Galin, M. Horwath, S. Jacobs, I. Joughin, M. A. King, J. T. M. Lenaerts, J. Li, S. R. M. Ligtenberg, A. Luckman,

S. B. Luthcke, M. McMillan, R. Meister, G. Milne, J. Mouginot, A. Muir, J. P. Nicolas, J. Paden, A. J. Payne, H. Pritchard, E. Rignot, H. Rott, L. S. Sørensen, T. A. Scambos, B. Scheuchl, E. J. O. Schrama, B. Smith, A. V. Sundal, J. H. van Angelen, J. H., W. J. van de Berg, M. R. van den Broeke, D. G. Vaughan, I. Velicogna, J. Wahr, P. L. Whitehouse, D. J. Wingham, D. Yi, D. Young, and H. J. Zwally. 2012. "A reconciled estimate of ice-sheet mass balance". Science, 338: 1183–1189. doi:10.1126/science.1228102.

Slater, D. A., P. W. Nienow, T. R. Cowton, D. N. Goldberg, and A. J. Sole. 2015. "Effect of near-terminus subglacial hydrology on tidewater glacier submarine melt rates." Geophys. Res. Lett. 42: 2861-2868. doi: 10.1002/2014GL062494.

Smith, B. E., H. A. Fricker, I. R. Joughin, and S. Tulaczyk. 2009. "An inventory of active subglacial lakes in Antarctica detected by ICESat (2003-2008)." J. Glaciol. 55: 573–95. doi:10.3189/002214309789470879.

Smith, S. J. and T.M.L. Wigley, 2006. Multi-Gas Forcing Stabilization with the MiniCAM. Energy Journal (Special Issue #3). pp 373-391.

Sohn, H. G., K. C. Jezek, and C. J. van der Veen. 1998. "Jakobshavn Glacier, west Greenland: 30 years of spaceborne observations." Geophys. Res. Lett. 25(14): 2699-2702. doi: 10.1029/98GL01973.

Stanley, S. J., A. Jenkins, C. F. Giulivi and P. Dutrieux. 2011. "Stronger ocean circulation and increased melting under Pine Island Glacier ice shelf." Nat. Geosci. 4: 519–523. doi: 10.1038/ngeo1188.

Tedesco, M., X. Fettweis, T. Mote, J. Wahr, P. Alexander, J. E. Box, and B. Wouters. 2013. "Evidence and analysis of 2012 Greenland records from spaceborne observations, a regional climate model and reanalysis data." The Cryosphere 7: 615-630. doi: 10.5194/tc-7-615-2013

The PISM Authors. 2014. "PISM, a Parallel Ice Sheet Model. User's Manual."Accessed June 15, 2015. http://www.pismdocs.org/.

Thomas, H. R., W. Abdalati, E. Frederick, W. B. Krabill, S. Manizade, and K. Steffen. 2003. "Investigation of surface melting and dynamic thinning on Jakobshavn Isbræ." J. Glaciol. 49(165): 231–239. doi:10.3189/172756503781830764.

Thomas, R. H. 2004. "Force-perturbation analysis of recent thinning and acceleration of Jakobshavn Isbrae, Greenland." J. Glaciol. 50(168): 57–66. doi: 10.3189/172756504781830321.

Van der Veen, C. J., J. C. Plummer, and L. A. Stearns. 2011. "Controls on the recent speed-up of Jakobshavn Isbræ, West Greenland." J. Glaciol. 57(204): 770–782.

Vieli, A., and F. M. Nick. 2011. "Understanding and Modeling Rapid Dynamic Changes of Tidewater Outlet Glaciers: Issues and Implications." Surv. Geophys. 32: 437–458. doi: 10.1007/s10712-011-9132-4.

Weis M., R. Greve, and K. Hutter. 1999. "Theory of shallow ice shelves". Contin. Mech. Thermodyn. 11(1): 15–50.

Weidick, A. 1968. "Observations on some Holocene glacier fluctuations in West Greenland". Bull. Grønl. Geol. Unders. 73.

Weidick, A. 1969. "Investigations of the Holocene deposits around Jakobshavn Isbrae, West Greenland". In Péwé, T.L., ed. The periglacial environment: past and present. Montréal, McGill–Queens University Press: 249–262.

Winkelmann, R., M. A. Martin, M. Haseloff, T. Albrecht, E. Bueler, C. Khroulev, and A. Levermann. 2011. "The Potsdam Parallel Ice Sheet Model (PISM-PIK) Part 1: Model description." The Cryosphere 5: 715–726. doi:10.5194/tc-5-715-2011.

Wouters, B., A. Martin-Español, V. Helm, T. Flament, J. M. Van Wessem, S. R. M. Ligtenberg, M. R. Van Den Broeke and J. L. Bamber. 2015. "Dynamic thinning of glaciers on the Southern Antarctic Peninsula". Science 348(6237): 899-903. doi: 10.1126/science.aaa5727.

Yin, J., J. T. Overpeck, S. M. Griffies, A. Hu, J. L. Russell and R. J. Stouffer. 2011. "Different magnitudes of projected subsurface ocean warming around Greenland and Antarctica". Nat. Geo. 4: 524-528. doi:10.1038/ngeo1189.

Zwally, H. J., R. Schutz, C. Bentley, J. Bufton, T. Herring, J. Minster, J. Spinhirne, and R. Thomas. 2012. "GLAS/ICESat L2 Antarctic and Greenland Ice Sheet Altimetry Data V031. Boulder, Colorado: NASA Distributed Active Archive Center at the National Snow and Ice Data Center. Digital media." Nat. Geo. 4: 524–528. doi: 10.1038/ngeo1189.

List of figures

List of tables

Appendix A

A1. List of symbols

Table A1: List of symbols

Symbol	Description	SI units
A	ice softness	$Pa^{-3}\ s^{-1}$
A_c	ice hardness coefficient cold	$Pa^{-3}\ s^{-1}$
A_w	ice hardness coefficient warm	$Pa^{-3}\ s^{-1}$
$\bar{B}$	vertically averaged ice hardness	$Pa\ s^{1/3}$
b	bedrock elevation	m
c	calving rate	$m\ s^{-1}$
c_0	the till cohesion	kPa
E_{SIA}	enhancement factor for the SIA	-
E_{SSA}	enhancement factor for the SSA	-
F_{melt}	a sub-shelf melt model parameter	-
f	flow law water fraction coeff.	-
g	acceleration due to gravity	$m\ s^{-2}$
h	upper surface elevation of ice	m
H	ice thickness	m
K	proportionality constant for eigen calving	m s
M	ice equivalent surface mass balance	$m\ s^{-1}$
n	Glen flow law exponent	-
N_{till}	effective pressure of the till	$N\ m^{-2}$
p	pressure	Pa
P_0	ice overburden pressure	$N\ m^{-2}$
pw	pore water pressure	$N\ m^{-2}$
$\boldsymbol{Q}$	horizontal ice flux	$m^2\ s^{-1}$
Q_c	flow law activation energy cold	$J\ mol^{-1}K^{-1}$
$\boldsymbol{Q_{heat}}$	mass flux from shelf to ocean	-
Q_ω	flow law activation energy warm	$J\ mol^{-1}K^{-1}$
q	exponent of the pseudo-plastic basal resistance model	
R	ideal gas constant	$J\ mol^{-1}K^{-1}$
S	ice equivalent basal mass balance	$m\ s^{-1}$
S_0	ocean water salinity	psu
T	ice temperature	K
T_c	flow law critical temperature	K
T_f	virtual temperature	K
T_{pa}	pressure-adjusted temperature	K
T_{pm}	ice temperature at the base of the shelf	K
T_0	ocean water temperature	K
$\boldsymbol{u}$	the model sliding velocity	$m\ s^{-1}$
$\boldsymbol{v}_{SIA}$	SIA velocity of ice	$m\ s^{-1}$
$\boldsymbol{v}_{SSA}$	SSA velocity of ice	$m\ s^{-1}$
W_{till}	the effective thickness of water in the till	m
z_b	elevation at the base of the ice shelf	m
δ_{ij}	Kronecker delta	-
(x, y)	horizontal dimensions	m

∇	2-D gradient operator	m^{-1}
βcc	the Clausius-Clapeyron gradient	$K\ m^{-1}$
ε_{ij}	component of the strain rate tensor	s^{-1}
ν	viscosity	Pa s
$\bar{\nu}$	vertical-averaged viscosity	Pa s
ρ_i	density of ice	$kg\ m^{-3}$
ρ_o	density of ocean water	$kg\ m^{-3}$
z	vertical dimension (positive upwards)	m
σ_{ij}	full Cauchy stress tensor	$N\ m^{-2}$
τ_b	basal shear stress	$N\ m^{-2}$
τ_c	yield stress	$N\ m^{-2}$
τ_{ij}	component of the deviatoric stress tensor;	$N\ m^{-2}$
ϕ	till friction angle	degrees

A2. Additional figures

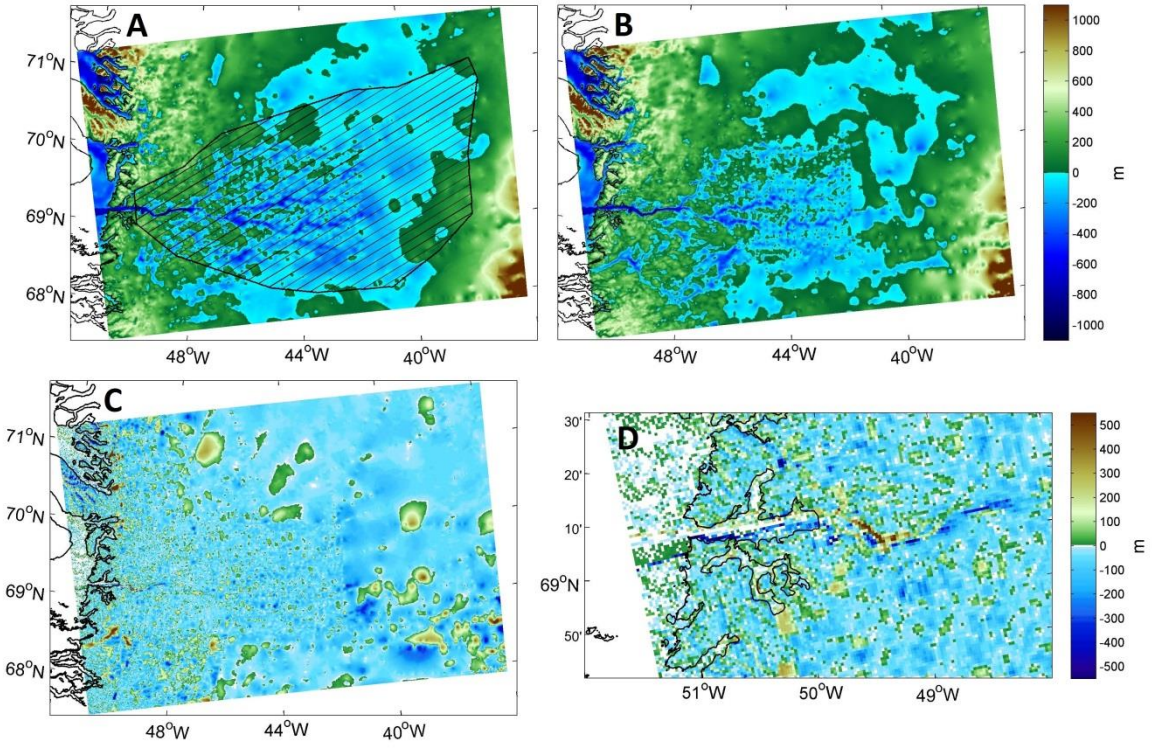

Figure A1: (A) Bed topography from Bamber et al. (2013). (B) Bed topography from Morlighem et al. (2014). (C) Difference in meters between the two bed topography sets (A-B) for the entire computational domain. (D) Difference in meters between the two bed topography sets (A-B) for the terminus region.

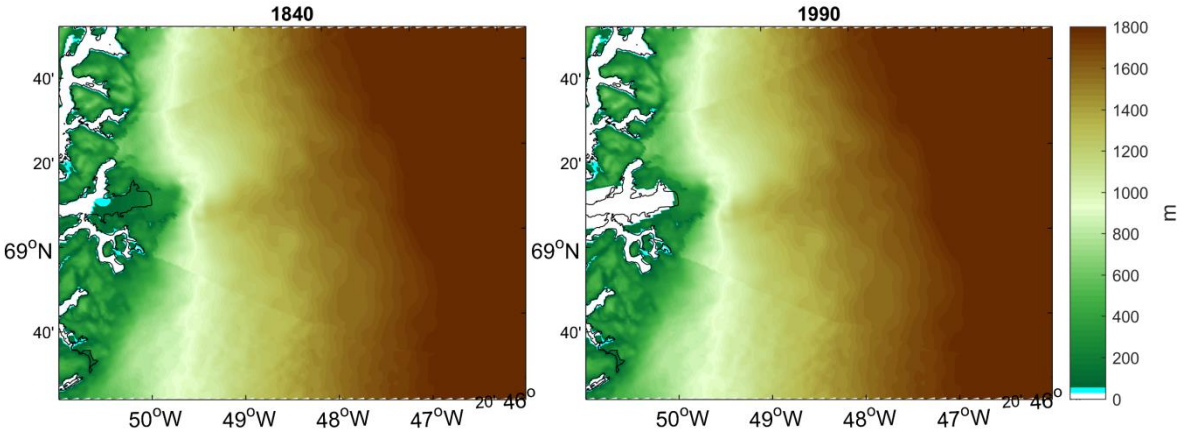

Figure A 2: Reconstructed surface elevation (see Sect. 2.3) for 1840 (left) and 1990 (right) .

Appendix B. Study 1

B1. Parameters

Table A2: Ice sheet model parameters that have been altered from the default PISM values (The PISM Authors, 2014) during the paleo spin-up.

Symbol	Description	Value
E_{SIA}	the flow enhancement factor for SIA	3
q	the exponent of the pseudo-plastic basal resistance model	0.25
ϕ	the till fraction angle	°
ϕ_{min}	for bed elevations lower than 300 m below sea level [°]	5
ϕ_{max}	for bed elevations higher than 700 m above sea level [°]	30
α	pore water pressure fraction	0.98

To obtain an initial state with temperature equilibrium, I ran the model at a 10 km horizontal grid resolution with constant surface forcing for 50 ka while keeping the geometry fixed. Based on this initial state, I then started the paleo climate forcing spin-up (125 ka to 0 ka) with full physics. Horizontal and vertical model resolutions are 5 km and 20 m, respectively. The computational domain extends horizontally over 1500 km × 2800 km, and vertically over 4000 m in the ice and 1000 m in the bedrock. Grid refinements are made from 10 km to 5 km at -5000 a. The FTT mechanism is switched on at -5000 a. The paleo spin-ups have been performed using pism v0.5-88-gc24f74b.

Table A3: Ice sheet model parameters that have been altered from the default PISM values (The PISM Authors, 2014) during the equilibrium and forward simulations.

Symbol	Description	Value
E_{SIA}	the flow enhancement factor for SIA	1
q	the exponent of the pseudo-plastic basal resistance model	0.25
ϕ	the till fraction angle	°
ϕ_{min}	for bed elevations lower than 300 m below sea level [°]	5
ϕ_{max}	for bed elevations higher than 700 m above sea level [°]	30
α	pore water pressure fraction	0.98

The equilibrium and forward simulations have been performed using pism v0.5-88-gc24f74b.

Table A4: Prediction errors for modelled horizontal surface velocities and ice thickness at the end of the forward simulation (~2012), and modelled cumulative mass change [Gt] for the period 1997-2012 together with the residual signal between modelled and observed ice mass change (Sect. 2) in percent [%]. Root Mean Squared Error (RMSE), coefficient of variation (CV) of the RMSE, $\bar{o}$ mean observed ice thickness for the bed topography from Bamber et al. (2001) and Bamber et al. (2013) , $\bar{m}$ mean modelled ice thickness, and AMD absolute mean difference.

Simulation	Horizontal surface velocities					Ice thickness					Cumulative mass change [Gt]	
	RMSE [ma^{-1}]	CV [unitless]	$\bar{o}$ [ma^{-1}]	$\bar{m}$ [ma^{-1}]	AMD [ma^{-1}]	RMSE [m]	CV [unitless]	$\bar{o}$ [m]	$\bar{m}$ [m]	AMD [m]	1997-2012	Difference [%]
Rv1-J90-12	214.53	4.04	53.08	53.09	33.58	170.39	0.09	1966.67	2110.65	146.97	195.76	6 %
Rv1-R90-12	206.09	3.88	53.08	47.07	34.41	135.03	0.07	1966.67	2064.43	109.80	131.57	-29 %
Rv1-H90-12	212.57	4.01	53.08	48.83	35.85	149.30	0.08	1966.67	2092.17	128.92	30.52	-84 %
Rv2-J90-12	156.38	2.95	53.08	47.52	35.11	101.54	0.05	1996.59	2015.04	67.69	221.42	20 %
Rv2-R90-12	154.94	2.92	53.08	49.00	34.70	105.43	0.05	1996.59	1985.72	65.17	243.66	32 %
Rv2-H90-12	188.76	3.56	53.08	53.98	37.98	93.12	0.05	1996.59	1980.23	60.47	88.29	-52 %
Rv2-H90-12*(1km)	172.68	3.88	53.08	61.72	30.11	116.28	0.10	1996.59	2017.94	68.34	115.31	-38 %
Rv2-H90-12*(2km)	191.79	4.32	53.08	61.51	30.18	107.19	0.09	1996.59	2013.48	60.99	116.89	-37 %
Rv1FTT-J90-12	160.04	3.02	53.08	25.90	36.09	85.80	0.04	1966.67	2020.11	66.93	195.28	5 %
Rv1FTT-R90-12	158.29	2.98	53.08	26.28	36.19	71.04	0.04	1966.67	2001.13	51.03	127.79	-31 %
Rv1FTT-H90-12	164.88	3.11	53.08	28.36	35.24	71.09	0.04	1966.67	2008.38	51.02	-13.85	-107 %
Rv2FTT-J90-12	135.58	2.56	53.08	36.24	32.36	66.15	0.03	1996.59	1999.62	43.80	218.73	18 %
Rv2FTT-R90-12	137.68	2.59	53.08	32.98	33.88	74.41	0.04	1996.59	1982.08	43.04	176.42	-5 %
Rv2FTT-H90-12	145.43	2.74	53.08	36.14	33.86	61.70	0.03	1996.59	1980.24	34.93	34.82	-81 %

Appendix C. Study 2

C1. Parameters

Table A5: Ice sheet model parameters (The PISM Authors, 2014) that remain unchanged both during equilibrium and the forward simulations.

Symbol	Description	Value
E_{SIA}	the flow enhancement factor for SIA	1.5
E_{SSA}	the flow enhancement factor for SSA	0.6
ϕ	the till fraction angle	°
ϕ_{min}	for bed elevations lower than 300 m below sea level [°]	15
ϕ_{max}	for bed elevations higher than 700 m above sea level [°]	40
S_0	salinity of the ocean water under the ice shelves [*psu*]	35
q	the exponent of the pseudo-plastic basal resistance model	0.3
δ	the till effective fraction overburden	0.022

Table A6: Ice sheet model parameters that have been altered relative to the equilibrium simulations.

Symbol	Description	Forward	Equilibrium
F_{melt}	parameter for subshelf melting [$m\ s^{-1}$]	0.4705	0.01
H_{cr}	ice thickness threshold [m]	400	500
K	proportionality constant for eigen calving [ms]	2^{18}	10^{18}
T_o	temperature of the ocean water [°C]	variable*	-1.7

* Please refer to Sect. 2.2.1 for ocean water temperature scenarios.

The equilibrium and forward simulations have been run on 30 and 80 cores using PISM v0.6.1-10-g37ef3af.

.

C2. Additional figures and tables

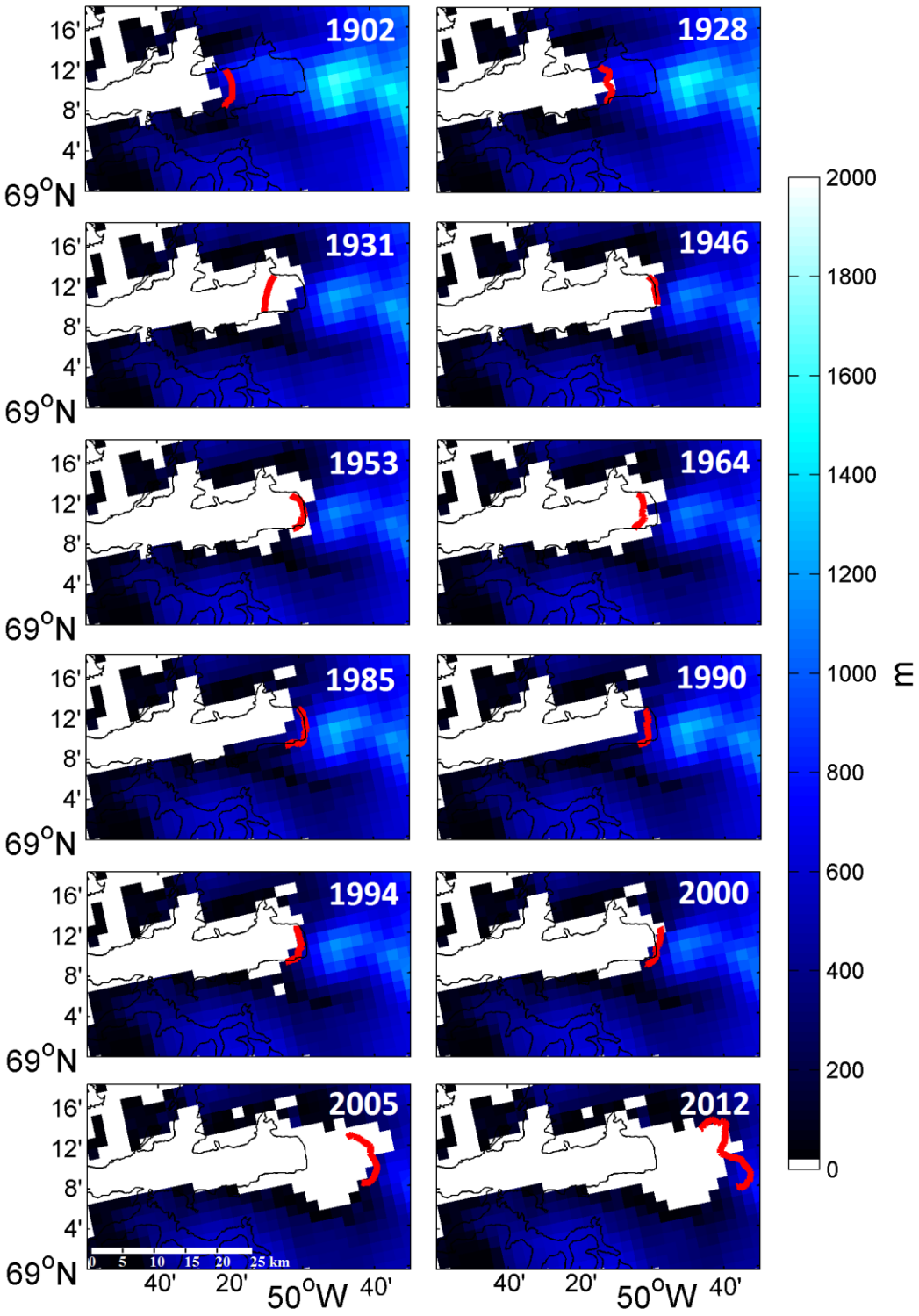

Figure A 3: Modelled ice thickness in the simulation with variable surface ocean temperature over the period 1840-2012 at JI. The solid red lines represent the observed positions of the terminus for the different years plotted.

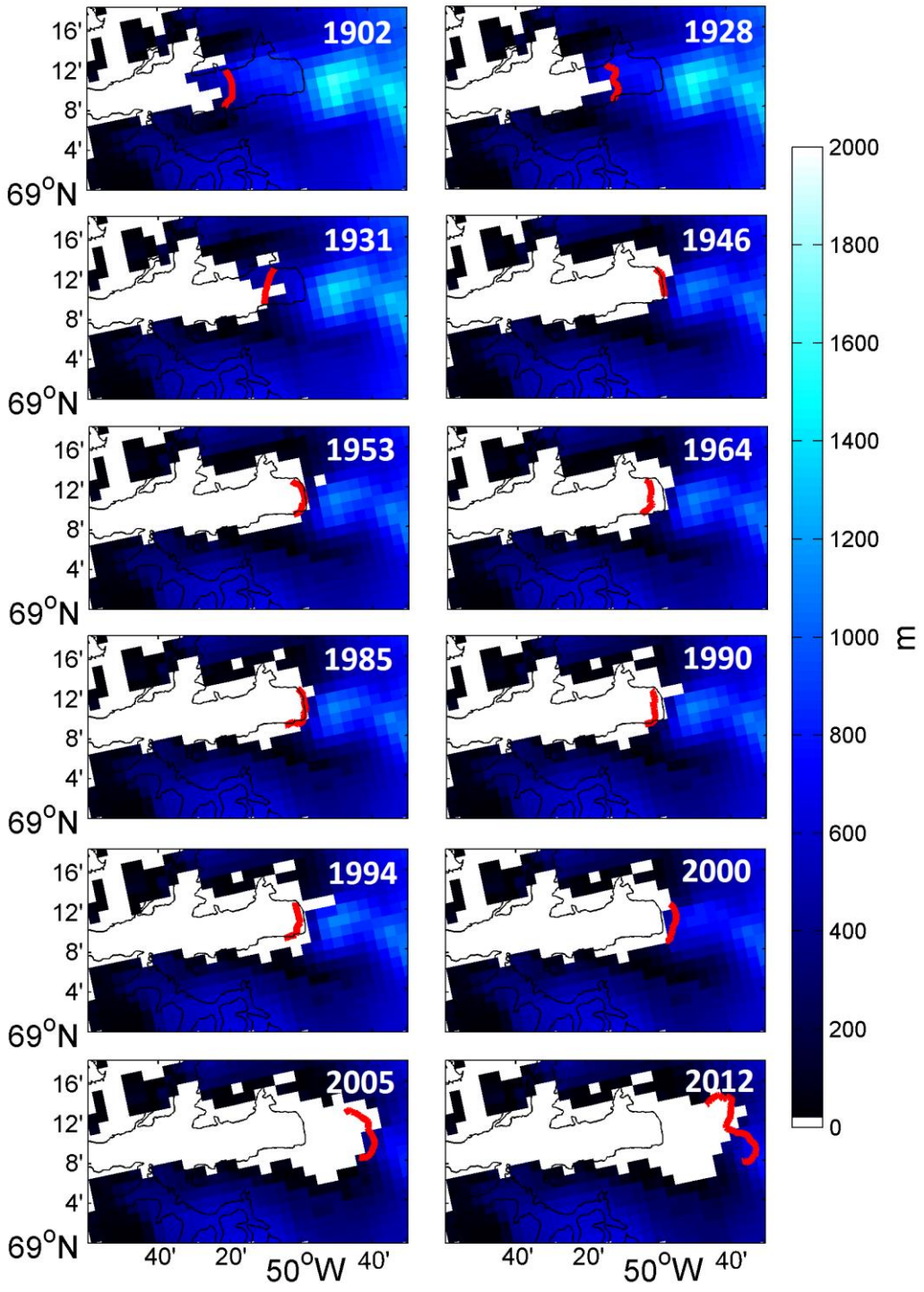

Figure A 4: Modelled ice thickness in the simulation with constant surface ocean temperature over the period 1840-2012 at JI. The solid red lines represent the observed positions of the terminus for the different years plotted.

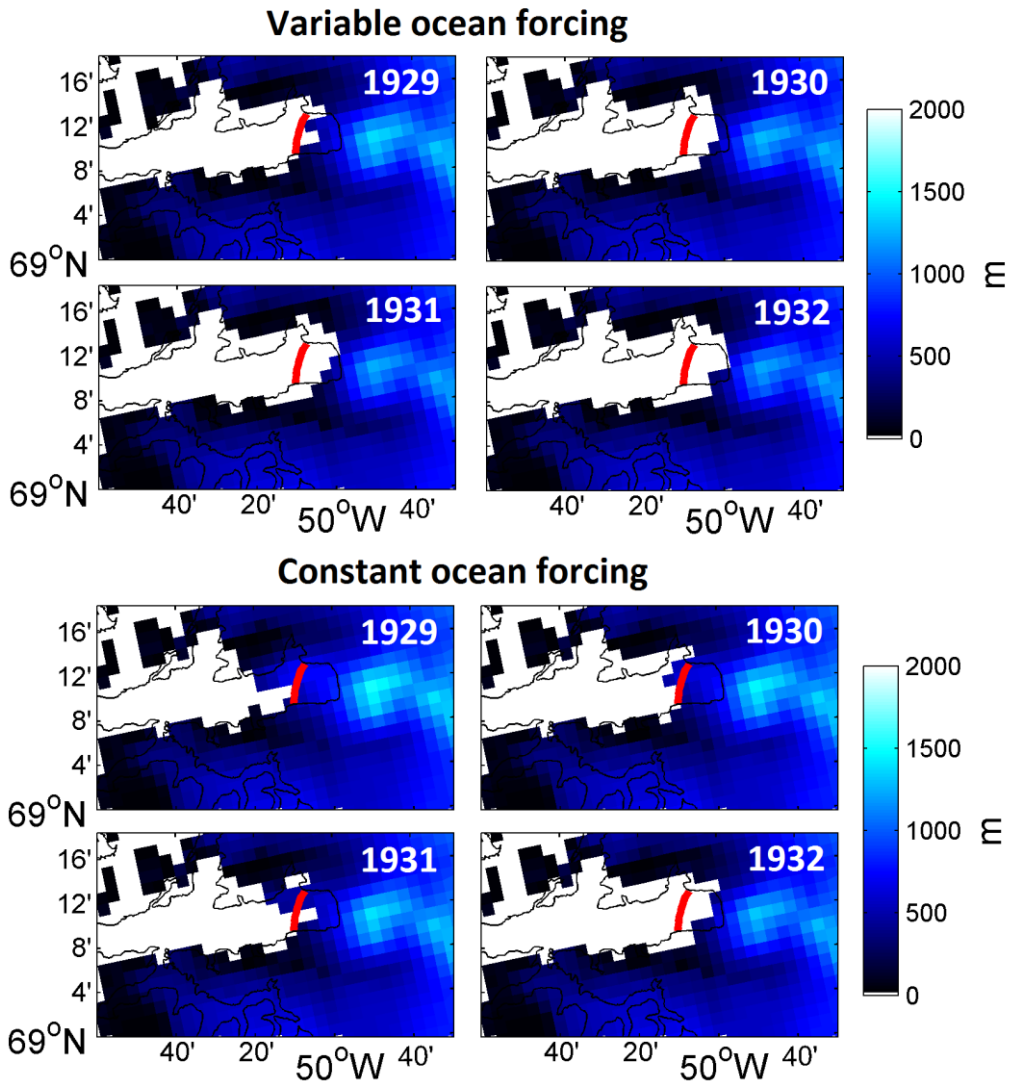

Figure A 5: Modelled ice thickness in the simulation with variable surface ocean temperature and in the simulation with constant surface ocean temperature during 1929, 1930, 1931 and 1932 at JI. The solid red lines represent the observed 1930 terminus position.

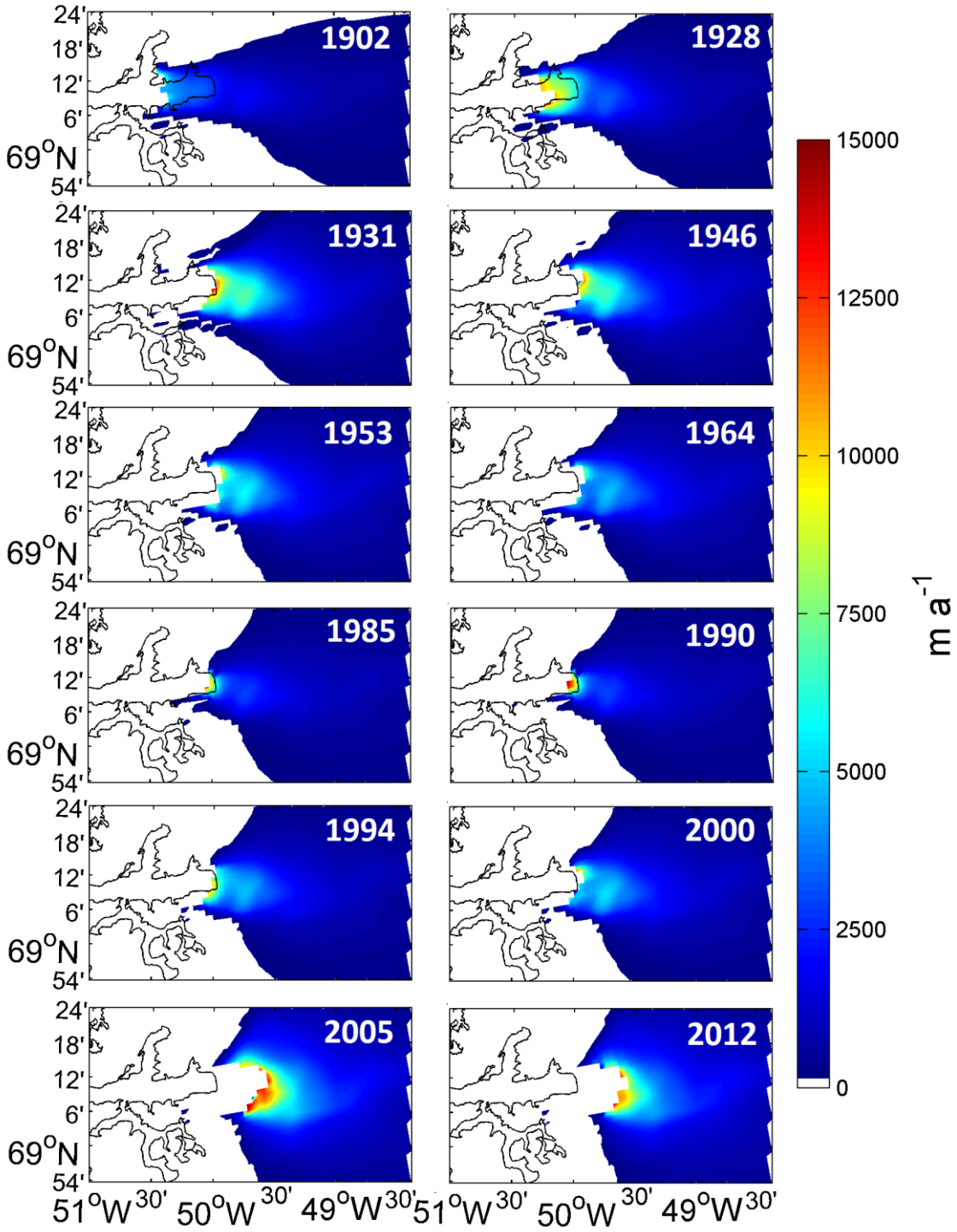

Figure A 6: Modelled horizontal surface velocities in the simulation with variable surface ocean temperature over the period 1840-2012 at JI.

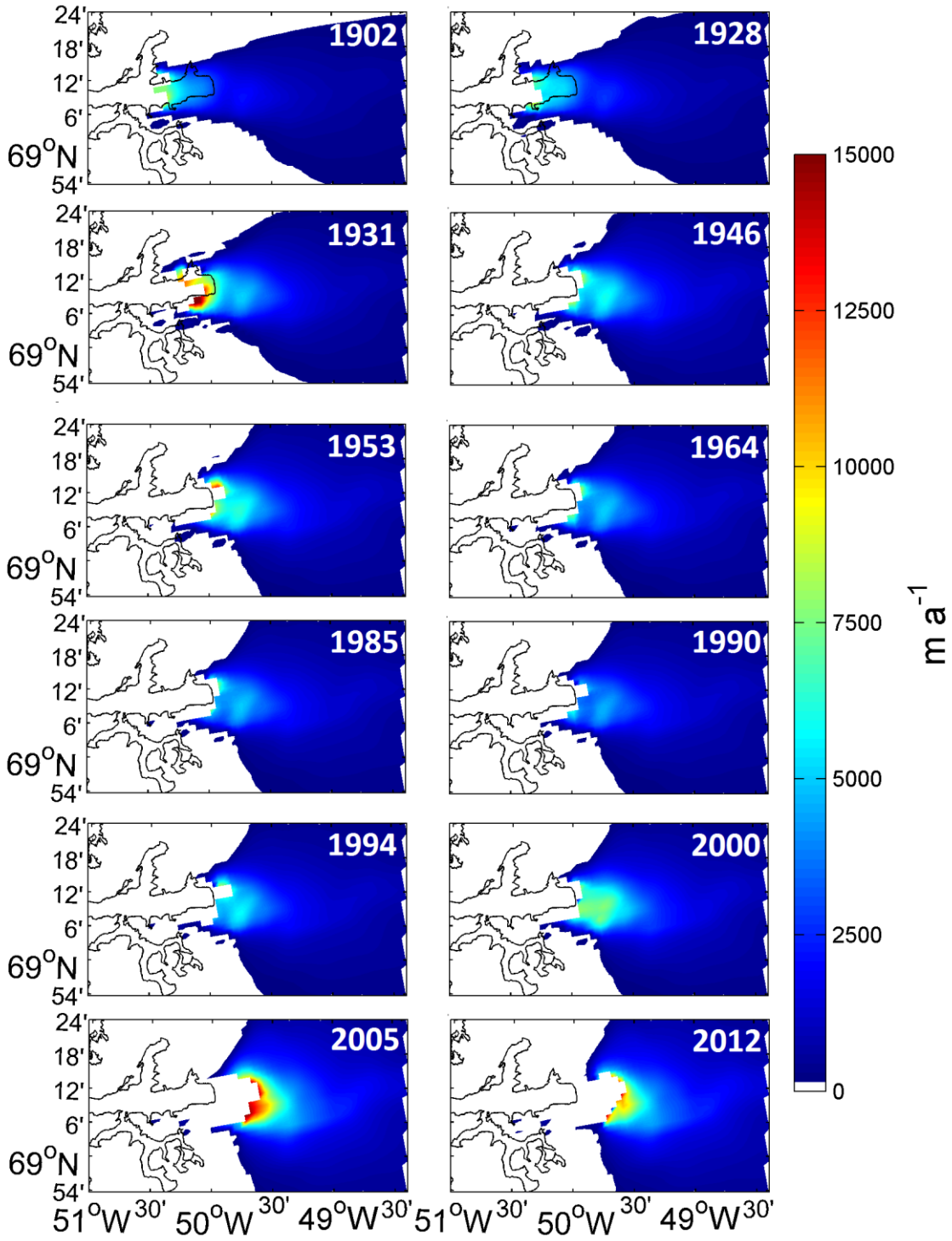

Figure A 7: Modelled horizontal surface velocities in the simulation with variable surface ocean temperature over the period 1840-2012 at JI.

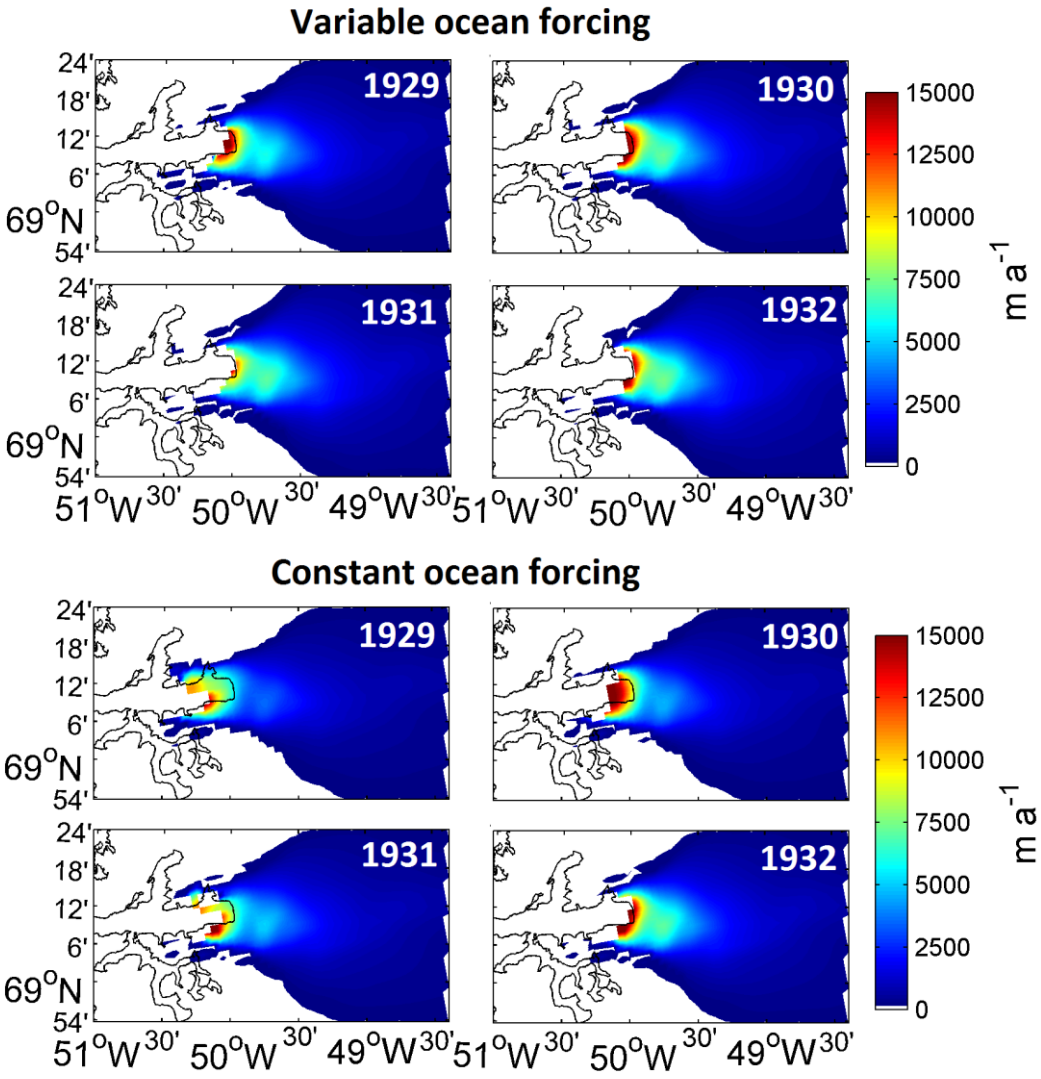

Figure A8: Modelled horizontal surface velocities in the simulation with variable surface ocean temperature and in the simulation with constant surface ocean temperature during 1929, 1930, 1931 and 1932 at JI.

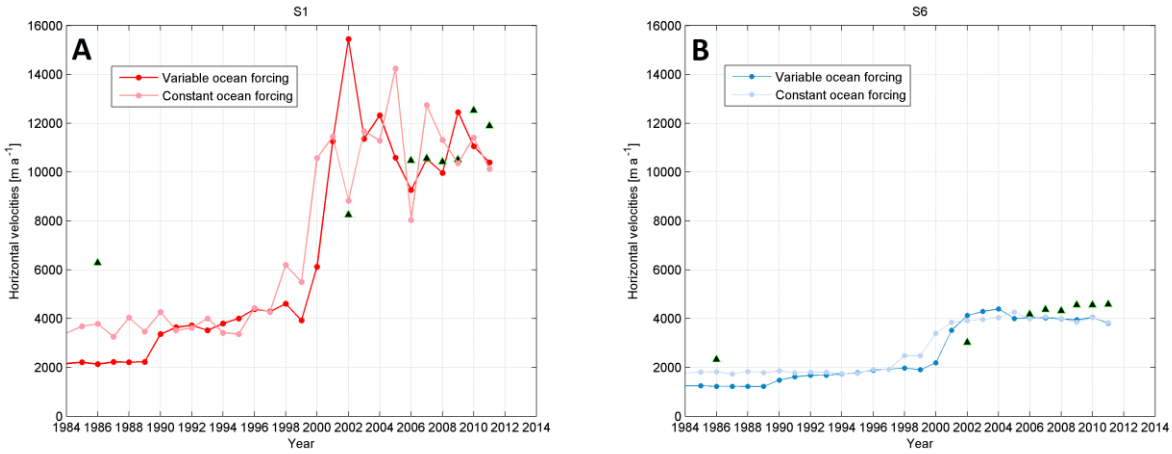

Figure A 9: Time series of modelled (filled circles) versus observed (black triangles with light green edges) velocities (Joughin et al., 2010) for the period 1990–2012 at locations S1 (A) and S6 (B) shown in Fig. 1C in a simulation with variable surface ocean temperature (darker colour) and a simulation with constant surface ocean temperature (lighter colour).

Table A7: Root Mean Squared Error (RMSE) for modelled horizontal surface velocities (i.e. along the flowline shown in Figure 1C) during 2000-2001, 2005-2006, 2006-2007 and 2008-2009 in a simulation with variable surface ocean temperature ("Variable") and a simulation with constant surface ocean temperature ("Constant"). The observed velocities relative to which I compute the RMSE are from Joughin et al. (2010).

	Simulation	
Time	**Variable [ma^{-1}]**	**Constant [ma^{-1}]**
2000-2001	667	996
2005-2006	91	839
2006-2007	623	1063
2008-2009	802	280

Table A8: Root Mean Squared Error (RMSE) for modelled ice thickness changes (i.e. at points S1, S3 and S6 shown in Figure 1C) during 2003, 2005, 2006, 2007, 2008, 2009, 2010, 2011 and 2012 in a simulation with variable surface ocean temperature ("Variable") and a simulation with constant surface ocean temperature ("Constant"). The observed ice thickness changes relative to which I compute the RMSE are from Krabill (2014).

	Points		
Simulation	**S1 [m]**	**S3 [m]**	**S6 [m]**
Variable	9	12	33
Constant	18	21	3

Table A9: Mass loss estimates and major terminus collapses at JI during the period 1840-2012 in a simulation with constant surface ocean temperature (Sect. 2.2.1).

Historic	Mass loss (Gt)	Mass loss rate (Gta^{-1})	Major terminus collapse (year)
1840-1880	37.42	0.9	
1880-1920	112.62	2.8	
1920-1960	315.36	7.7	1932
1960-1990	338.93	10.93	
1990-2012	424.01	18.44	1998-2003
1997-2012	306.97	19.2	

Table A10: Mass loss estimates and major terminus collapses at JI during the period 1840-2012 in a simulation with variable surface ocean temperature (Sect. 2.2.1).

Historic	Mass loss (Gt)	Mass loss rate (Gta^{-1})	Major terminus collapse (year)
1840-1880	37.42	0.9	
1880-1920	112.62	2.8	
1920-1960	437.63	10.6	1929
1960-1990	373.59	12.1	
1990-2012	253.18	11.01	1999-2003
1997-2012	209.33	13.08	

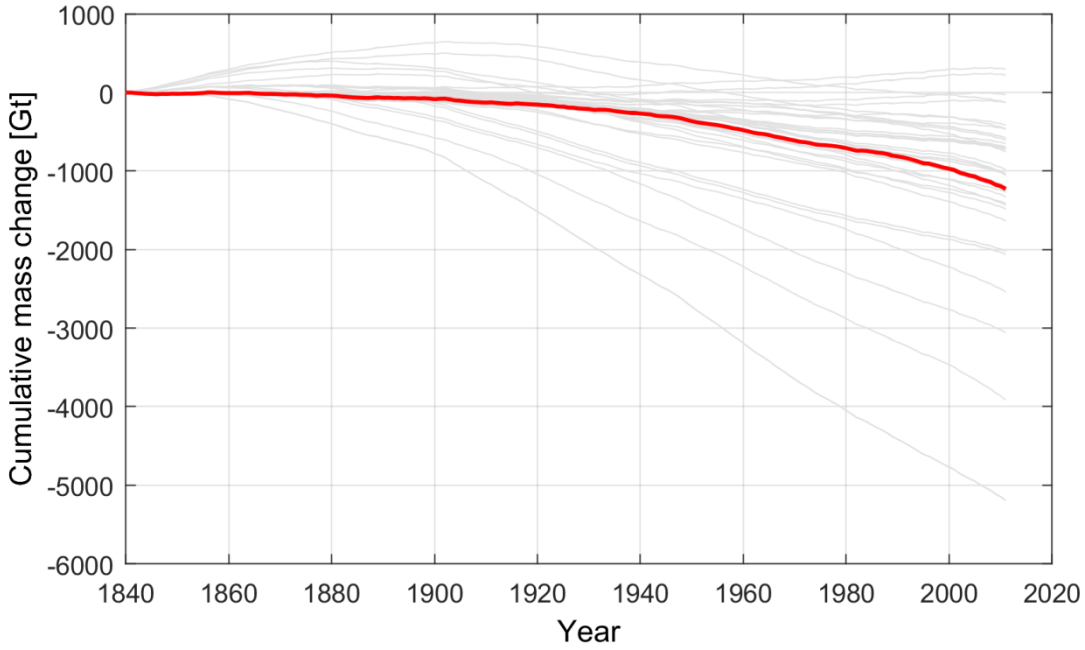

Figure A 10: Cumulative mass change for part of the simulations performed in Study 2. During these simulations, I altered parameters controlling the ice dynamics (e.g. the flow enhancement factor, the exponent of the pseudo-plastic basal resistance model, the till effective fraction overburden, etc.) and parameters related with ice shelf melt, ocean temperature, and calving (i.e., the ice thickness threshold in the basic calving mechanism). The simulations include experiments with no ocean forcing, constant ocean forcing, and variable ocean forcing. The red curve represents the simulation that best capture the full observed evolution of JI during the period 1840–2012.

Appendix D. Study 3

D1. Parameters

Table A11: Ice sheet model parameters (The PISM Authors, 2014) that remain unchanged both during equilibrium and the forward simulations.

Symbol	Description	Value
E_{SSA}	the flow enhancement factor for SSA	0.6
K	proportionality constant for eigen calving [ms]	2^{18}
ϕ	the till fraction angle*	°
ϕ_{min}	for bed elevations lower than 300 m below sea level [°]	15
ϕ_{max}	for bed elevations higher than 700 m above sea level [°]	40
S_0	salinity of the ocean water under the ice shelves [psu]	35

Table A12: Ice sheet model parameters that have been altered from the default PISM values (The PISM Authors, 2014) during the forward simulations.

Symbol	Description	Value*	Range**
E_{SIA}	the flow enhancement factor for SIA	1.2	1.0 - 1.3
F_{melt}	parameter for subshelf melting [$m\ s^{-1}$]	0.5505	0.01– 1
H_{cr}	ice thickness threshold [m]	375	250 - 450
q	the exponent of the pseudo-plastic basal resistance model	0.25	0.2 - 0.3
δ	the till effective fraction overburden	0.02	0.02-0.03
T_o	temperature of the ocean water [$°C$]	-1.7	-1.3 - -1.9

* The parameterization that best captures the full evolution of JI during the period 1990–2014;

** Range (min/max values) for the parameters tested during the simulations;

The equilibrium and forward simulations have been run on 30 and 80 cores using PISM v0.6.1-10-g37ef3af. I performed over 50 simulations in which I varied during the regional runs different parameters with a focus on $E_{SIA}, q, \delta, F_{melt}$, H_{cr} and T_o. The parameters or rather the range of the parameters (min, max) is shown in Table A12, 4th column. In order to match the overall retreat trend, the parameters F_{melt}, H_{cr} and T_o were altered first. However, a finer tuning was required to match the observed front positions and to capture the two accelerations (i.e., 1998 and 2003) within the observed time frame. This fine tuning was done by altering some of the parameters that control ice dynamics (E_{SIA}, q, δ).

From these simulations, I present in Study 3 the parameterization that best captures the full evolution of JI during the period 1990–2014: (i) in terms of observed versus modelled front positions for 1990-2014 and (ii) based on the correlation between observed and modelled mass changes during 1997-2014. While (i) is based on my visual interpretation, for (ii) I

selected those simulations within a +/- 30 Gt threshold. I found 3 simulations to satisfy (i) and (ii). From these simulations, I chose only the one that captured the two accelerations in the observational record within a 1 year time frame difference and that has overall magnitudes similar with those in the observational record (i.e, the RMSE in point S1 is ~2236 m a^{-1}; Fig. 28).

Table A13: Yearly mean modelled basal melt rates.

Year	Melt rates [ma^{-1}]
1990	262
1991	473
1992	150
1993	123
1994	159
1995	162
1996	148
1997	177
1998	690
1999	1153
2000	1387
2001	1368
2002	1295
2003	881
2004	242
2005	159
2006	145
2007	142
2008	138
2009	134
2010	148
2011	154
2012	177
2013	147
2014	159

Appendix E. Study 4

E1. Parameters

Table A14: Ice sheet model parameters (The PISM Authors, 2014) used during the prognostic simulations.

Symbol	Description	Value
E_{SIA}	the flow enhancement factor for SIA	1.5
E_{SSA}	the flow enhancement factor for SSA	0.6
K	proportionality constant for eigen calving [ms]	2^{18}
ϕ	the till fraction angle	°
ϕ_{min}	for bed elevations lower than 300 m below sea level [°]	15
ϕ_{max}	for bed elevations higher than 700 m above sea level [°]	40
S_o	salinity of the ocean water under the ice shelves [psu]	35
T_o	temperature of the ocean water [$°C$]	variable*
q	the exponent of the pseudo-plastic basal resistance model	0.3
δ	the till effective fraction overburden	0.022
F_{melt}	parameter for subshelf melting [$m\ s^{-1}$]	0.4705
H_{cr}	ice thickness threshold [m]	400

* Please refer to Sect. 2.2.2 for ocean water temperature scenarios.

The prognostic simulations have been run on 30 cores using PISM v0.6.1-10-g37ef3af.

E2. Additional figures and tables

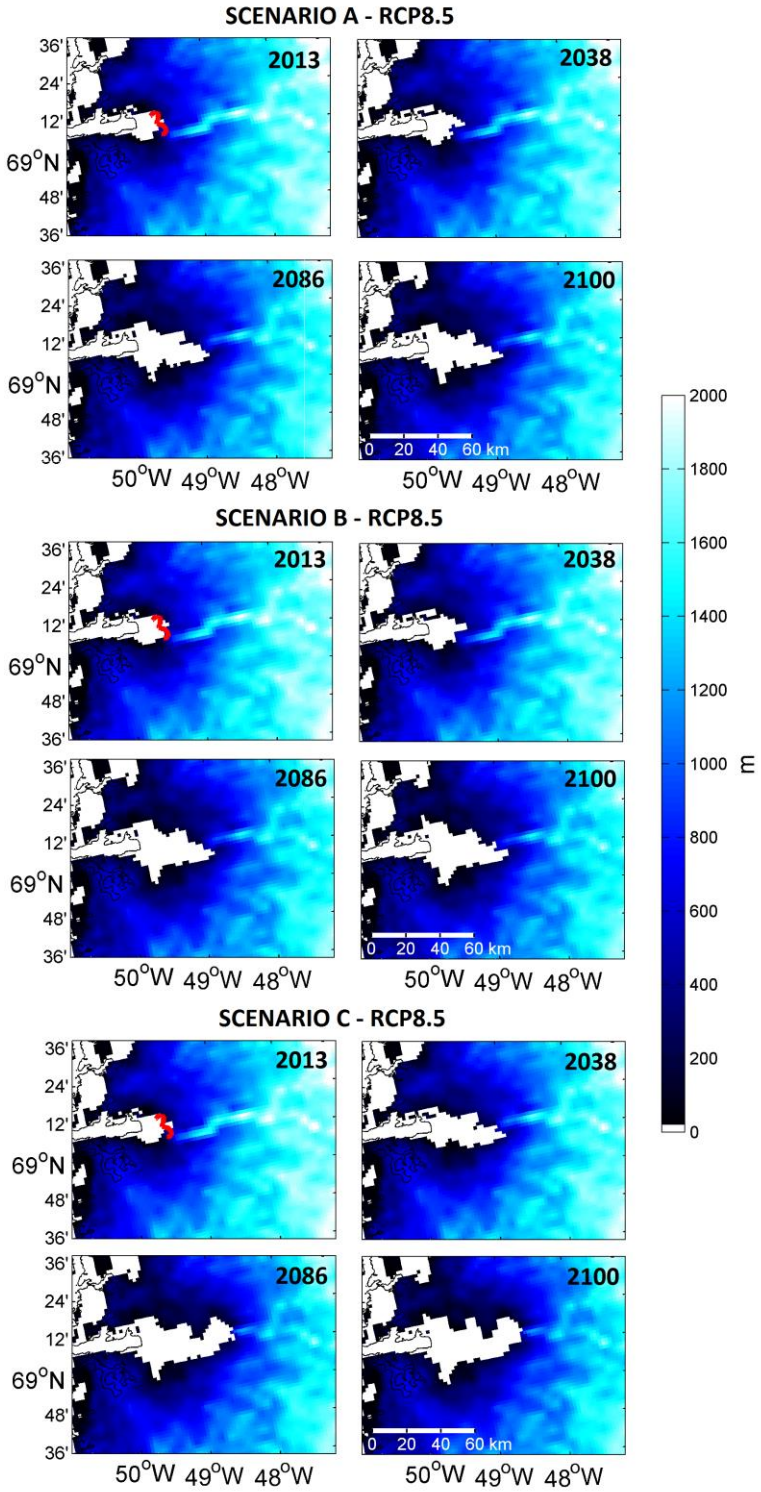

Figure A 11: Modelled terminus retreat at JI between 2013-2100 for Scenario A, Scenario B and Scenario C built under RCP 8.5. The colorbar shows the ice thickness in meters. The red line denotes the 2012 observed terminus position.

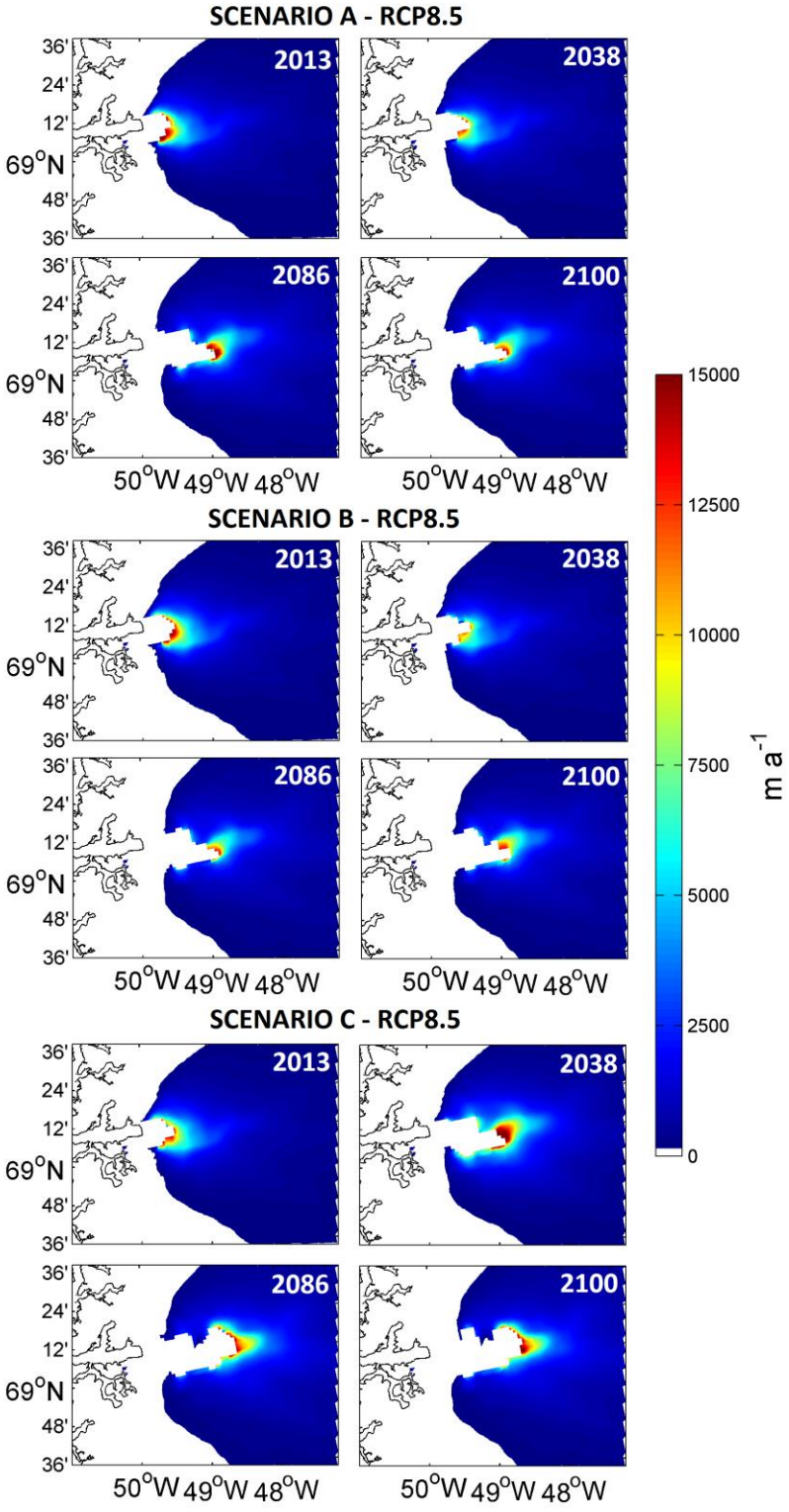

Figure A 12: Modelled horizontal velocities at JI between 2013-2100 for Scenario A, Scenario B and Scenario C built under RCP 4.5. The colorbar shows horizontal velocites in m a^{-1}.

Appendix F. Extra figures

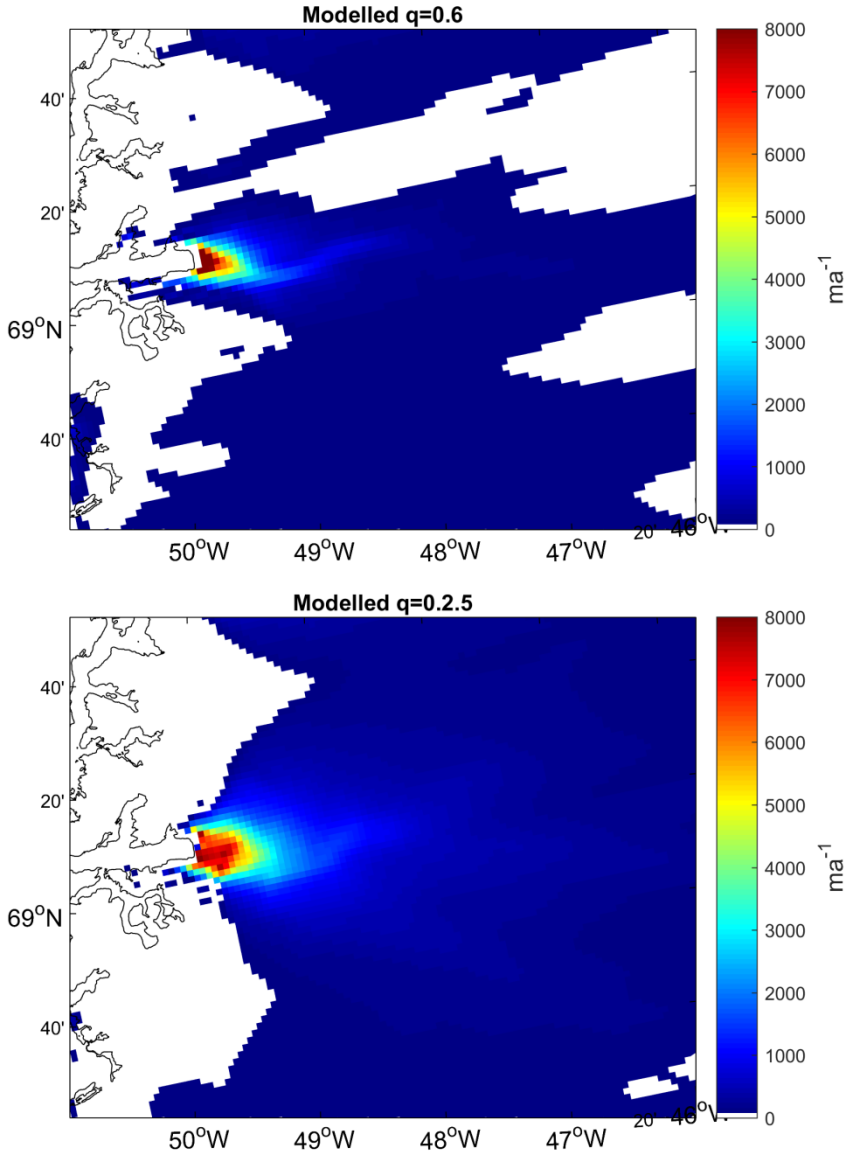

Figure A 13: Modelled horizontal velocities at JI with q=0.6 (top) and q=0.25 (bottom).

Appendix G. Teaching activities and conferences

G1. Teaching activities

Teaching assistant – "GPS, GIS and Setting out" (June, 2013)

Teaching assistant – "Mathematical and Numerical Methods in Earth and Space Physics" (February-May, 2014)

Teacher – "Mathematical and Numerical Methods in Earth and Space Physics" (February-May, 2015)

Continuum dynamics

GIA using SELEN

Finite element method (FEM)

Teacher – "Mathematical and Numerical Methods in Earth and Space Physics" (February-May, 2016)

Continuum dynamics

GIA using SELEN

Modelling glaciers and ice sheets (Driving stresses, Ice flow, SIA)

Finite element method (FEM)

G2. Conferences

EGU General Assembly, April 2014 (Poster no. EGU2014-6110)

Muresan et al., "Modelling the behavior of the Jakobshavn glacier since the end of the Little Ice Age"

http://meetingorganizer.copernicus.org/EGU2014/EGU2014-6110-1.pdf

Conference abstract published in:

Geophysical Research Abstracts Vol. 16,

EGU2014-6110-1, 2014

Proceedings of the Chamonix Symposium, May 2014 (Poster no. 70A1071)

Muresan et al., "Modelling the behavior of Jakobshavn glacier in the last century"

Conference abstract published online:

http://www.igsoc.org/symposia/2014/chamonix/proceedings/proceedings.html

American Geophysical Union (AGU) Fall Meeting, December 2014 (Poster no. C51B-0257)

Muresan et al., "Impact of External Forcing on Glacier Dynamics at Jakobshavn Isbræ during 1840-2012"

Conference abstract published online:

https://agu.confex.com/agu/fm14/webprogram/Paper7768.html

American Geophysical Union (AGU) Fall Meeting, December 2014 (Poster no. C51B-0258)

Khan et al., "Modelled and observed present-day state of the Jakobshavn Isbræ, west Greenland"

Conference abstract published online:

https://agu.confex.com/agu/fm14/webprogram/Paper12379.html

GIA modelling 2015, May 2015 (Oral talk)

Muresan et al., "Mass change at Jakobshavn Isbræ during 1880-2012", GIA meeting, Geophysical Institute, Fairbanks, Alaska, 2015.

American Geophysical Union (AGU) Fall Meeting, December 2015 (Poster no. C21A-0715)

Muresan et al., "Basin-Wide Mass Balance of Jakobshavn Isbræ (West Greenland) during 1880-2100"

Conference abstract published online:

https://agu.confex.com/agu/fm15/webprogram/Paper68423.html

National Space Institute
Technical University of Denmark
www.space.dtu.dk

Elektrovej 328
DK-2800 Kgs. Lyngby
Tlf. +45 45259500
Fax +45 45259575

ISBN 978-87-91694-32-5